Northwest Swell Variability at the Hawaiian Islands

A THESIS SUBMITTED TO THE GRADUATE DIVISION OF THE UNIVERSITY OF HAWAI'I AT MĀNOA IN PARTIAL FULFILLMENT OF THE REQUIREMENTS FOR THE DEGREE OF

MASTER OF SCIENCE

IN

OCEANOGRAPHY

August 2017

By
Alyssa E. Agustin

Thesis Committee:
Mark A. Merrifield, Chair
Douglas S. Luther
Charles Fletcher
Philip Thompson

ACKNOWLEDGEMENTS

I would like to express the utmost gratitude to my advisor, Dr. Mark Merrifield, for his unwavering support, guidance, and enthusiasm over the past five years. His insights were invaluable for the growth and success of this research and his generous financial support made my experience in graduate school possible. His example as a hard-working oceanographer, putting in many extra hours out of his love for science, has impacted me tremendously and he has become a great role model to me as I continue to grow as a young scientist.

I also would like to thank the members of my committee who were a pleasure to work with for their support and feedback throughout this process. Their comments and suggestions have greatly improved this research and each played a significant role in seeing this work come to fruition. Dr. Phil Thompson was especially helpful with the ESTELA model and I thank him.

I gratefully acknowledge Pat Caldwell for providing his Goddard and Caldwell surf observation dataset, Dr. Ning Li for providing her wave hindcast model output at Waimea, and Dr. Heidi Sherman for sharing her Baldwin Beach, Maui volume data with us. I am indebted to Dr. Kimball Millikan and the Hawai‘i Ocean Time Series physical oceanography team for their assistance with earning my field time experience requirement. I would like to thank Dr. Eric Firing for his open ears, critical outlook, and sharp mind that helped me develop some understanding of physical oceanography through innumerable, enjoyable discussions.

This research was sponsored by the Joint Institute for Marine and Atmospheric Research and the University of Hawai‘i Sea Level Center.

ABSTRACT

The influence of Pacific climate variability on the wind wave field at Hawai‘i is examined by identifying the regional winds that are most influential in driving waves in the winter. We demonstrate how the ESTELA (a method for Evaluating the Source and Travel-time of the wave Energy reaching a Local Area) model can be used to identify source regions using wave buoys around the islands for initialization and validation. We examine changes in the source wind field that drive the dominant northwest swell energy that arrives during winter months, and compare these variations with the prominent climate modes and storm tracks of the north Pacific. A case study of the impact of variations in the energy flux is conducted at Baldwin Beach on the north shore of Maui Island. We find that northwest winter swells are closely related to the North Pacific Index, sea level pressure at 42.5°N, 150°W, an increase in the number of extratropical storms, more southerly storm tracks, and an intensified east asian jet stream.

List of Tables

List of Figures

Table of Contents

Acknowledgements

Abstract

1 | Introduction

The Hawaiian Islands receive a wide range of swells that influence the local wave climate. Understanding the waves that are expected to arrive at shore is essential to the management of coastal resources such as beach sand, groundwater, wave energy conversion devices, and coral reefs. Waves are also important to coastal stakeholders, beachgoers, tourists, surfers, coastal engineers, and researchers to make safe, well-informed decisions. The dominant three types of swells Hawai‘i experiences are the easterly trade wind swells, northwest swells generated by north Pacific winter storms, and south swells that are generated by south Pacific winter storms (Stopa et al., 2013). In Hawai‘i, few studies have been done about the changes in the swells over time scales greater than a year.

For this study I expand the work done by (Aucan, 2006) to create a wave climatology for Hawai‘i using wave buoys, models, and observations. The previous study, Aucan (2006), created a directional wave climatology for the north shore of O‘ahu and found an increase in the occurrence of winter extreme wave events in time using model data. There are 16 buoys around Hawai‘i with data from a subset dating from 1981 to present as well as an observational record from 1969 to present that I use to examine changes in the winter wave climate. Studies have shown that long-term wave climate variability in the northern hemisphere is related to some climate indices (e.g. Bromirski et al. (1999); Rooney et al. (2004); Caldwell (2005); Aucan (2006); Menèndez et al. (2008)). This thesis looks for climate indices that have a robust relationship to the wave field in Hawai‘i and for physical forcings that can be used to predict winter wave variability in the Islands.

Secondly, I use the ESTELA model (Pérez et al., 2014) to determine the sources of waves arriving at buoys surrounding Hawai‘i and focus on the energetic winter swell. The ESTELA model will outline the region where the northwest swell is generated and the Pacific climate in that region will be studied.

Lastly, I conduct a case study relating wave energy flux to sediment transport at Baldwin Beach on the north shore of Maui. This information can lead to further studies examining the contribution of wave activity to beach erosion.

Understanding the wave climate of Hawai‘i is essential for oceanographers, coastal engineers, and coastal planners who make decisions and inferences based upon the expected wave climate. The present study will fill a gap in the literature to aide coastal work. Some of the broader impacts are to residents who decide to live in the coastal zones and will be directly impacted by any changes in the wave climate. As a student, I will benefit greatly from this work by being able to learn more about coastal waves which is my primary interest, how to model waves in Hawai‘i, and how to bring deep water wave information to the shoreline.

The wave buoys used in this study are discussed in Chapter 3, the methods used for the ESTELA model and results are described in Chapter 4, and the Baldwin Beach case study is described in Chapter 5. The results and discussion are presented in Chapter 6, and the conclusion in Chapter 7.

2 | Background

2.1 Hawaii's Oceanographic Setting

The Hawaiian archipelago is located in the middle of the tropical north Pacific, and receives a wide range of swells and seas. The three main types of swells impacting the main Hawaiian Islands include the northwest swells generated by north Pacific winter storms, the south swells generated by south Pacific winter storms, and the year-round, easterly, trade-generated seas and swells (Moberly and Chamberlain, 1964). Additional sources includes occasional hurricanes and winds from the southwest (Kona winds).

2.2 Wave Generation

Sea-swell waves in the ocean are generated by surface winds. A theory of the transfer of energy from wind to waves that included both normal and tangential stresses was first proposed by Sverdrup (1947). Later, Phillips (1957) considered pressure and surface stress fluctuations at the start of wave generation. The roughening of the ocean's surface has been understood in terms of how the wind's velocity varies from a high altitude to the sea surface. The vertical variation, know as the velocity profile, is affected by the turbulent properties of the fluid. Over the ocean the velocity decreases as the sea surface is approached. When velocities are small relative to the ratio of characteristic length to a measure of the viscosity, the flow is laminar. As the velocity increases, the flow becomes turbulent. As the wind blows, energy is put into the ruffled sea surface and waves begin to grow in both height and length.

The northwest swell for the Hawaiian Islands is known to be generated by extratropical storms near the Kuril and Aleutian Islands during November through March as the subtropical high pressure weakens and variable wind patterns develop (Stopa et al., 2011). Extreme surf episodes in Hawaiʻi typically coincide with the genesis region being closer to the islands. High-surf episodes tend to last longer from extratropical cyclones that form in the far northwest Pacific, have a slow east-component track speed, and typically coincide with an occluded low-pressure system about 1500 km northwest to north of Hawaiʻi (Caldwell et al., 2009). From December to February the large swells experience a shift from northwest toward more west-northwesterly direction, due to the southerly migration of the north Pacific storm track (Caldwell, 2005).

The south facing shores experience more gentle swells generated by the year-round Westerlies in the southern hemisphere that are augmented by mid-latitude cyclones off Antarctica during May through September.

The trade winds generate wind waves from the northeast to east throughout the year forced by the subtropical high-pressure region (Stopa et al., 2011; Li et al., 2016). The steep volcanic mountains on the Hawaiian Islands speed up the wind flows in the channels and create prominent wakes in increased wave height in the channels and to the south of Hawaiʻi Island (Yang et al., 2005; Nguyen et al., 2010; Stopa et al., 2013; Hitzl et al., 2014). These localized wind flows together with island sheltering create regional wave patterns in the lee of the islands with large spatial and temporal variations (Aucan, 2006; Caldwell et al., 2009; Stopa et al., 2011).

2.3 North Pacific Climate Indices and Storm Tracks

The Pacific/North American Index (PNA) is one of the most prominent modes of low-frequency variability in the northern hemisphere extratropics. The positive phase of the PNA pattern features above-average 500 millibar geopotential heights in the vicinity of Hawaiʻi and over the intermountain region of North America, and below-average heights located south of the Aleutian Islands and over the southeastern United States (Trenberth and Hurrell, 1994). The PNA pattern is associated with strong fluctuations in the intensity of the east asian jet stream (Chan et al., 2017). The positive phase is associated with an eastward shift in the jet exit region toward the western United States (Wallace and Gutzler, 1981). The PNA pattern also is strongly influenced by the El Niño Southern Oscillation (ENSO). The positive phase of the PNA pattern tends to be associated with Pacific warm episodes (El Niño), and the negative phase tends to be associated with Pacific cold episodes (La Niña). Menèndez et al. (2008) found that PNA had a positive relationship with extreme wave heights on the west coast of the United States.

Niño 3.4 is an anomaly that may be thought of as representing the average equatorial sea surface temperatures across the Pacific from about the dateline to the South American coast. The Niño 3.4 index uses a 5-month running mean, and El Niño or La Niña events are defined when the Niño 3.4 sea surface temperatures (SSTs) exceed +/- 0.4°C for a period of six months or more (Barnston et al., 1997). El Niños tend to strengthen the weather systems that occur in the north Pacific (Stopa et al., 2013) and give them longer life spans (Rocha, 2016). In Hawai'i and the west coast of North America, the number of swell events was found to increase during El Niño years (Aucan, 2006; Menèndez et al., 2008; Barnard et al., 2015, 2017). During the 1997-1998 El Niño, storm tracks coming across the Pacific arrived further south on the west coast (Barnard et al., 2017). This could be related to the deepening of the Aleutian Low during that El Niño (Adams et al., 2008; Gan et al., 2017).

The North Pacific Index (NPI) is the area-weighted sea level pressure over the region 30°N-65°N, 160°E-140°W. The NPI index is defined to measure interannual to decadal variations in the atmospheric circulation in the Aleutian Low region (Trenberth and Hurrell, 1994).

The North Pacific Oscillation (NPO) is a north-south seesaw in winter sea level pressure over the north Pacific on monthly (and shorter) time scales. It was defined in 1924 by Sir Gilbert Walker as the opposition between Alaska, representing the area of low pressure, and Honolulu near the margin of the high pressure area. Following Wallace and Gutzler (1981) and Wang et al. (2007), we create the NPO time series by taking the normalized sea level pressure difference between 65°N, 170°E and 25°N, 165°. NPO variability is linked to meridional displacements of the Asian-Pacific jet and Pacific storm tracks (Chan et al., 2017). The positive NPO phase represents a deeper Aleutian low (Linkin and Nigam, 2008).

The Pacific Decadal Oscillation (PDO) is a pattern of Pacific climate variability similar to ENSO in character, but with enhanced low frequency energy (Mantua et al., 1997). The PDO can remain in the same phase for 20 to 30 years, while ENSO cycles typically only last 6 to 18 months. At times, the PDO and ENSO are in phase with one another (Biondi et al., 2001). The PDO, like ENSO, consists of a warm (deepened Aleutian Low) and cool phase which alters upper level atmospheric winds (Zhang et al., 1997; Zhu et al., 2007). The Stopa and Cheung (2014) study found that the empirical orthogonal function (EOF) mode 2 of climate forecast system reanalysis (CFSR) winds in the north Pacific resembles the PDO. Research in southern California showed that waves tend to be larger during the warm phase of PDO over long time periods (Adams et al., 2008).

The Arctic Oscillation (AO) is the first leading mode from the EOF analysis of monthly mean 1000 millibar geopotential height anomalies over 20°N-90°N. Year-round monthly mean anomaly data are used to obtain the loading patterns. The loading patterns primarily capture characteristics of the cold season patterns. Stopa et al. (2013) found that the positive phase of AO is related to a more northerly jet stream.

A climatological study (Bromirski et al., 1999) of the wave field in the northeast Pacific found that during the El Niño winter of 1997-1998 the storm tracks appeared to be much more northerly than those of 1982-1983 when waves were anomalously large. The 1997-1998 winter also had more meridional "upper-air" flow (sharper troughs with less east to west width) than in 1982-1983. This pattern would build smaller, tighter surface lows, causing higher wind speeds, but with less surface fetch to build storm swells. The strength of these north Pacific westerlies is characterized by the PNA Index (Wallace and Gutzler, 1981).

El Niño is related to a weakening of the trade winds and a strengthening of weather systems in the northwest Pacific. During the El Niño phase there are changes to the tropical cyclone tracks in the western north Pacific. Tropical cyclones have a tendency to recurve and propagate northward when compared to non-ENSO conditions. During the late season, October to December, recurving storms dominate when compared to La Niña conditions. As a TC propagates north to the mid-latitudes it loses its symmetric core and gradually takes on the appearance of an extratropical storm as it experiences increased baroclinity and vertical shear, decreased sea surface temperatures, and stronger temperature gradients (Jones et al., 2003). This process is called extratropical transition (ET); tropical cyclones transition into extra-tropical storms in nearly every ocean basin with the largest number of ET occurring in the western north Pacific (Jones et al., 2003). During El Niño years, cyclones have longer life spans and a higher tendency to recurve and interact with mid-latitude transients (Chan and Liu, 2004; Camargo and Sobel, 2005) as well as an eastward shift in cyclogenesis (Lander, 1994). Studies by Aucan (2006); Caldwell (2005); Rooney et al. (2004); Menèndez et al. (2008); Rocha (2016) have found that large wave heights in Hawai‘i have a positive association with the Niño 3.4 and PNA index. This pattern of winds is consistent with the tendency for an expanded and deepened Aleutian Low during El Niño years (Horel and Wallace, 1981), and consequently rougher wave conditions in the eastern and central north Pacific.

2.4 Wave Buoys

In-situ wave data in the Hawaiian Islands are collected using wave buoys. The buoy data in this study comes from three organizations. First, data are used from the Pacific Island Ocean Observing System (PacIOOS), which maintains a network of Datawell Directional Waverider buoys to provide the most continuous record possible. Data collected by the buoys are sent to the Coastal Data Information Program (CDIP), Integrative Oceanography Division, operated by the Scripps Institution of Oceanography, which analyzes, archives, and posts the data online (Caldwell, 2005). For this study I use the historical spectral archive on the CDIP website (http://cdip.ucsd.edu/). Secondly, I use foam and discus buoy data from the National Data Buoy Center (NDBC) historical archive going back to 1996 (http://www.ndbc.noaa.gov/). Third, the oldest data used are significant wave height and dominant wave period data from the National Oceanographic Data Center (NODC) archive going back to the early 1980's (https://www.nodc.noaa.gov/). The time span of buoy data available at the time of this study is given in Table 2.1. Buoy locations are shown in Figure 2.1.

Table 2.1: Wave Buoy Inventory in the Hawaiian Islands

Name	Latitude	Longitude	Start Date	End Date
Hanalei (PacIOOS, 51208)	22.29°N	159.57°W	Oct 2, 2013	March 7, 2016
Waimea Bay (PacIOOS, 51201)	21.67°N	158.12°W	Dec 16, 2001	Mar 15, 2017
Barbers Point (PacIOOS, 51204)	21.28°N	158.12°W	Oct 11, 2010	Feb 20, 2017
Kaneohe Bay (PacIOOS, 51210)	21.47°N	157.75°W	Oct 26, 2012	Mar 3, 2017
Mokapu Point (PacIOOS, 51202)	21.42°N	157.68°W	Aug 9, 2000	Sep 13, 2016
Pauwela (PacIOOS, 51205)	21.02°N	156.43°W	Dec 3, 2011	Mar 18, 2016
Kaumalapau (PacIOOS, 51203)	20.79°N	157.01°W	May 17, 2007	Apr 29, 2015
Hilo (PacIOOS, 51206)	19.78°N	154.97°W	Mar 4, 2012	Dec 12, 2015
51001 (NDBC)	24.417°N	162.10°W	Jan 1, 1996	Dec 31, 2016
51101 (NDBC)	24.318°N	162.231°W	Feb 21, 2008	Jan 21, 2016
51100 (NODC)	23.558°N	153.900°W	Apr 23, 2009	Apr 26, 2015
51002 (NDBC)	17.037°N	157.696°W	Jan 1, 1996	May 5, 2016
51003 (NDBC)	19.289°N	160.569°W	Jan 1, 1996	Feb 14, 2016
51004 (NDBC)	17.602°N	152.395°W	Jan 1, 1996	Feb 18, 2016
51001 (NODC)	24.417°N	162.10°W	Feb 11, 1981	Dec 24, 2009
51101 (NODC)	24.318°N	162.231°W	Feb 21, 2008	Mar 31, 2011
51100 (NODC)	23.558°N	153.900°W	Apr 24, 2009	Mar 31, 2011
51002 (NODC)	17.037°N	157.696°W	Sep 6, 1984	Mar 31, 2011
51003 (NODC)	19.289°N	160.569°W	Nov 1, 1984	Mar 31, 2011
51004 (NODC)	17.602°N	152.395°W	Nov 8, 1984	Mar 31, 2011
51026 (NODC)	21.350°N	156.93°W	Jan 16, 1993	Nov 21, 1996

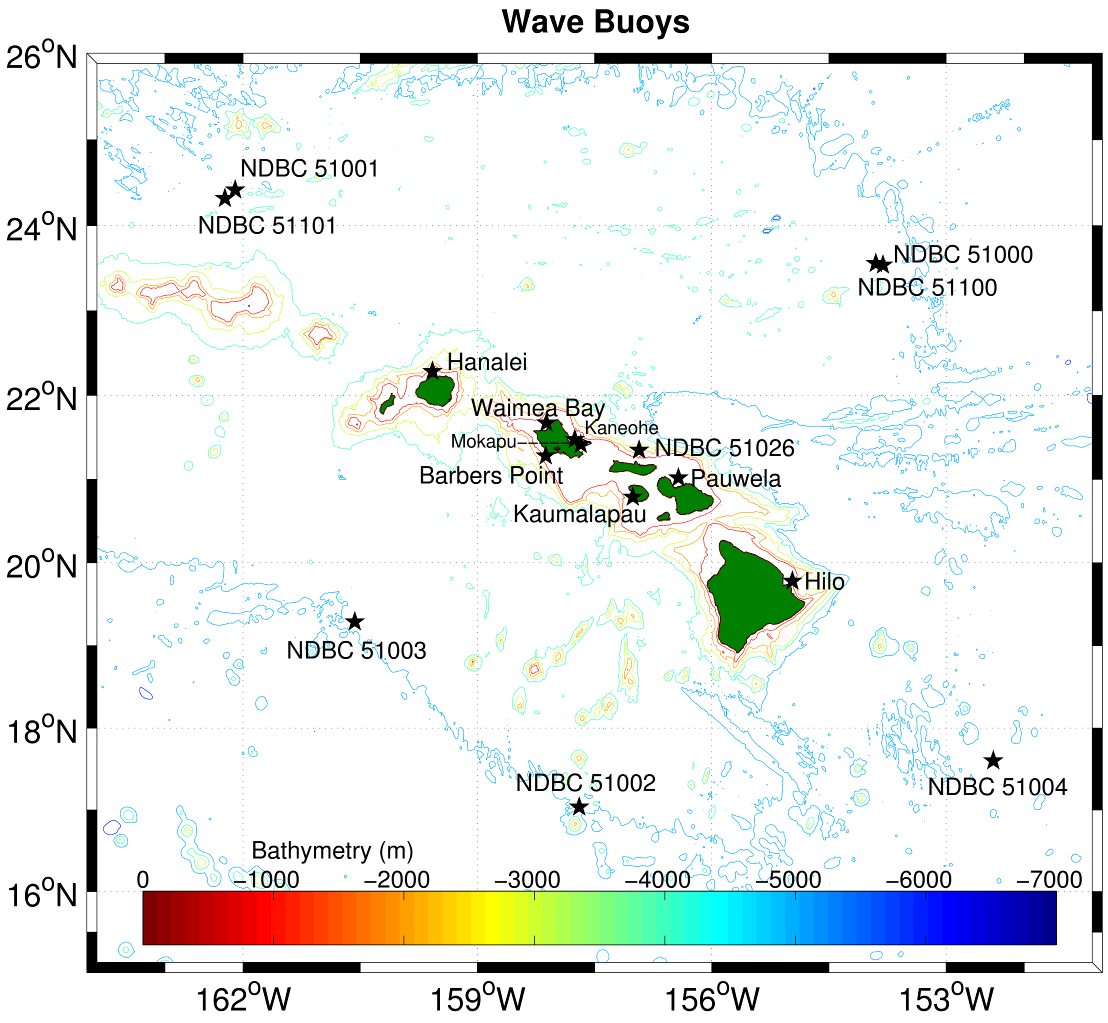

Figure 2.1: Map of wave buoy locations where wave buoys are indicated by black stars.

The Datawell Directional Waverider buoys are 0.9-m metallic floating spheres with heave-pitch-roll sensors (accelerometers) to measure wave energy and infer wave direction. Buoy movements get corrected to a fixed x-y-z reference frame; it has a better signal-to-noise ratio than buoys that use pitch-roll directly to estimate directional wave properties. The Waverider measures waves with periods from 1.6 to 30 seconds, with an error of no more than 3%. The buoys are tethered by moorings that are a combination of a bungee and chain anchoring systems (Figure 2.2). For NDBC and NODC buoys, the choice of hull type (foam or discus) used usually depends on its intended deployment location and measurement requirements. To assure optimum performance, a specific mooring design is produced based on hull type, location, and water depth. The discus buoys have 3 meter circular hulls that very cost-effective. Since it is constructed of aluminum, it is less likely to corrode, and compass measurements are not affected.

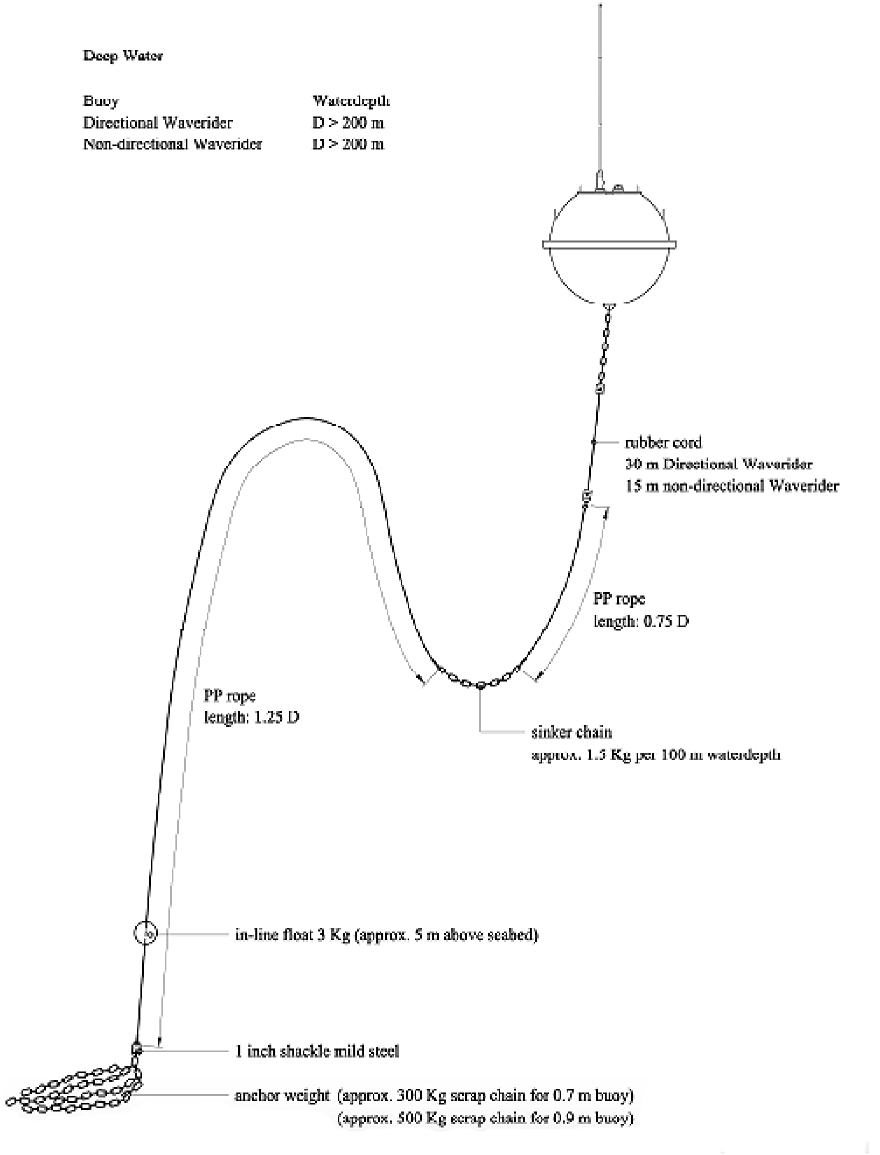

Figure 2.2: Mooringline layout for the Datawell Waverider Buoy.

The data from the buoys have been used to validate wave models (e.g. SWAN, Li et al. (2016)), but few studies have used the wave buoy network to examine the wave field around the Hawaiian Islands. Using satellite altimeter data, Flament et al. (1996) produced averages of the offshore combined sea and swell heights around the Hawaiian Islands as a function of season. Fletcher et al. (2002) detailed a history of high-surf events for the various shores of Oahu and ranked the hazard potential in the coastal zones of all the main Hawaiian islands. Aucan (2006) used the Waimea buoy to derive a directional wave climatology for the north shore of Oahu based on 4 years of data in addition to 45 years of wave model reanalysis output.

2.5 Baldwin Beach, Maui Island

The wave climate has an important impact on coastal regions influencing the sediment transport, runup, and groundwater. Understanding these connections necessary for coastal managers and stakeholders (Moberly and Chamberlain, 1964; Pérez et al., 2014). Beaches around the Hawaiian Islands get covered and uncovered by the short and long wave-induced water level fluctuations in an area named the swash zone. The understanding of this region is fundamental to predict beach erosion and inundation during both extreme and mean wave conditions.

Coastal erosion is the natural shoreline response to a rising sea level by landward displacement of coastal environments causing erosion of the upland (Bruun, 1962; Fletcher et al., 1997). Beach erosion, a volumetric loss of sediment from the beach, occurs when the sand supply is decreased and/or when erosion is refocused away from the upland and onto the adjoining beach. Hence, artificially fixing the shoreline with seawalls and revetments removes upland sand from the sediment budget, and reduces sand supplies to the beach (Plikey and Wright, 1988; Kraus, 1988). Furthermore, it can be expected that the effects of climate change (e.g., sea level rise and possible storm intensification) will produce more drastic beach loss (Bruun, 1962; Kraus, 1988; Tait and Griggs, 1990; Hall and Pilkey, 1991). Active seawalls and revetments may enhance scouring in front of and flanking such structures during an erosive event (Komar and McDougal, 1988; Morton, 1988; Lipp, 1995) and, on a sand-starved beach, will compromise the ability of a beach to recover after an erosive event (Morton, 1988).

The water level depends on sea level variations associated with winds and ocean currents, astronomical tides, the setup that elevates the mean shoreline position and the runup of individual waves beyond that mean level due to momentum transfer of breaking waves to the water column occurring on a time scale of seconds. The cross-shore gradient of the radiation stress is balanced by a sloping water level, causing setdown outside the breaker zone and setup inside the surf zone and at the coast (Longuet-Higgins and Stewart, 1963). Appreciable setup at the shoreline can last for several days, depending on the duration of energetic swell events.

The other factor important to the occurrence of property erosion is the morphology and size of the fronting beach, and its capacity to serve as a buffer between the attacking waves and properties. The overall size of the beach, governed by the quantity of sediment, largely determines its buffering ability, but morphological elements such as the development of rip current embayments can also locally determine the width of the beach. The morphology of the beach can be characterized as ranging from dissipative to reflective (Wright and Short, 1983), depending on the sediment grain size, beach slope, and wave parameters. Depending on the magnitude of the fall velocity and the wave characteristics, a sand grain may move either onshore or offshore (Dean and Dalrymple, 1991). This classification relates to the dissipation of wave energy, the dynamic response of the beach morphology, and ultimately to the natural capacity of the beach to protect coastal properties (Ruggiero et al., 2001).

The investigation of the physics of the transient, shallow, turbulent and multi-phase swash flow is a challenge in terms of the fluid mechanics, and in addition conducting measurements in this region is very difficult (Puelo et al., 2012). In general, depth-resolving models provide a better description of the flow during the backwash, at a high computational cost. The infiltration and exfiltration of fluid into the sediment is believed to play an important role in boundary layer dynamics, sediment transport, and run-up, but this is yet to be quantified experimentally. For example, it is clear that the infiltration influences the run-up and flow velocity, which would have direct consequences for sediment transport (Briganti et al., 2016).

This study examines data collected from Baldwin Beach, on the north shore of Maui Island in the Hawaiian Islands to develop a better understanding of how these processes are connected to wind-wave variability.

3 | Wave Buoys

3.1 Wave Buoy Data

To process the PacIOOS spectral wave buoy data from CDIP, I compute directional spectrum for each station following Lygre and Krogstad (1986). The coefficients of the directional Fourier series are used to create complex directions and then used to determine angles of energy by

$$c_1 = a_1 + ib_1 \tag{3.1}$$

$$c_2 = a_2 + ib_2 \tag{3.2}$$

$$\phi_1 = \frac{c_1 - c_2 * \bar{c_1}}{1 - |c_1|^2} \tag{3.3}$$

$$\phi_2 = c_2 - c_1 * \phi_1 \tag{3.4}$$

where a_1, a_2, b_1, and b_2 are the Fourier coefficients. The 2-dimensional directional distribution array is calculated by

$$D = \frac{\frac{1}{2\pi}[1 - \phi_1 * \bar{c_1} - \phi_2 * \bar{c_2}]}{|1 - \phi_1 e^{-i\theta} - \phi_2 e^{-2i\theta}|^2} \tag{3.5}$$

where θ is the direction. I then multiply each of the energy density components by the directional distribution value to get the directional spectrum with a 1° resolution.

The final directional spectrum is the average of this energy over 5° bins. The output of these equations give a time series of directional spectrum for each of the directional wave buoys. To get a sense of the seasonality of the energy arriving at each of the buoys, I take the average over the most energetic seasons (summer and winter). Summer in this study is defined as June, July and August. Winter is defined as December, January, and February. Shown here are the results for the Waimea Buoy (Figure 3.1). Results for the other PacIOOS buoys can be found in Appendix A.

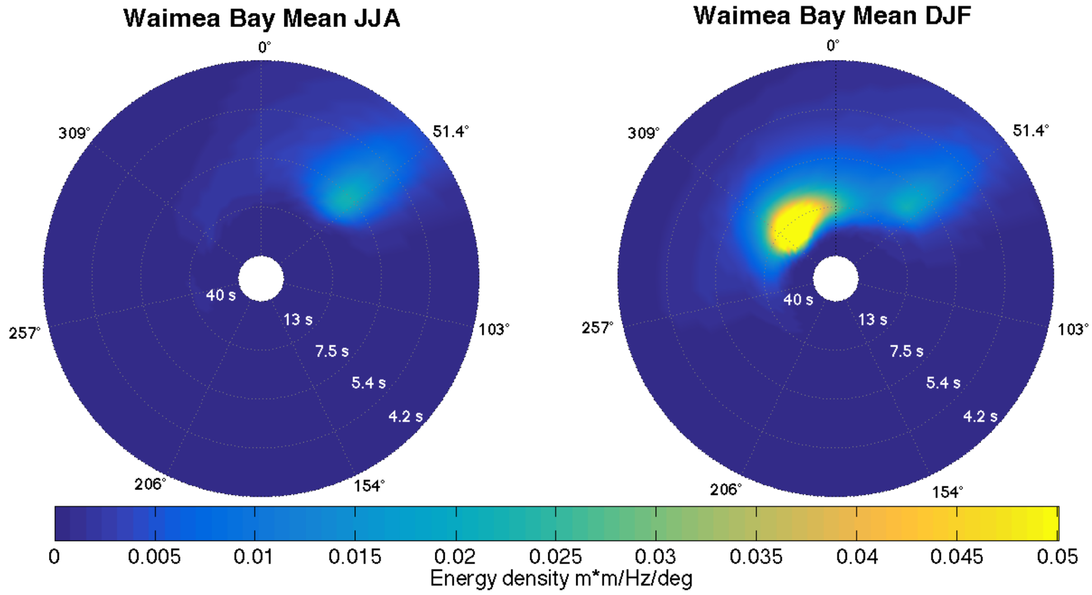

Figure 3.1: Waimea Bay directional spectra. Left: Summer (June, July, August) average. Right: Winter (December, January, February) average.

During the summer at Waimea, the trade wind swell wave energy is from approximately 25-60° over 4-11sec. (Figure 3.1). During the winter there is about ten times more energy coming from the northwest (260-360°, 7-30sec). The peak in winter northwest swell energy is 0.1706 $m * m/Hz/deg$ at 315°, 0.065Hz (15.38sec). From the northeast (50°) there is a trade wind signal likely from the trade wind swell wrapping around the north side of Oahu and arriving at the buoy.

The mean wave period (Ta) can be calculated with these data as

$$Ta = \left[\frac{\int_{f_{min}}^{f_{max}} \int_{\theta_{min}}^{\theta_{max}} S(f,\theta)}{\int_{\theta_{min}}^{\theta_{max}} S(f,\theta)}\right]^{-1} \tag{3.6}$$

where $S(f,\theta)$ is the directional spectra. The significant wave height (H_s) can be calculated by

$$H_s = 4\sqrt{\int_{f_{min}}^{f_{max}} \int_{\theta_{min}}^{\theta_{max}} S(f,\theta) d\theta df} \tag{3.7}$$

The energy flux is a useful measurement when we are studying modulations in the amplitude of waves from a defined direction in coastal regions. It can be computed from the directional spectrum as

$$ef_x = -sin(\theta)\frac{\rho g^2}{2\pi} \int_{f_{min}}^{f_{max}} \int_{\theta_{min}}^{\theta_{max}} \frac{S(f,\theta) * BW}{f} d\theta df \tag{3.8}$$

$$ef_y = -cos(\theta)\frac{\rho g^2}{2\pi} \int_{f_{min}}^{f_{max}} \int_{\theta_{min}}^{\theta_{max}} \frac{S(f,\theta) * BW}{f} d\theta df \tag{3.9}$$

where ρ is the density of water ($1029\ \frac{kg}{m^3}$), g is gravity, f is frequency, θ is direction, and BW is the band width. The negative sign is included so that positive flux is in the direction of wave propagation.

To process the NDBC buoys that have frequency, but no direction, I first sort out the frequency range 0.033-0.33Hz. We use a broad frequency range, because the old NODC buoys do not account for frequency in their measure of significant wave height. To get the significant wave height for the NDBC buoys we follow:

$$H_s = 4\sqrt{\int_{0.033Hz}^{0.33Hz} S(f) * BW df} \tag{3.10}$$

where $S(f)$ is the nondirectional spectrum. After using a dispersion solver (C.S. Wu.), the wave speed (c) is given by

$$c = \sqrt{\frac{g * tanh(akk)}{dkk}} \tag{3.11}$$

where akk is the wave number times depth, and dkk is the wave number. Group speed (c_g) is given by

$$c_g = \frac{1}{2} * c * \frac{1 + (2 * akk)}{sinh(2 * akk)} \tag{3.12}$$

and energy flux (ef) in kW/m is given by

$$ef = \frac{1}{1000} * \frac{1}{8}\rho g \int_{f_{min}}^{f_{max}} S(f) * c_g df \tag{3.13}$$

The NODC buoys have significant wave height and dominant wave period (spectral peak period in seconds to tenths), but no frequency or direction. Each variable is available as a 1-dimensional time series. The energy flux is computed following Dean and Dalrymple (1991) by taking the product of the energy and the group speed:

$$E = \frac{1}{8}\rho g H_s^2 \tag{3.14}$$

$$c_g = \frac{g * T_p}{4\pi} \tag{3.15}$$

$$ef = E * c_g \tag{3.16}$$

where T_p is the dominant wave period.

Figure 3.2 shows time series of the energy flux from buoys that experience a northwest swell. We can see that the maximum amplitude of the winter significant wave heights at each buoy modulates with time. In summer the average significant wave height is about 0.6m and in the winter it is about 2.5m.

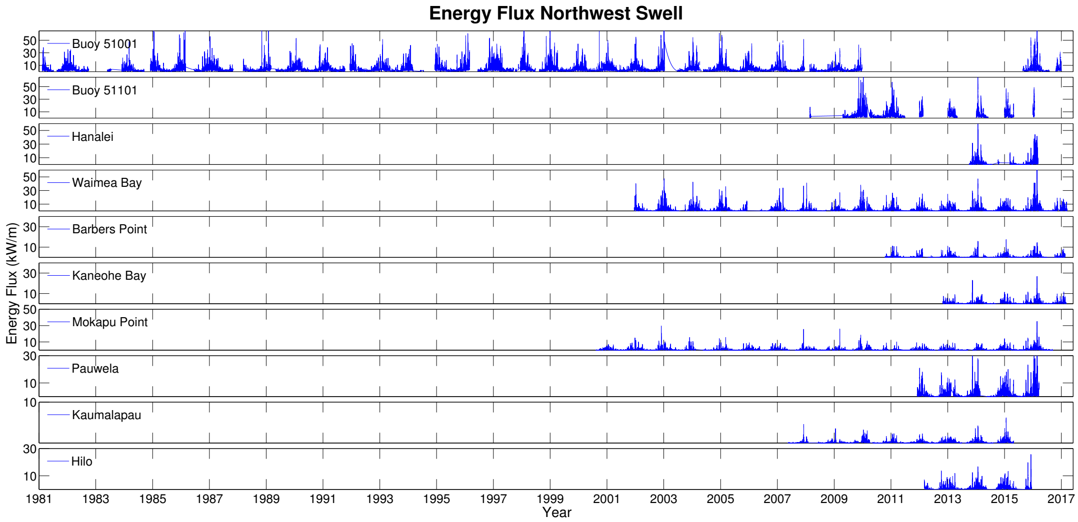

Figure 3.2: Energy flux for the northwest swell from wave buoy data. Top to Bottom: Buoy 51001, Buoy 51101, Hanalei, Waimea, Barbers Point, Kaneohe Bay, Mokapu Point, Pauwela, Kaumalapau, and Hilo.

To create a long record for the northwest swell, I merge the energy flux data to make a single time series. The PacIOOS directional spectrum data are considered to be of the highest quality and buoy data of this type are chosen first if available for a given time. For energy flux, The NODC data from buoy 51001 are chosen if PacIOOS data are not available. If that is not available, NDBC 51001 and then NODC 51001 and then NDBC 51101 are chosen. The northwest swell data are offset so that winter (DJF) means at each buoy match the Waimea buoy. The NODC and NDBC data does not account for swell direction, so the time period with these data sources may not do a good job capturing real signals for swell types. These buoys also have a lot more gaps in the data that can miss measurements of large swell events. Figure 3.3 shows the data sources that are used to create a single, long time series for the NW swell.

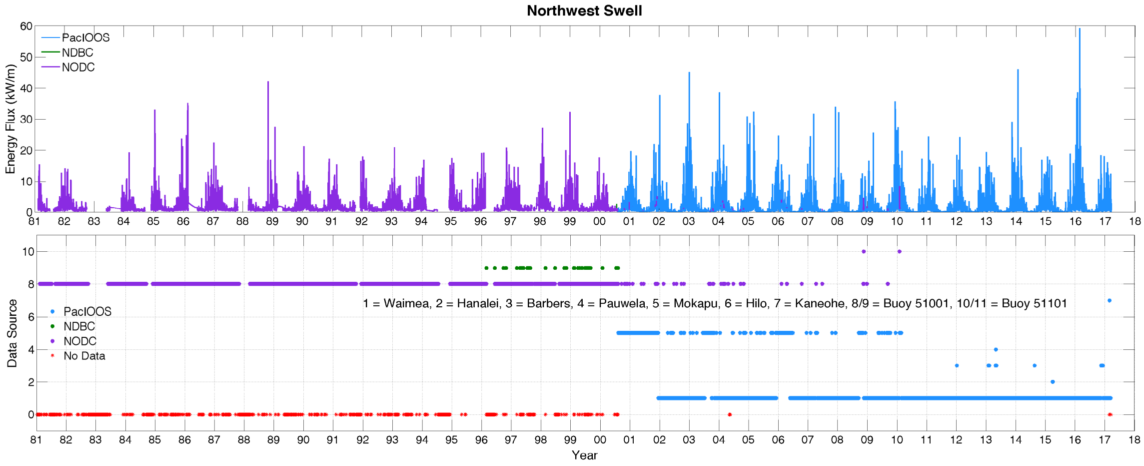

Figure 3.3: Merged time series of wave buoy data. Top Panel: Energy flux. Bottom Panel: The data source that was used at each point in time to create the merged time series shown above. The purple portion of the time series indicates nondirectional buoy data and blue indicated directional.

3.2 SWAN

To evaluate the accuracy of the long wave buoy time series for the northwest swell, we compare our measure of significant wave height to a 34-year hindcast model of spectral wave output (Li et al., 2016) at the Waimea Buoy location. We use significant wave height, because later we compare our wave buoy time series to a observational dataset of wave height. This model is the SWAN model adapted to the tropical island environment by (Filipot and Cheung, 2012). For the overlapping time period, the DJF average winter datasets have a correlation of r = 0.6362, p = 6.91 x 10^{-5} (Figure 3.4). If we just compare the PacIOOS (2000-2017) portion of the data to the model, the correlation increases to r = 0.9503, p = 2.23 x 10^{-7}. The poor agreement between the SWAN hindcast and NDBC/NODC portion of the time series suggests that the SWAN hindcast is inaccurate during this time period, or that the NODC/NDBC data are. The buoy data have many gaps, do not account for swell direction, and are also further from the islands than the PacIOOS buoys so it may be that something is happening to the energy between the NDBC/NODC buoys and Waimea.

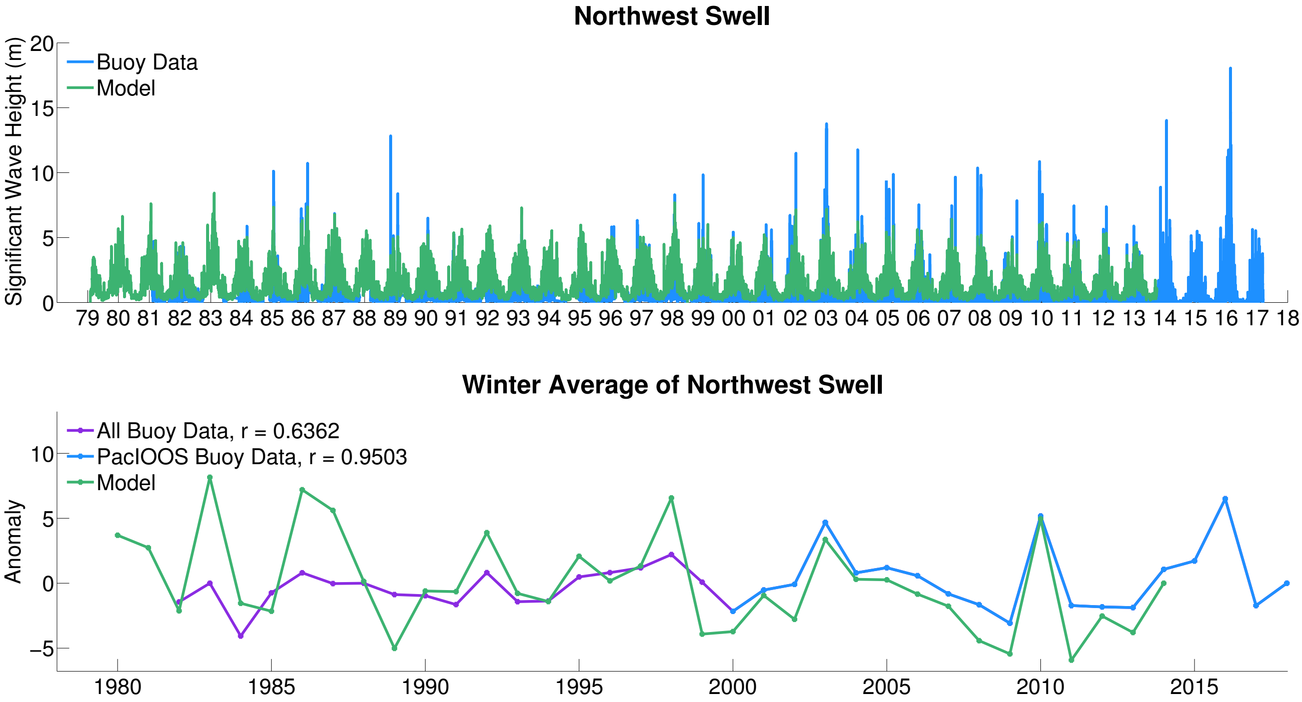

Figure 3.4: Top: In light blue is the buoy data that has been combined to create a long time series for the northwest swell. In green is the SWAN model output at the Waimea Buoy location. Bottom: Winter averages of the above time series. In purple is the portion of the wave buoy time series that comes from the NODC or NDBC records. In the legend are the correlation values between the green model output, the 1981-2017 buoy time series, and the 2000-2017 PacIOOS buoy time series.

3.3 Goddard and Caldwell Dataset

Since 1968, daily visual observations of surf heights on Oahu have been recorded at select locations by various entities and made publicly available. The primary observers have been the City and County of Honolulu lifeguards and employees of the Surf News Network Inc. From 1968 through September 1987, Mr. Larry Goddard recorded the daily observations to create a digital dataset. Since September 1987, Mr. Patrick Caldwell has been recording the daily values (Caldwell, 2005). In this dataset, referred to as the Goddard and Caldwell (GC) dataset, the single value that is logged daily represents the highest waves reported on the north shore of Oahu. Wave heights are reported in a measurement unique to Hawai‘i called the Hawai‘i standard feet (Hsf). One approach to convert Hsf to trough-to-crest wave height is to assume the Hawai‘i scale height represents one-half of the height at the moment of highest cresting for the section along the wave front of greatest peakedness. Another approach is that the Hawai‘i scale height represents two-thirds of the average wave front, trough-to-crest height from the highest peak to the lower wave shoulder. When the surf is large (greater than 15 Hsf), the former view approaches two-thirds, while the latter assumption nears unity (Caldwell, 2005). This study assumes we are looking at large waves and uses unity to convert heights to meters.

Sunset Point is usually the observing location with the highest breakers during surf episodes up to roughly 15 Hsf, while Waimea Bay is the reporting spot for very large surf occurrences above 15 Hsf. The daily GC value represents the high end of the range as given in the reports (Caldwell and Aucan, 2007). For recent years, digital video cameras have been maintained at Sunset Point and Waimea Bay and made available via the Internet. This allows an opportunity to cross-check the lifeguard and Surf News Network reports and also to acquire late-day observations under rising swell conditions. Estimating the breaker heights as seen on the cameras requires experience. Presently, this information is utilized only when Patrick Caldwell makes the estimate (Caldwell, 2005). The dataset is publicly available online from 1968 to 2004 at the time of this study (Caldwell and NESDIS, 2011). Patrick Caldwell was a supporter of this research and provided the updated data that have not been published yet (1968 to 2017).

The GC surf heights are compared to the NW swell significant wave heights from the buoy observations and from the SWAN model hindcast (Figures 3.5-3.6). The GC heights have been offset so winter wave heights match those at the Waimea buoy. We find that the GC wave heights correlate well with the buoy data during the period of PacIOOS directional buoy observations ($r = 0.9774$, $p = 8.4673 \times 10^{-7}$), but not during the nondirectional NODC/NDBC period ($r = 0.6077$, $p = 5.8 \times 10^{-3}$). In addition, the GC wave heights are highly correlated ($r = 0.9167$, $p = 6.1121 \times 10^{-9}$) with the SWAN model output. We conclude that the nondirectional buoy observations are not representative of the NW swell at Waimea for the reasons mentioned previously. In particular, we suspect that the numerous gaps in the directional buoy data lead to sampling errors when constructing the DJF averages. Henceforth, we use the GC dataset combined with the directional wave buoy data to represent NW swell significant wave height at Waimea.

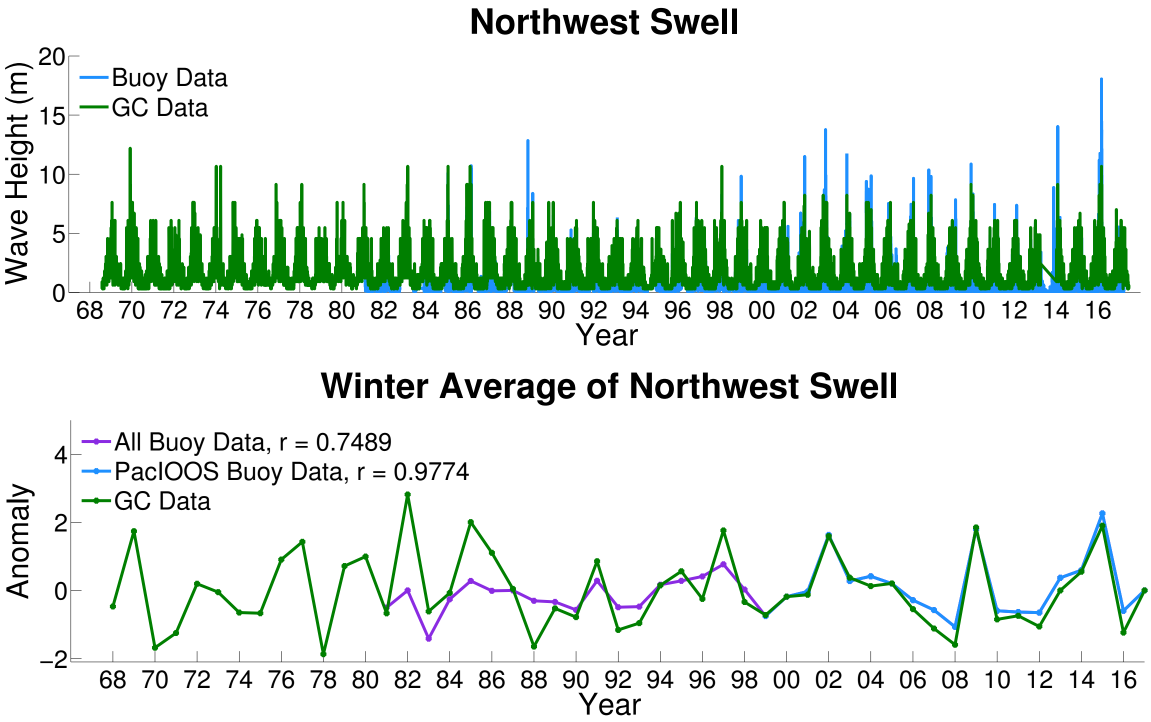

Figure 3.5: Top: In light blue is the buoy data that has been combined to create a long time series for the northwest swell. In green is the GC record of wave heights for the northwest swell. Bottom: Winter averages of the above time series. In purple is the portion of the wave buoy time series that comes from the NODC or NDBC records. In the legend are the correlation values between the green GC, the 1981-2017 buoy time series, and the 2000-2017 PacIOOS buoy time series.

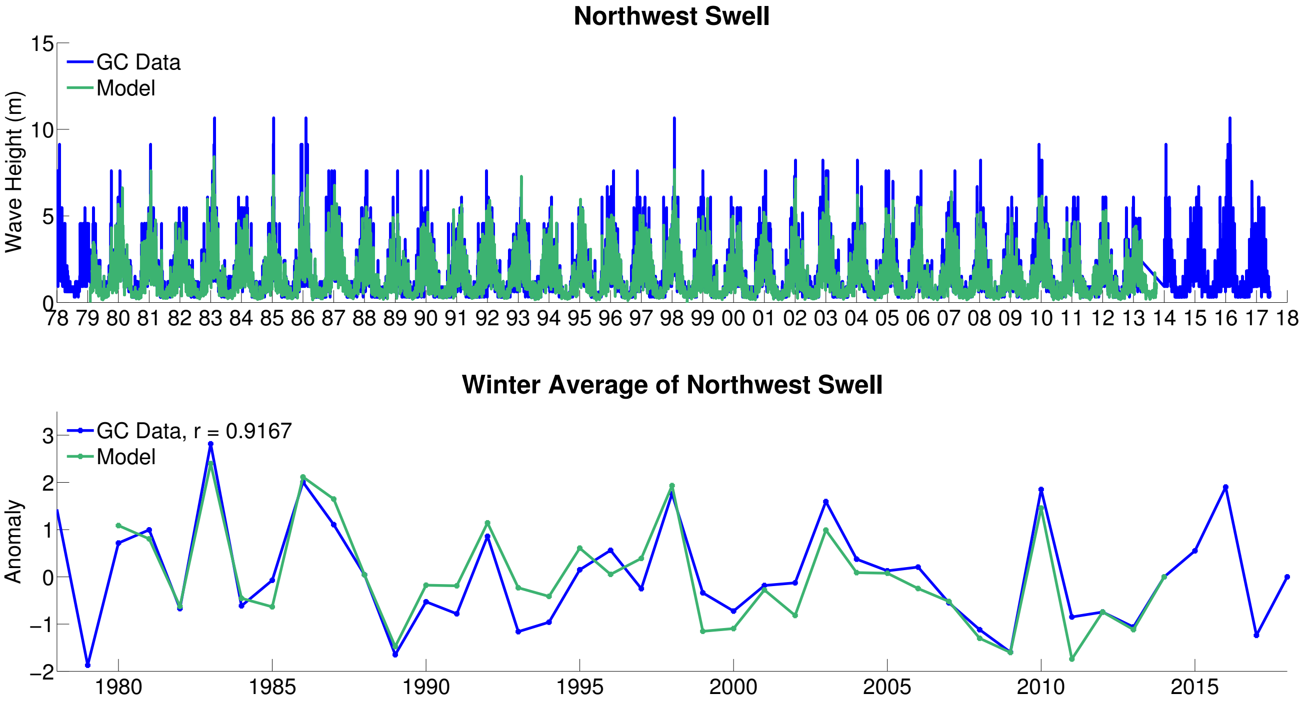

Figure 3.6: Top: In dark blue is the GC data for the northwest swell. In green is the 34-year hindcast model of spectral wave output data at the Waimea Buoy location. Bottom: Winter averages of the above time series. In the legend is the correlation values between the green model output and the GC time series.

Time series of the computed significant wave height are given in Figure 3.7. More information about the trade wind swell and the south swell can be found in Appendix 1. The northwest swell data are offset so that the mean for winters (DJF) matches the mean for winters at the Waimea buoy. The PacIOOS directional spectrum data are considered to be of the highest quality and buoy data of this type is chosen first if available for a given time. The GC data from the north shore observations is chosen if PacIOOS data are not available. GC is chosen over SWAN because it covers a longer time period and it has a higher correlation to the PacIOOS buoy data of 0.9774 (Figure 3.5). Figure 3.8 shows the data sources that are used to create a single, long time series.

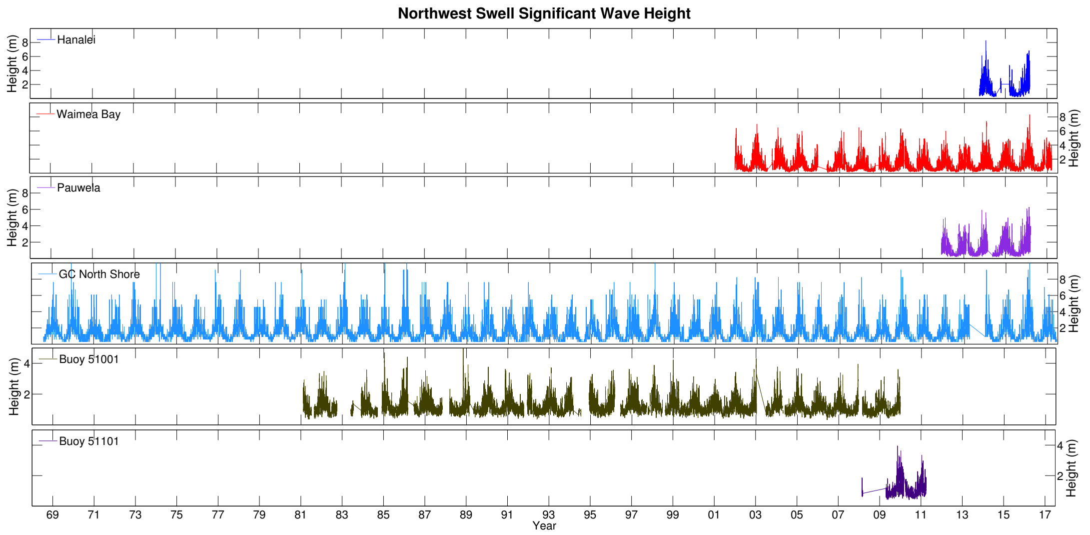

Figure 3.7: Significant wave height for the northwest swell. Top to bottom: Significant wave height data from the Hanalei buoy in dark blue, Waimea Buoy in red, Pauwela buoy in purple, Goddard and Caldwell surf observations in light blue, buoy 51001 in black, and buoy 51101 in dark purple.

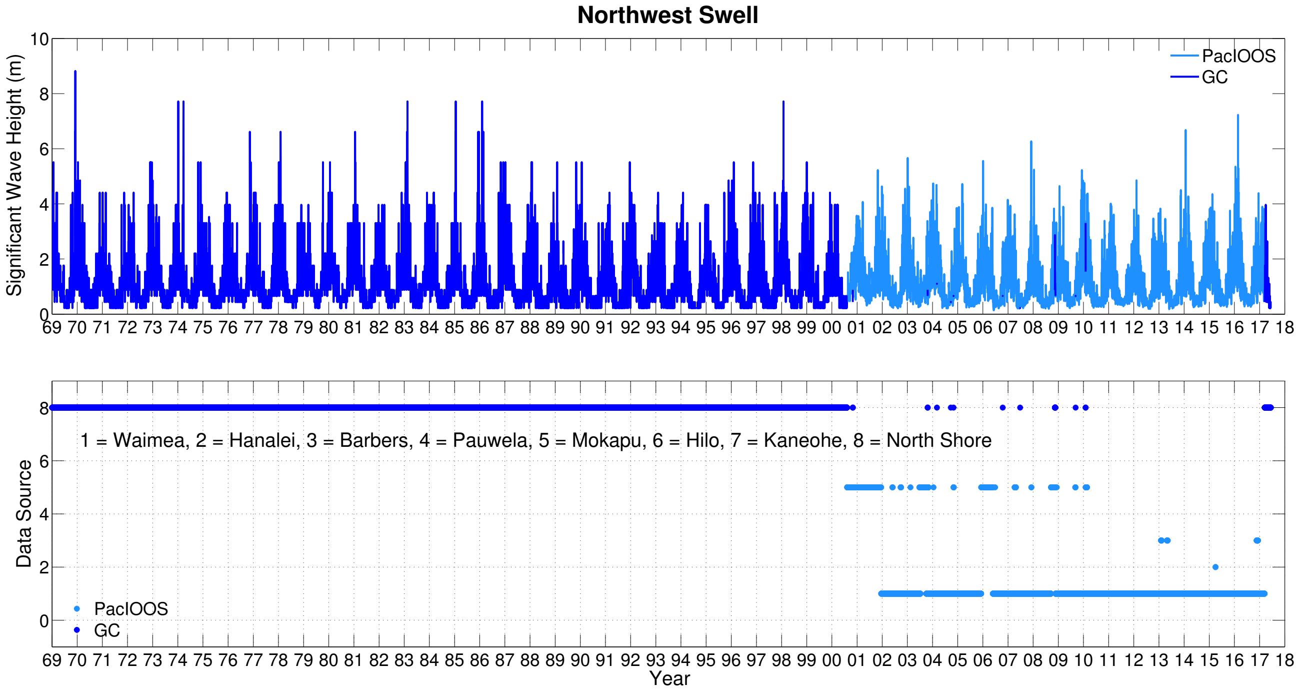

Figure 3.8: Merged time series of wave buoy data. Top Panel: Significant Wave Height, Bottom Panel: The data source that was used at each point in time to create the merged time series shown above.

3.4 Climate Indices

Modulations in the Pacific climate can influence the resulting winter swell that appears in the Hawaiian Islands. For this study we examined the relationship between winter wave heights and the following climate indices: North Pacific Oscillation, Pacific Decadal Oscillation, Arctic Oscillation, Pacific North American Index, Niño 3.4, and the North Pacific Index. Climate indices are a useful way to capture the interannual to decadal variability in large regions like the north Pacific.

A comparison to the winter averages of our northwest swell time series to each of these climate indices (Figure 3.9) gives significant correlations for the North Pacific Index ($r = -0.8062$, $p = 1.61 \times 10^{-12}$), Niño 3.4 ($r = 0.6381$, $p = 6.18 \times 10^{-7}$), and the Pacific/North American Index ($r = 0.7310$, $p = 1.66 \times 10^{-9}$). Correlations to NPO, PDO, and the AO are not significant in this study. These significant climate indices describe sea level pressure and the jet stream in the north Pacific so it is likely that modulations in these forcings are related to the wave heights seen in the Hawaiian Islands.

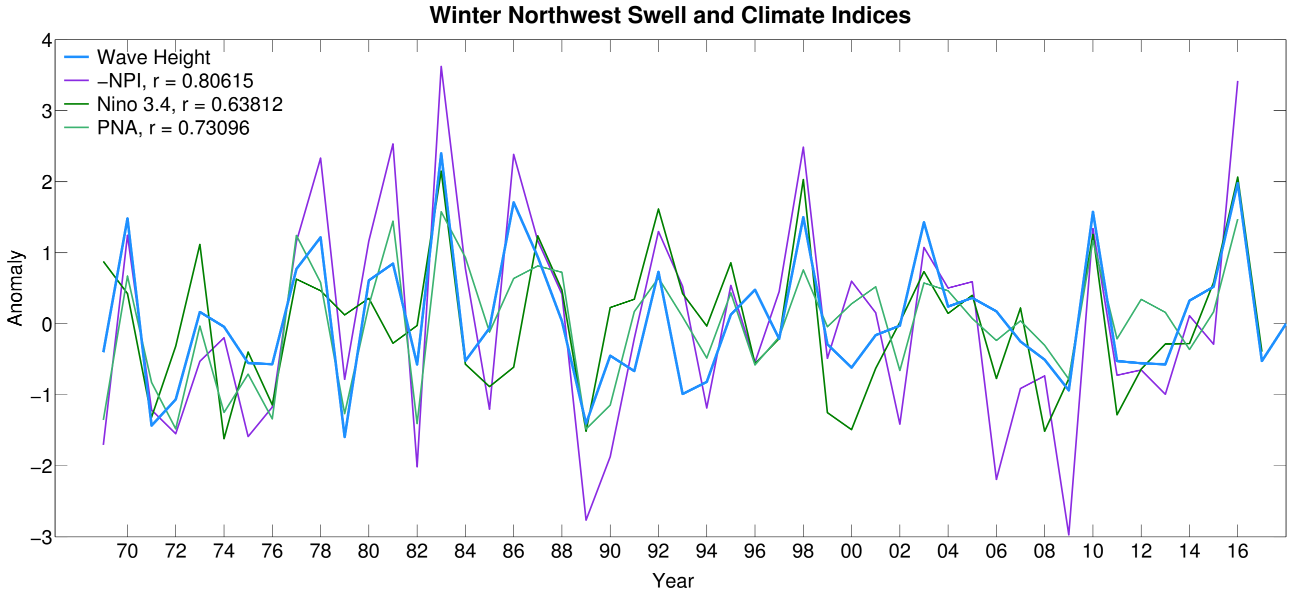

Figure 3.9: Comparison of the winter (DJF) anomalies in wave height, the North Pacific Index, the Niño 3.4 index, and the Pacific North-American Teleconnection Index. Wave height here is from the GC dataset until 2000 and then PacIOOS buoy data after 2000. Correlation values between each index and the wave heights are given in the legend.

A correlation map between the winter averaged sea level pressure (SLP) time series (1993-2011) at each CFSR model gridpoint (Saha et al., 2010, 2014) is shown in Figure 3.10. The highest correlation is r = -0.91, p = 6.14 x 10^{-8} between the sea level pressure and wave height at 42.5°N, 150°W indicated by the purple dot on the map. Also on the map, is the NPI region outlined in black. NPI was the climate index that had the highest correlation to winter waves (Figure 3.9). Since NPI is the average of SLP in the box shown on the map, and that box encompasses the region of highest correlation between winter SLP and wave height, it makes sense that the NPI would have a high correlation value. Shown in Figure 3.11 are the time series of winter wave height and the SLP time series from 42.5°N, 150°W from three different models. In all cases, the correlation is high. The National Centers for Environmental Prediction (NCEP) model extends backward in time before the wave record and gives us some insight into how the waves might have been in Hawai‘i before observations began.

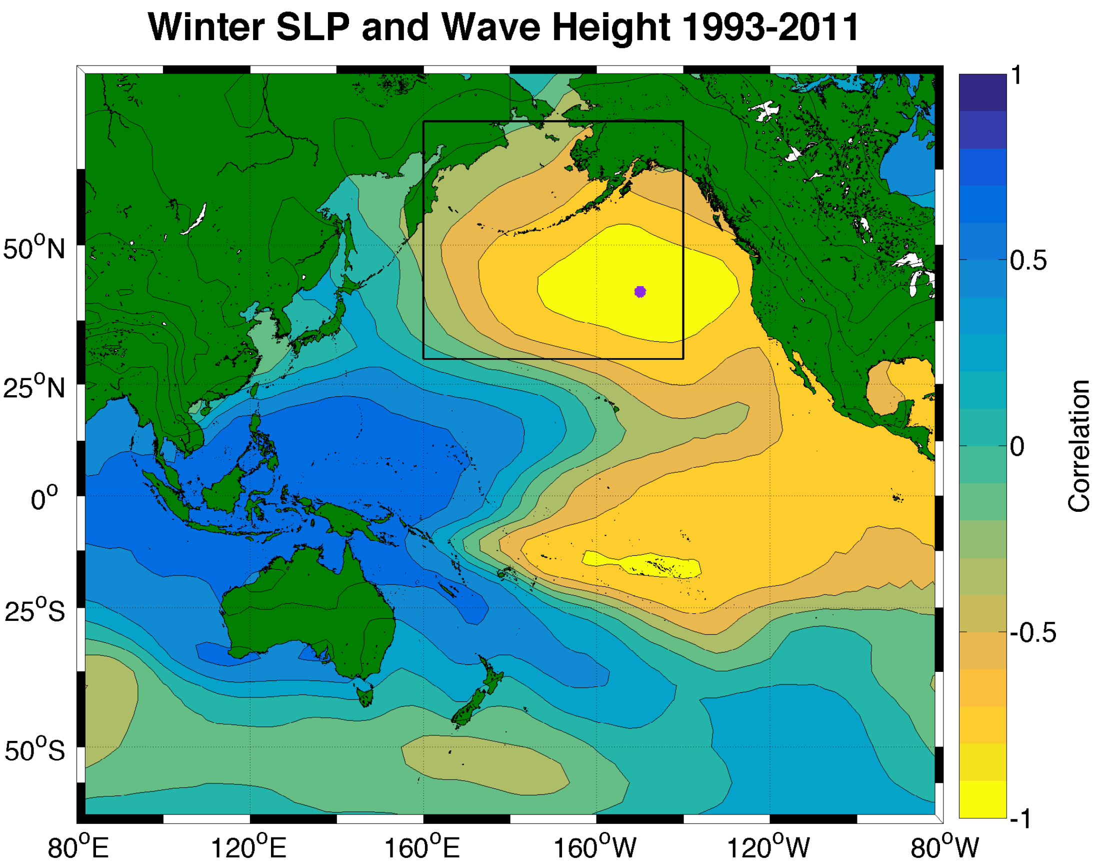

Figure 3.10: Correlation values between winter (DJF) average of SLP for each year during 1993-2011 and winter averages of northwest swell wave height. The highest correlation value is r = - 0.91, p = 6.14 x 10^{-8} at 42.5°N, 150°W shown in purple.

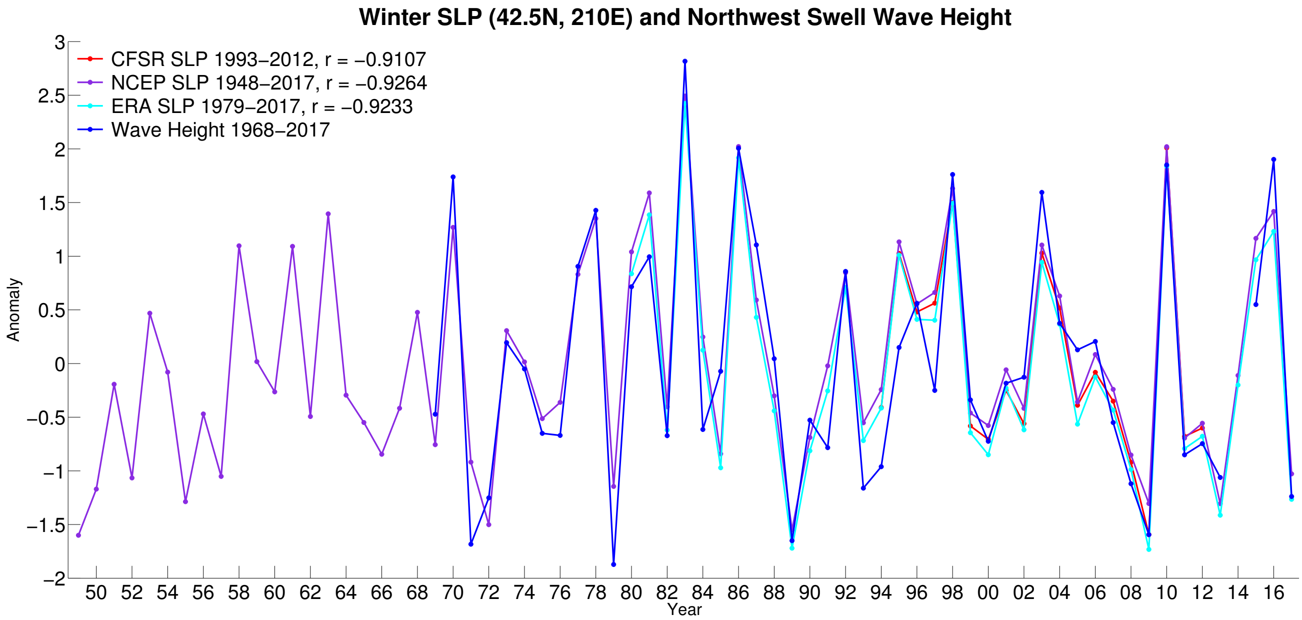

Figure 3.11: Time series of winter (DJF) average of SLP at 42.5°N, 150°W from the CFSR model, NCEP model, and ERA Interim Model. In blue is the winter (DJF) average of the northwest swell wave height. Correlation values between each model and the wave heights is given in the legend.

Physically, this correlation is describing a deepening of the Aleutian Low and the resulting higher wave heights seen in the Hawaiian Islands. We know that a deepening of the Aleutian Low can adjust the east asian jet stream and storm tracks. Storm tracks that are oriented so that they produce wave trains that are in line with Hawai‘i would create larger winter wave heights.

Following Aucan (2006), if we examine the number of extreme events (>4m) and the magnitude of waves during high and low NPI winters, we find that both the number of extreme events and the magnitude of waves increase during low NPI conditions (Figure 3.12).

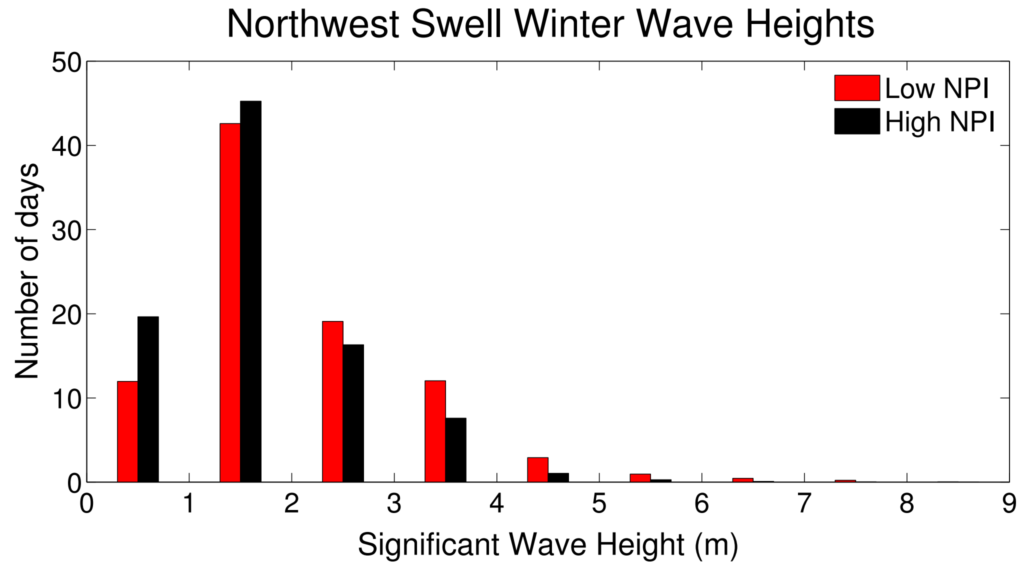

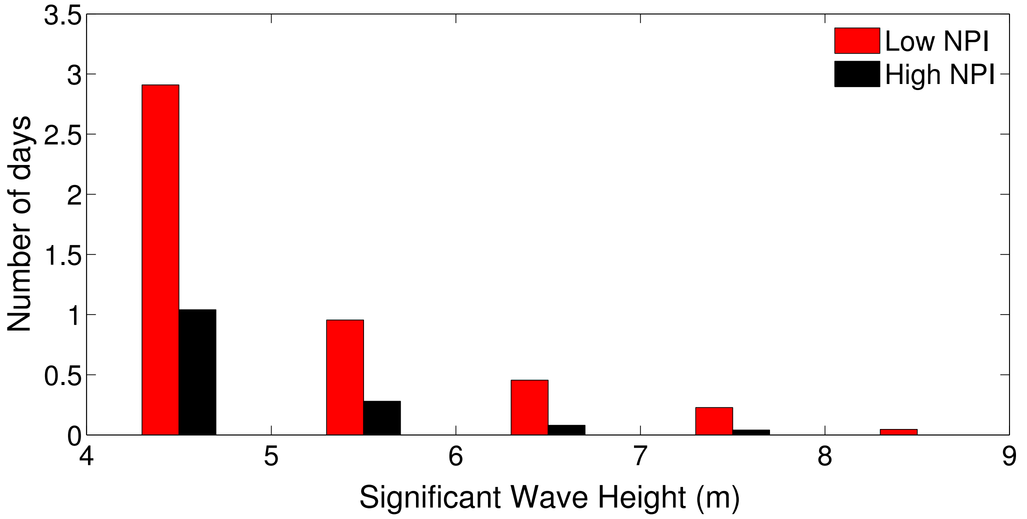

Figure 3.12: Top: Histogram of the number of days at different wave heights on the north shore of Oahu under low and high North Pacific Index (NPI) conditions. Bottom: Histogram of the number of days at wave heights greater than 4m on the north shore of Oahu under low and high NPI conditions.

Another climate index that had a high correlation with winter waves at Hawai'i was the Niño 3.4 index (r = 0.64, p = 6.18 x 10^{-7}). In the Pacific there is an atmospheric bridge (Alexander et al., 2002) that carries circulation perturbations from the tropics, captured by Niño 3.4, to the north Pacific where the Aleutian Low modulates storm tracks that make waves that come to Hawai'i. The bridge occurs through changes in the Hadley and Walker cells, Rossby waves, and interactions between the quasi-stationary flow and storm tracks (Trenberth et al., 1998). After year 2000, the correlation between the Niño 3.4 index and wave heights goes up. This might suggest that the strength of the atmospheric bridge is variable and has been stronger and more closely linked to NPI since 2000.

To understand the wave climate further and the way variations in SLP in the north Pacific result in variable wave conditions, we find the source of Hawai‘i's waves in Chapter 4 using a model and examine the impact SLP has on the storm tracks in the source region.

4 | The ESTELA Model

In order to understand why waves and their energy flux change in the Hawaiian Islands, we must understand changes that are occurring in the generation of the waves. To expand the study of a swell to its source point we use the ESTELA (Evaluating the Source and Travel-time of the wave Energy reaching a Local Area) model. Once the source regions for waves are known, we look at how forcings change in that region and how they relate to the energy flux arriving in the Hawaiian Islands.

4.1 Model Description and Results

The ESTELA (Evaluating the Source and Travel-time of the wave Energy reaching a Local Area) model was developed by Pérez et al. (2014). It is designed to find source points of effective wave energy for a given target point. The model provides information such as where the energy is generated or dissipated, and how long it takes to arrive at the given target point. For this study, the target points are the waves buoys described in Chapter 3.

To run ESTELA, model hindcast wave data are required. In this study, a global wave parameter database (Rascle et al., 2008; Rascle and Ardhuin, 2012) has been used. This database was obtained by the numerical wave model WAVEWATCH III in its version 4.04 forced by winds from the Climate Forecast System Reanalysis (Saha et al., 2010). The wave spectrum of the model is discretized using 24 directions and 31 frequencies and the results are provided in a spatial grid at 0.5° resolution and 3-h time resolution. The available catalogue from this hindcast includes parameters such as significant wave height, peak period, mean direction and directional spread for up to six partitions of the spectrum, the wind sea and five swell trains in the more general case. In this study, we use 20 years, from 1993 to 2012, of wave spectra reconstructed from these partitions.

The first step is to apply geographic criteria to limit the study area to wave systems that are not separated from the target point by land. These criteria rely on the assumption that deep water waves travel along great circle paths, which reduces the computational effort in the following steps of the methodology. This assumption has several limitations, however due to the dynamic interaction of waves with their environment. For example, wave-current interactions are not always negligible in deep water, and processes such as refraction and diffraction may be important in shallow waters. The great circle assumption may therefore neglect contributions by energy from some cells located behind groups of small islands or that are partially blocked by land, to overall energy at the target point. In order to take these limitations into account, we only neglect a source point when the area represented by that grid point is clearly blocked by land, i.e. there is a land mass that blocks all the directions in a directional sector $\alpha \pm \Delta$, where α is the direction of the great circle between a source point and the target point and Δ determines the width of the directional sector. We use

$$\Delta = max\Big(5, arctan\Big(\frac{dx/2 + dy/2}{r}\Big)\Big) \tag{4.1}$$

where the minimum Δ is 5°, dx and dy are the spatial resolution of the hindcast, and r is the distance between a source point and the target point. Figure 4.1 gives an example of how the geographic points that meet the criteria of equation 4.1 project onto a map for the Waimea buoy as a target point. Note that the valid area includes all the grid points where the wave energy that reaches the target point can be generated or transformed. The neglected source regions in Figure 4.1 represent areas where wave arrivals are blocked from reaching Waimea by the islands of Kauai and Niihau to the northwest, and by the island of Oahu to the south and southeast.

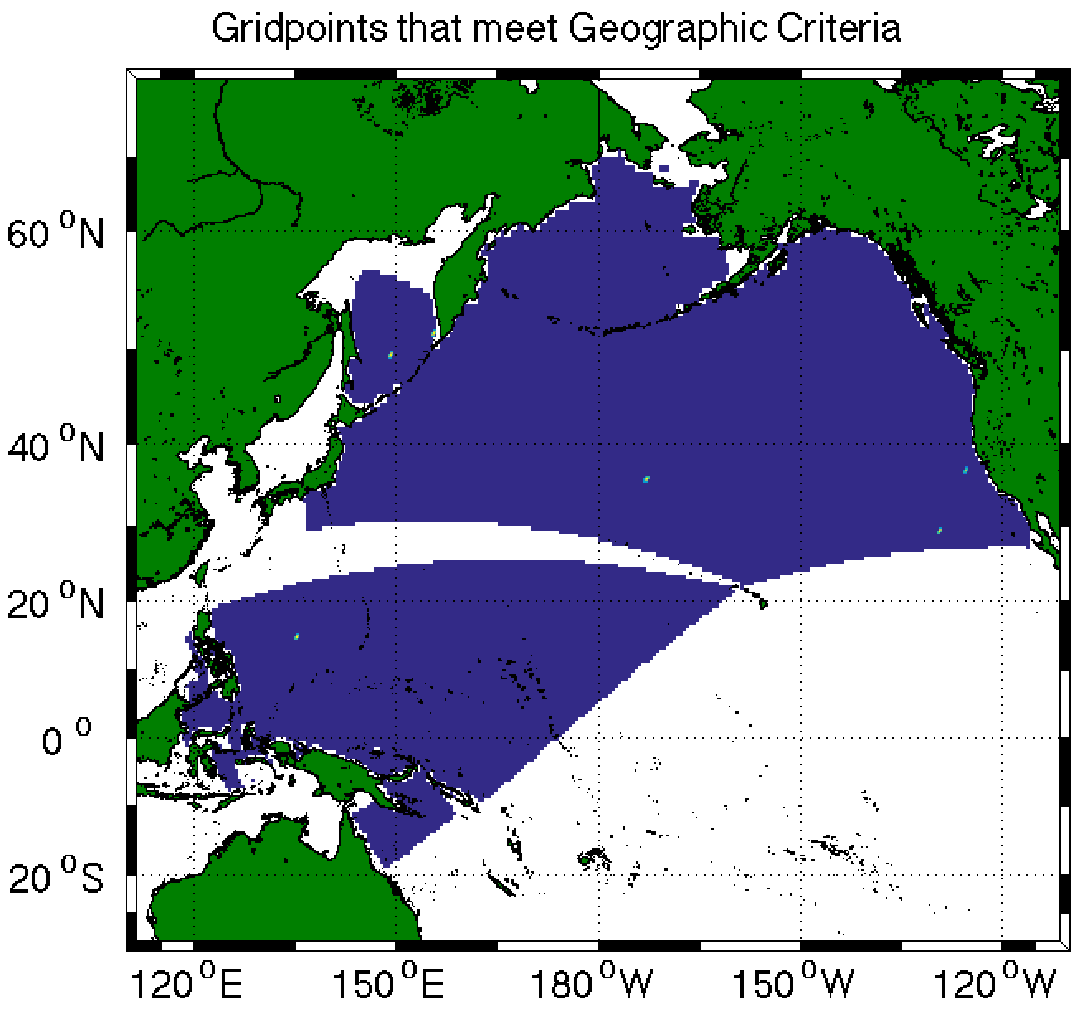

Figure 4.1: Source points (in dark blue) that meet geographic criteria for the ESTELA model with the Waimea buoy as the target point.

The next step is to reconstruct the full frequency-direction spectrum using four parameters obtained from spectral partitioning. Those parameters are significant wave height (Hs), peak period (Tp), mean direction (θ) and directional spread (σ) for one sea and up to five swells $\{Hs_0, Tp_0, \theta_0, \sigma_0 \ldots Hs_5, Tp_5, \theta_5, \sigma_5\}$. Any partition can be viewed as a unimodal spectrum given by its parameters, and the multimodal spectrum can be obtained by aggregation of these unimodal spectra. We reconstruct the frequency-direction spectrum following:

$$E(f, \theta) = \sum_{i=0}^{5} \rho g S_i(f) D_i(\theta) \tag{4.2}$$

where ρ is the water density and g is the acceleration due to gravity. $S_i(f)$ and

$D_i(\theta)$ are the one-dimensional wave spectrum and the directional distribution for a partition i. The one-dimensional wave spectrum $S_i(f)$ is obtained by using a JOint North SeaWAve Project (JONSWAP) spectrum (Hasselmann, 1973), where the amount of energy is determined by Hs_i and the distribution over the frequencies depends on Tp_i. We have used a JONSWAP spectrum shape with a peak enhancement parameter $\gamma = 3.3$, following Pérez et al. (2014). Wave hindcast and testing showed that this assumption has negligible effect in the assessment of the effective wave energy reaching a target point. Regarding the directional distribution $D(\theta)$ we assume a cosine-type expression (Mitsuyasu et al., 1975; Holthuijsen, 2007):

$$D(\theta) = A_2 cos^{2s}\Big(\frac{\theta - \alpha}{2}\Big) for - 180^\circ < \theta - \alpha < 180^\circ \tag{4.3}$$

where θ is the mean direction parameter and α is the direction between the source point and the target point. A_2 and s are two parameters controlling the width of the distribution and depend on the directional spread parameter:

$$s = \frac{2}{\sigma^2} - 1 \tag{4.4}$$

$$A_2 = \frac{\Gamma(s+1)}{\Gamma\Big(s + \frac{1}{2}\Big) 2\sqrt{\pi}} \tag{4.5}$$

In Pérez et al. (2014) an analysis to evaluate the spectrum reconstruction was performed to compare the reconstructed spectra against the original spectra from the numerical model. The evaluation in different locations and periods showed consistent results. Reconstructed spectra capture correctly the directional distribution. The frequency distribution was also represented reasonably well, although some discrepancies were found for the higher frequencies. This was expected since two parameters (θ and α) are used to represent the directional distribution and only one parameter (Tp) is used to represent the frequency distribution.

The last step is to compute the effective energy flux based on the characteristics of the spectrum and the location of the source point and the target point. Here, the effective energy flux is defined as the energy of the spectrum travelling towards the target point at the group velocity, and it is estimated to achieve the Effective Wave Energy ESTELA maps (Figure 4.2, Appendix B). The effective energy is corrected by the viscous dissipation that the waves are expected to encounter during the propagation between the source and target points. In order to evaluate the relative importance of the far-field regions, the effect of other dissipation mechanisms must be taken into account. This can be assessed qualitatively by analyzing the effective energy flux in the downstream points of the great circle path. The position of the source point with respect to the target point is defined by the distance r and the angle α. The spectral density radiated towards the target point is determined by $E_{(f;r,\alpha,t)}$, the cross section through the spectrum $E_{(f,\theta;r,\alpha,t)}$ at the direction α. In order not to overestimate the importance of energy from distant source points, a spatial decay at a rate μ can be considered. A theoretical lower bound for μ in deep water (Dore, 1978; Ardhuin et al., 2009; Collard et al., 2009) is

$$\mu = 2\frac{\rho_a}{\rho_w g c_g}\Big(\frac{2\pi}{T}\Big)^{5/2}\sqrt{2\nu_a} \tag{4.6}$$

where $\rho_a/\rho_w = 0.0013$ is the relation between air density and water density, $c_g = gT/4\pi$ is the group velocity and ν_a is the air viscosity (for a clean surface $\nu_a = 1.4$ 10^{-5} $\mathrm{m^2s^{-1}}$).

Viscous dissipation is responsible for a considerable loss of energy of higher frequencies. Dissipation of lower frequencies, however, is dominated by other processes. Pérez et al. (2014) only corrects viscous dissipation because it can be considered independent of the atmospheric and oceanic conditions during the propagation. Moreover, regions where the loss of energy cannot be explained by viscous dissipation are as interesting as the regions where energy is generated.

The effective energy flux (F) and the travel time (τ) at any time (t) and position (r, α) are then:

$$F_{(r,\alpha,t)} = \int_0^\infty E_{(f;r,\alpha,t)} e^{-\mu r} c_g df \tag{4.7}$$

$$\tau_{(r,\alpha,t)} = r\frac{\int_0^\infty E_{(f;r,\alpha,t)}e^{-\mu r}df}{F_{(r,\alpha,t)}} \tag{4.8}$$

The effective energy flux is the sum of the valid energy fluxes divided by the number of N sea states and the travel time is obtained by using the weighted mean of the group celerity:

$$\overline{F_{(r,\alpha)}} = \frac{\sum_{i=1}^{N} F_{(r,\alpha,t_i)}}{N} \tag{4.9}$$

$$\overline{\tau_{(r,\alpha)}} = r\frac{\sum_{i=1}^{N} F_{(r,\alpha,t_i)}\frac{\tau_{(r,\alpha,t_i)}}{r}}{\sum_{i=1}^{N} F_{(r,\alpha,t_i)}} \tag{4.10}$$

Figure 4.2 shows the effective mean energy flux and travel time to the Waimea buoy over 1993 to 2012. The coloured area shows the effective energy flux (kW/m/degree). Black dashes show the great circles of 16 directional sectors and black contours represent the travel time (τ) in days. Yellow areas represent the regions with the highest wave energy transmitted toward the target point whereas the effective energy of dark blue areas is negligible.

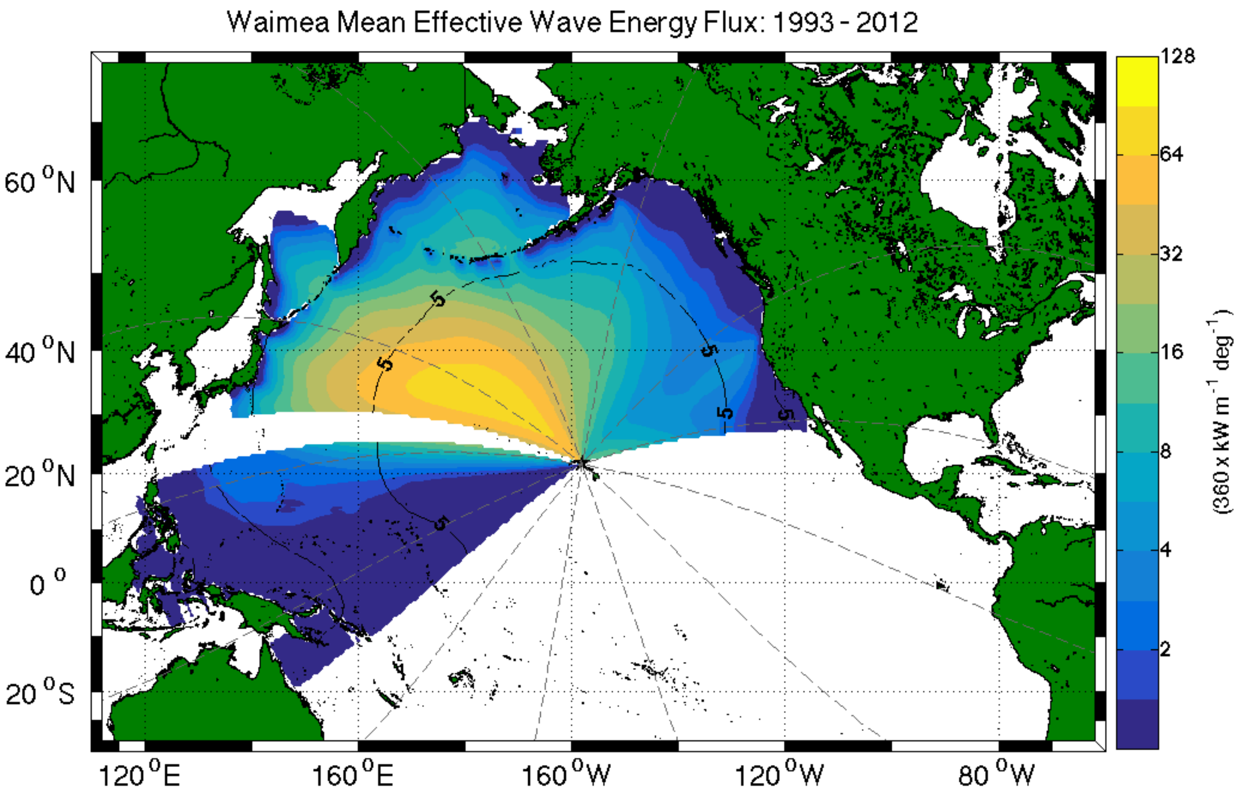

Figure 4.2: Waimea mean effective wave energy flux ESTELA model output.

For wave arrivals at Waimea, Figure 4.2 shows the mean generation regions identified by ESTELA, which highlights the importance of the northwest Pacific. The mean ESTELA map agrees with the directional spectrum at the Waimea Buoy (Figure 3.1). The primary source region in the model output is known to be an area of high storm activity (Bromirski et al., 2005; Graham and Diaz, 2001). A box around this energetic region (25-40°N, 160°E-170°W) will be added to later figures for reference and is called the "source box" from now on. The model output for more buoy locations is discussed in Appendix B.

To examine how the source fields change with season, we take the average of the monthly ESTELA output. In this study, winter is defined as December, January, February, spring is defined as March through May, summer is June through August, and fall is September until November. The spring and fall seasons were found to have little variability that explains changes in energy flux arriving in the Hawaiian islands, so for the purposes of this study we will focus on the winter and summer variability.

In winter, Waimea shows a peak in effective wave energy flux in the source region that is spread out over a larger geographic area than the mean (Figure 4.3). The contours of travel time in days are further distance from the target point than the mean output indicating that these waves travel quickly. During the summer, the northwest source region is very weak and the energy arriving at Waimea from the northeast is easier to see (Figure 4.4). This agrees with the directional spectrum (Figure 3.1). Waimea is on the northwest side of Oahu, so the trade wind energy in the summer wraps around the north point of Oahu before reaching the buoy so it is a weak signal at this location.

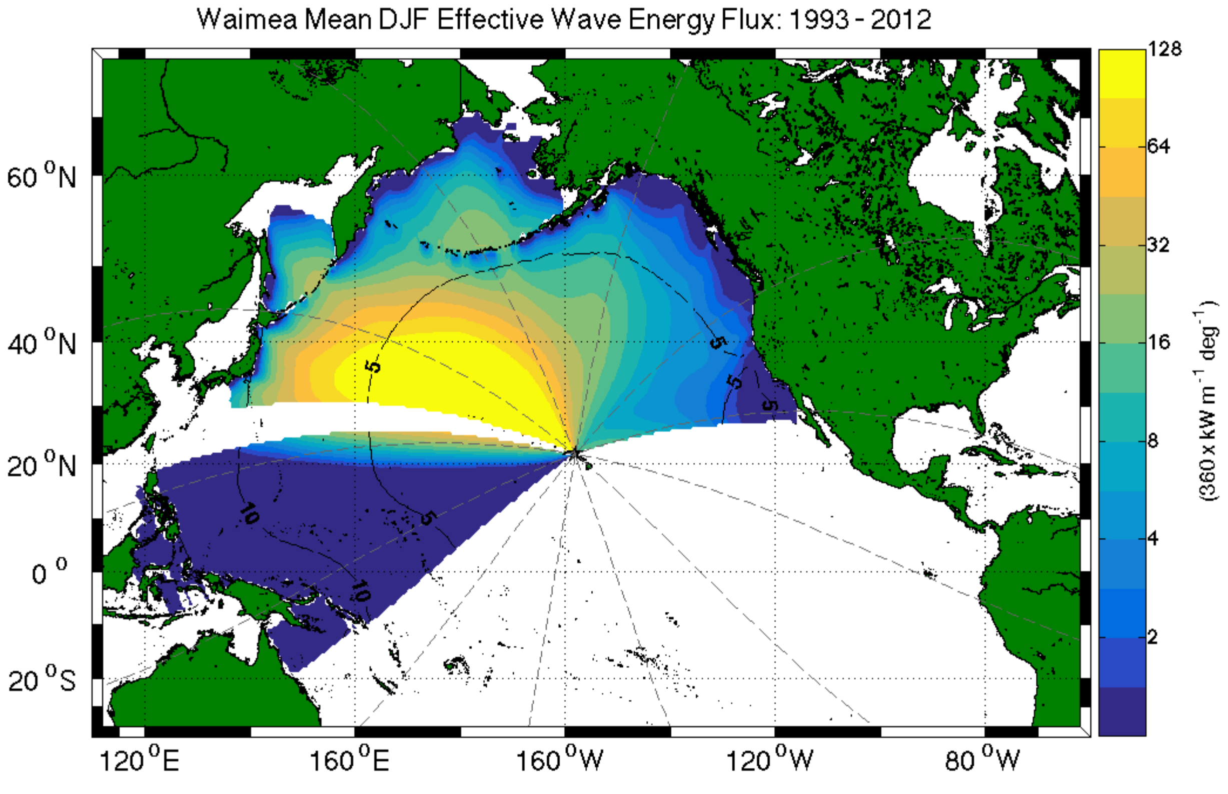

Figure 4.3: Waimea mean winter effective wave energy flux ESTELA model output.

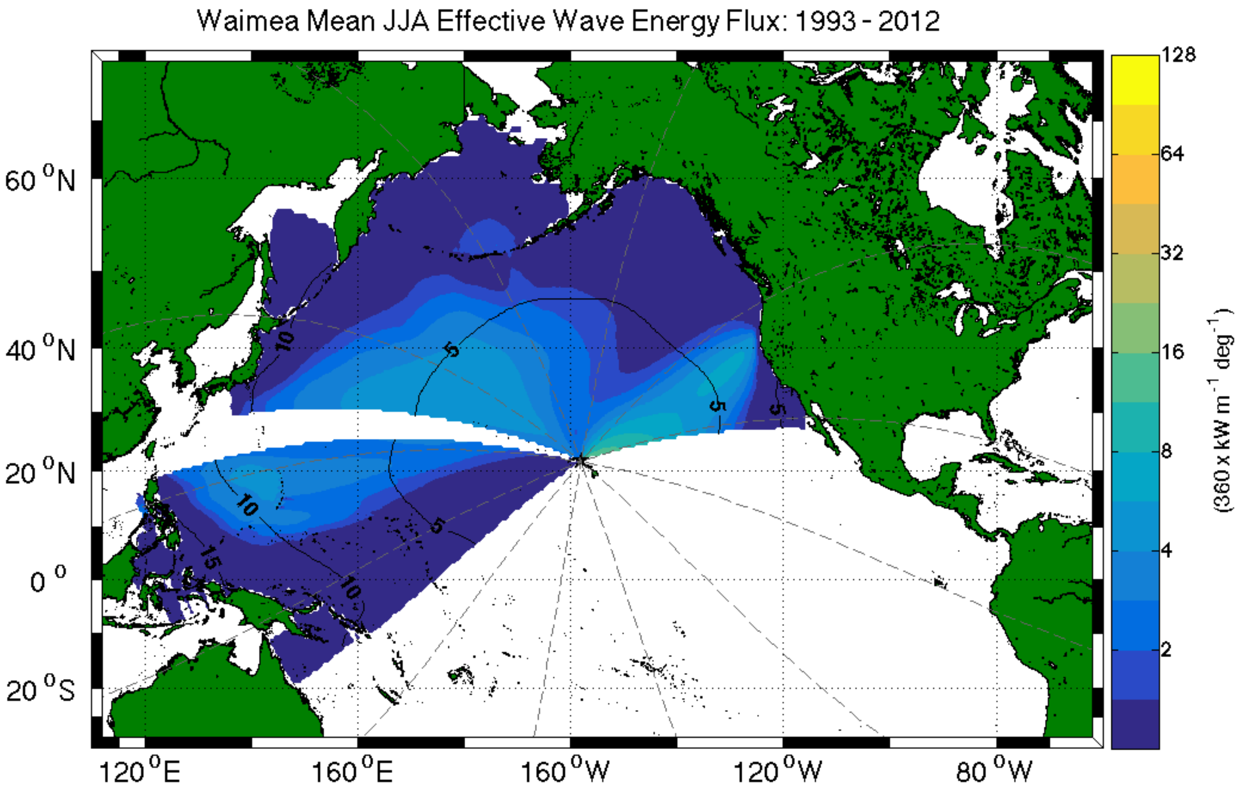

Figure 4.4: Waimea mean summer effective wave energy flux ESTELA model output.

4.2 ESTELA Source Fields and the North Pacific Index

Since we know that the winter time series of wave heights at Waimea have a high correlation to the NPI from Chapter 3, we plot the ESTELA model output during winters that have high (anomaly between -5 and -10, 1994, 2002, 2006, 2009, Figure 4.5) and low (anomaly < -10, 1998, 2001, 2003, 2010, Figure 4.6) NPI winter average values.

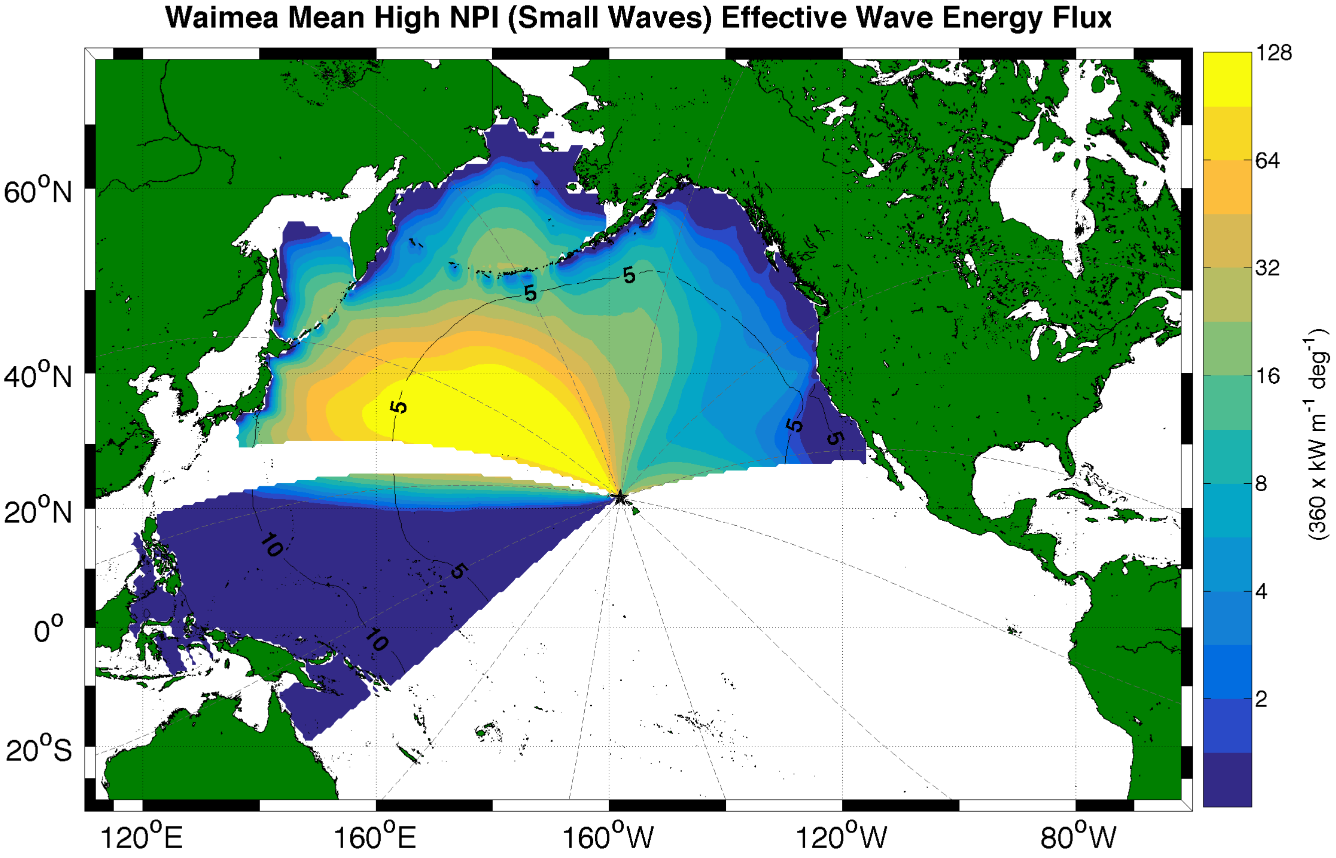

Figure 4.5: Waimea mean effective wave energy flux output from the ESTELA model during high NPI winters (DJF of 1994, 2002, 2006, and 2009).

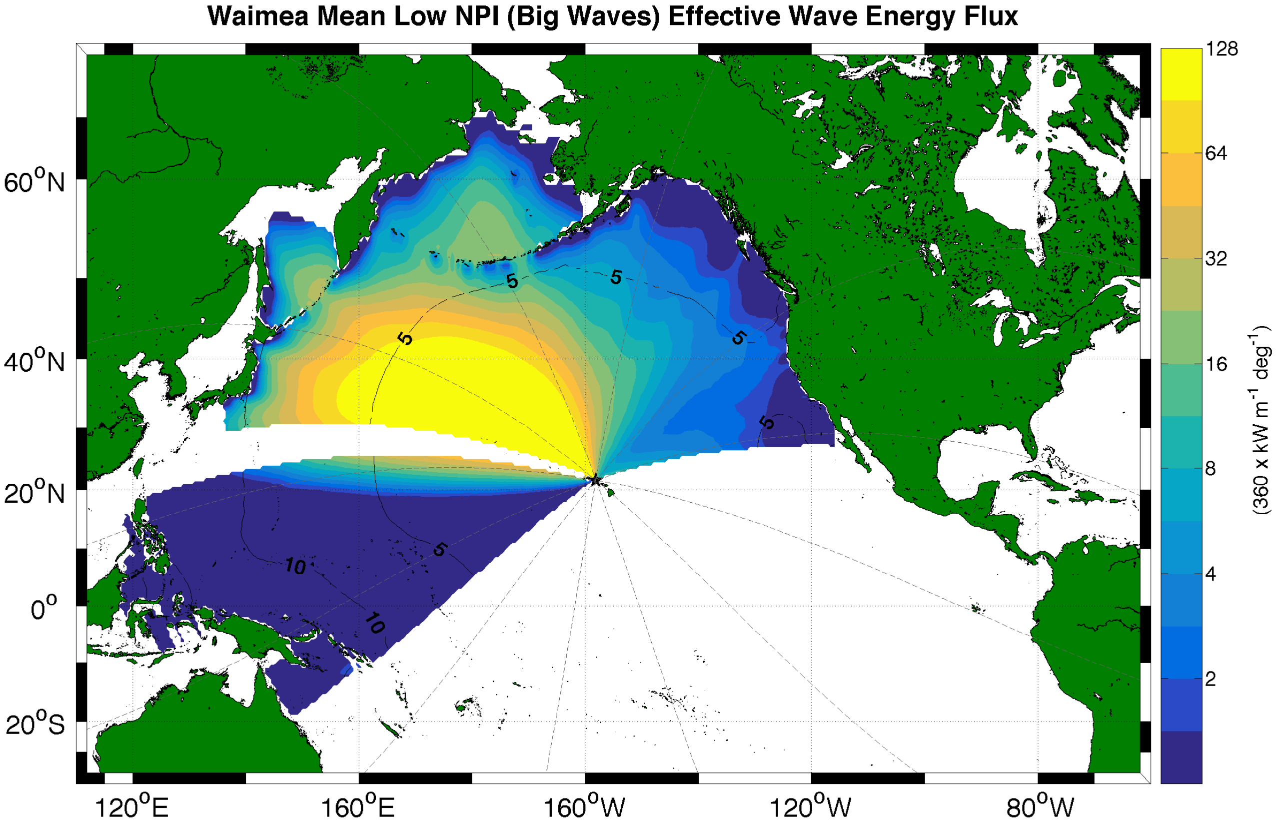

Figure 4.6: Waimea mean effective wave energy flux output from the ESTELA model during low NPI winters (DJF of 1998, 2001, 2003, and 2010).

We can see that during the low NPI years, when big waves arrive in the islands, that the energetic region covers a larger area, particularly more to the north. This could be related to the way that a deepened Aleutian Low alters the storm tracks that go through that region associated with the east asian jet stream.

To examine forcing fields in the "source box", I use CFSR model data for sea level pressure and for 10m winds sampled monthly. I average these fields over winter months during high (anomaly between -5 and -10) and low (anomaly $<$ -10) NPI winters (Figure 4.7). The box on these maps represents the generation region for the northwest swell waves (Figure 4.2). During low NPI conditions it appears that the gradient of sea level pressure in the source region for northwest swell waves is stronger, the surface winds are stronger and directed toward the Hawaiian Islands, and the deepened Aleutian low extends further southeast. This might cause storm tracks to also extend further southeast in the north Pacific. During high NPI winter, the Aleutian low is not as deep and winds are weak.

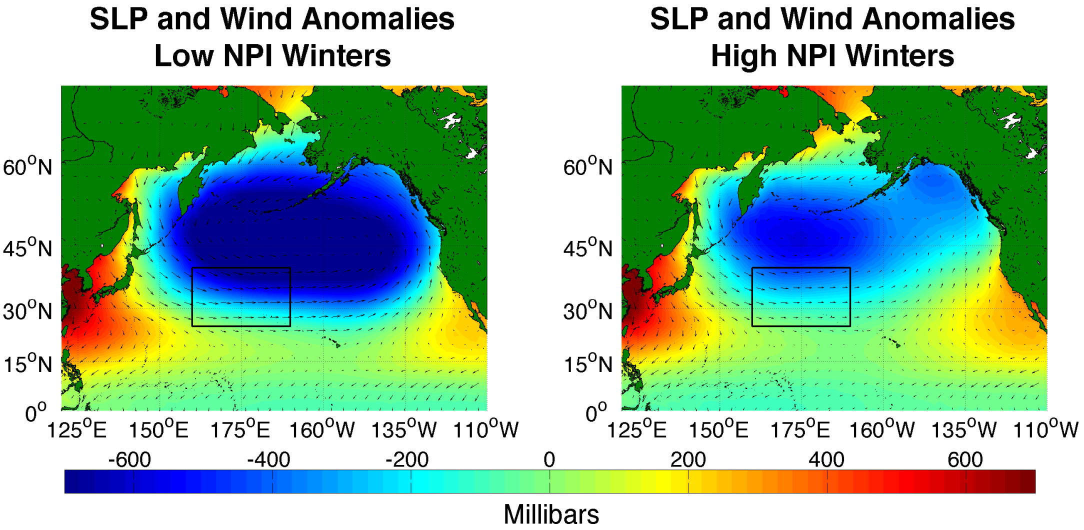

Figure 4.7: In color are sea level pressure anomalies. The arrows indicate the 10m wind speed anomalies. The black box outlines the primary source region for the northwest swell identified by the ESTELA model. The left map shows the conditions for the low NPI phase during winter (DJF) and on the right is for years where winter NPI is high.

Extratropical storm track data are publicly available from Serreze (2009). This dataset comprises a 50-year record of daily extratropical cyclone statistics computed for the northern hemisphere. Cyclone locations and characteristics were obtained by applying the updated Serreze et al. (1997) algorithm to daily Sea Level Pressure (SLP) data at six-hour intervals (Serreze and Barrett, 2008). The SLP source data are part of the National Centers for Environmental Prediction (NCEP) and National Center for Atmospheric Research (NCAR) Reanalysis data. The parameters included in this dataset are the position and central pressure of each cyclone, the distance the center of the cyclone traveled, whether the observation represents a cyclogenesis or cyclolysis event, and the local Laplacian of SLP and SLP tendency at each cyclone center. We examine how these storm tracks vary under conditions of low and high NPI to understand how changes in the atmospheric pressure cause changes in the path of storms in the source region for the northwest swell as determined by the ESTELA model and therefore cause variations seen in the northwest swell that arrives in the Hawaiian Islands.

In Figure 4.8 we see that storms under low NPI conditions tend to pass through the top third of the source region. The storm tracks that go into this figure all last two days or more, occur in the winter (December, January, or February), and have a cyclogenesis in the north Pacific. Storms that reform in the north Pacific are neglected if their cyclogenesis region was elsewhere. Under high NPI conditions, there are fewer storms that occur. Fewer of the storm tracks pass through the source region and onto the north Pacific High region.

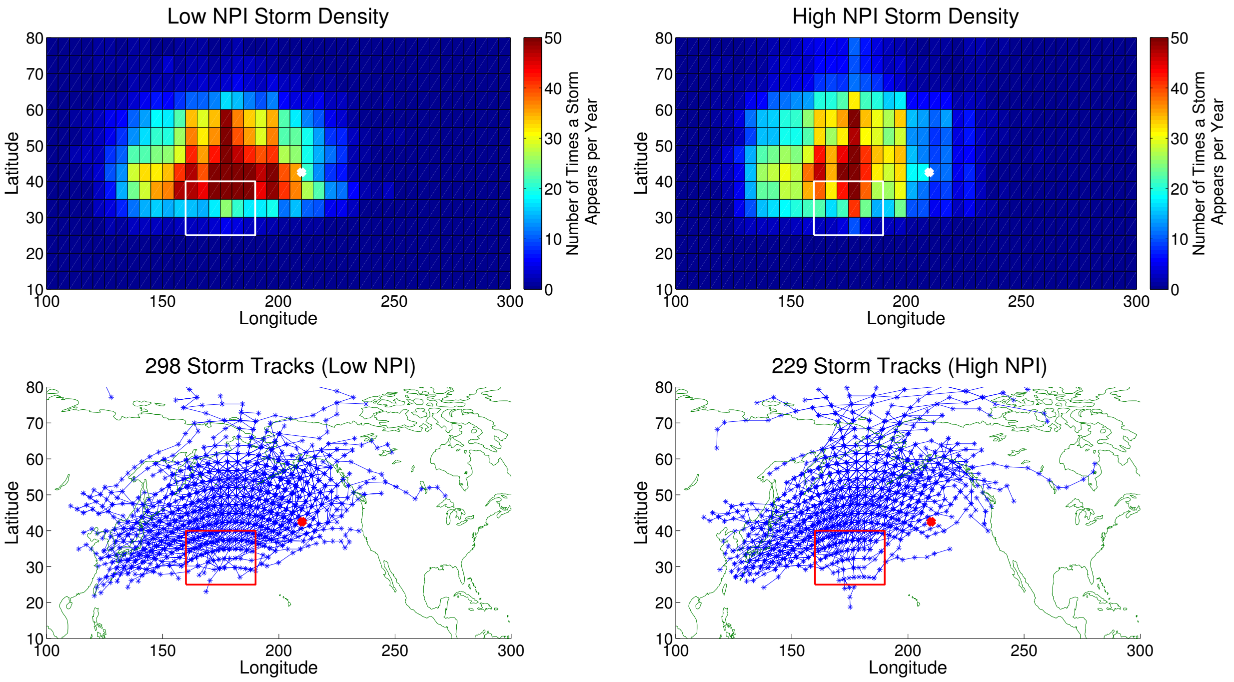

Figure 4.8: Top Left: Number of storms that pass through each latitude/longitude grid per winter year under low NPI conditions that result in a big northwest swell arriving in Hawai‘i. White dot indicated the position where sea level pressure has a -0.92 correlation to wave heights (Figure 3.11). Top Right: Number of storms that pass through each latitude/longitude grid per winter year under high NPI conditions. Bottom Left: Storm tracks that create the density plot above under low NPI conditions that result in a big northwest swell arriving in Hawai‘i. Red dot indicated the position where sea level pressure has a -0.92 correlation to wave heights. Bottom Right: Storm tracks that create the density plot above under high NPI conditions.

.

The ESTELA analysis illustrates the higher winter wave energy in the northwest

Pacific during low NPI conditions. This increase in energy is related to a stronger gradient in atmospheric pressure in the generation region and consequently more extratropical storms pass through the source region and continue eastward. During winters with high NPI conditions, the atmospheric pressure is not as low throughout the source region resulting in fewer extratropical storms (Figure 4.9). This agrees with (Barnard et al., 2017) that storms arrive further south along the west coast of the US when there is a deepening of the Aleutian Low (low NPI). That study was relating the storm tracks and wave activity to El Niño, but the NPI or PNA are better indicators of seasonal wave heights in the Hawai‘i region. ENSO, measured by SST anomalies in the eastern Pacific, is not the best measure of the atmospheric pressure cell in the northeast Pacific because they are not completely dependent on each other.

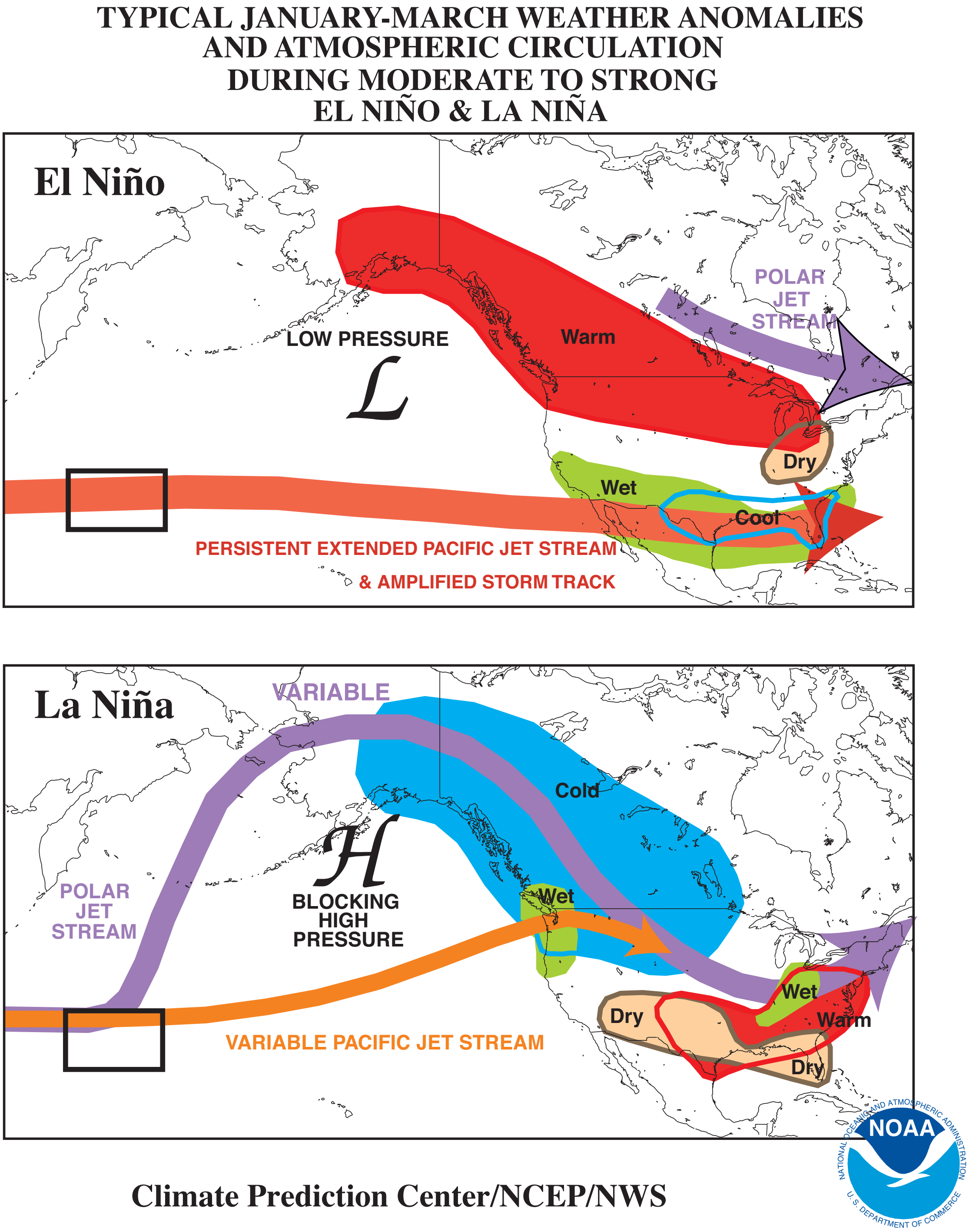

Figure 4.9: Top: Description of the east asian jet stream under El Niño conditions. Black box indicates the source region of the northwest swell identified by the ESTELA model. Bottom: Jet stream variability under La Niña conditions. Figure is from the NOAA Climate Prediction Center.

Atmospheric pressure in the Aleutian Low region appears to be a better indicator of seasonal swell conditions at Hawaiʻi than atmospheric variability in the source box itself. I examined winter mean winds in the direction of great circle routes leading to Hawaiʻi and winter averages of wind and atmospheric pressure variability over the source box. Neither yielded a higher correlation with Waimea swell than pressure in the Aleutian Low region. The best indicator of year-to-year variation in winter swell reaching Hawaiʻi appears to be downstream pressure to the northeast of the Islands. Downstream pressure appears to capture shifts in winter storm tracks that impact the Hawaiʻi region. Winter atmospheric pressure in this region tends to vary with ENSO, but not entirely. Hence, there are years when the NPI is low, Hawaiʻi swell is energetic, and El Nino is not active. Conversely, it does appear that all energetic El Nino years measured correspond to low NPI phases.

5 | Baldwin Beach Case Study

A majority of Hawaiian beaches have been reported to be in a state of long-term shoreward retreat (Fletcher et al., 2012), which poses considerable challenges for the state's tourism industry and threatens an iconic natural and cultural resource that provides 60 percent of the jobs in Hawaiʻi (Fletcher et al., 2003). On average, Hawaiʻi's shorelines are retreating at a long-term (since the early 1900s) rate of -0.11 ± 0.01 m/yr and at a short-term (post-World War II) rate of -0.06 ± 0.01 m/yr (Fletcher et al., 2012). Resource management and planning agencies seek to balance natural morphology of the coastal regions with human-resource needs (Hwang, 2005).

The causes for Hawaiian beach sediment loss are complex. Beach sand mining activities contributed to significant losses during the early to mid 20th century (Miller and Fletcher, 2003). At some locations, the addition of beach structures such as sea walls and revetments has had unintended negative impacts on sand supply. Other drivers of shoreline change include sediment availability, and varying littoral transports driven by waves, winds, and nearshore currents. In addition, climate change may play a role through rising sea levels and potentially shifting swell and sea wave conditions causing beaches that were previously stable to become unstable (Anderson et al., 2015; Fletcher et al., 2012; Garza et al., 2012). Sea level has risen around Hawaiʻi at approximately 1.5 mm/yr over the past century (Caccamise et al., 2005; Fletcher, 2010; Fletcher et al., 2012). Long-term sea level rise can lead to chronic coastal erosion, coastal flooding, drainage problems, salt-water intrusion, increased impact of short-term fluctuations in extreme tides causing episodic flooding and erosion (Fletcher, 2010). One important process influencing extreme sea level events in Hawai‘i is the occurrence of mesoscale eddies, which are large (>100 km) oceanic disturbances with sea level anomalies often exceeding 10 cm (Firing and Merrifield, 2004). Romine et al. (2013) showed that Hawai‘i sea level is rising most quickly at Maui (2.32 ± 0.53 mm/yr) in part due to differential land motion (Caccamise et al., 2005). Maui is also the island with the highest beach erosion rates (long-term rate of -0.17 ± 0.01 m/yr, short-term rate of -0.15 ± 0.01 m/yr, Fletcher et al. (2012)). If the impacts of climate change have been modest to this point, the future substantial rise in global sea level that is predicted in coming decades places Hawaiian beaches in significant jeopardy.

Beach restoration projects can provide short-term relief to chronic beach erosion problems, and nourishment efforts are becoming more prevalent in the United States (Campbell and Benedet, 2006). Unlike the continental United States, offshore sand deposits needed to supply nourishment projects in Hawai‘i are exceedingly limited. White sand beaches in Hawai‘i are composed of coralline and calcareous algae, coral, mollusk, and echinoderm fragments (Harney et al., 1999). Regulations on the quality and type of sand that can be used for nourishment substantially restrict sand supplies to local sources. The procedure of pumping offshore sands to the shore is quite costly. Beach nourishment often erodes faster than natural beach sand, and causes increased suspended sediment loads that can adversely affect nearshore reef environments (Jordan et al., 2010). In Hawai‘i, nourishment has not played a major role in the management of beach resources other than at Waikiki. The most common stabilization approach has been shoreline hardening in the form of seawalls. On the island of Oahu, Fletcher et al. (1997) found that about 24% of sandy beaches have narrowed or have been completely lost since 1949 as a result of artificial hardening of the shoreline. Nourishment has largely been restricted to locations where erosion poses an immediate threat to development including Stable Road and Sugar Cove on the north shore of Maui, Waikiki, and Lanikai on Oahu, as well as other isolated locations. To enhance the positive outcomes of these efforts and to improve their cost effectiveness, there is a need for design strategies that maximize the residence time of replacement sand on restored beaches.

Historical aerial photographs indicate that the highest rate of shoreline retreat among Oahu, Kauai, and Maui beaches has occurred at Baldwin Beach on the north shore of Maui, with a long-term erosion rate of -1.5 ± 1.1 m/yr and short-term rate of -2.2 ± 1.1 m/yr (Fletcher et al., 2012). Despite discontinuation of sand mining in 1979, ongoing erosion continues to be a concern, as evidenced by public restrooms at Baldwin falling into the ocean in 2011. The county of Maui has acquired 35 acres of land adjacent to Baldwin Beach (Figure 5.1), which has raised interest in beach restoration efforts for Baldwin. Recently, development on the beach that once may have negatively impacted the sediment budget has been removed, although these impacts have not been quantified. With the goal of restoring natural sediment transport behavior at the site, the removal of a revetment separating Baldwin Beach from Paia Beach has been proposed; however, the impact of this removal on the Baldwin Beach sediment budget is unknown. As a hot spot for shoreline erosion and a site where beach modifications have been proposed to alleviate the high erosion rate, Baldwin presents an intriguing case study for the examination of natural and human-induced drivers for shoreline change in the state of Hawai‘i.

Baldwin Beach is on the north shore of Maui and receives the northwest swell and trade wind swell (Figures A.5, B.4-B.6). The south swell does not impact on this beach because it is blocked by Maui Island. These swells act to move the sand along the beach back-and-forth from west to east seasonally. We use the long wave records we have created (Figures 3.8, A.9) to examine beach change at Baldwin.

Figure 5.1: Map of study site: Baldwin Beach, Maui with major features labeled.

A primary motivation for studying Baldwin Beach is the availability of monthly topographic surveys of the subaerial beach from April 2012 to April 2017 by Dr. Heidi Sherman of 'Ailana Surveying and Geomatics. The survey work has been conducted in consultation with Tara Owens, the UH Sea Grant College Program Coastal Processes and Hazards Specialist in the County of Maui Planning Department. These surveys use a RTK-GPS system to determine the height of the sand across the beach at points approximately 10m apart relative to a fixed reference point in the parking lot of Baldwin Beach. The surveys tell us how the subaerial volume of sediment is changing with time. This unique dataset allows for an assessment of the seasonal beach volume sediment cycle at Baldwin, as well as year-to-year changes.

Figure 5.2 shows the volume deviation from the mean alongshore Baldwin Beach with time. On the left side of the figure is the west side of Baldwin Beach by Baby Beach. On the right side, east, is where the beach changes the most seasonally. This is also the part of the beach that is most popular to beachgoers and where the public facilities are. Some of the major features that stand out are the erosion of the west side of the beach each winter and the accretion of the east side when that happens.

During the summer the reverse happens with erosion of the east side and accretion on the west side. This suggests that alongshore transport is the dominant mode at Baldwin. There appears to be a portion of the beach toward the middle that does not change very much throughout the year. The year with the most erosion at the spit since surveys started was winter 2016, and El Niño year with low NPI conditions.

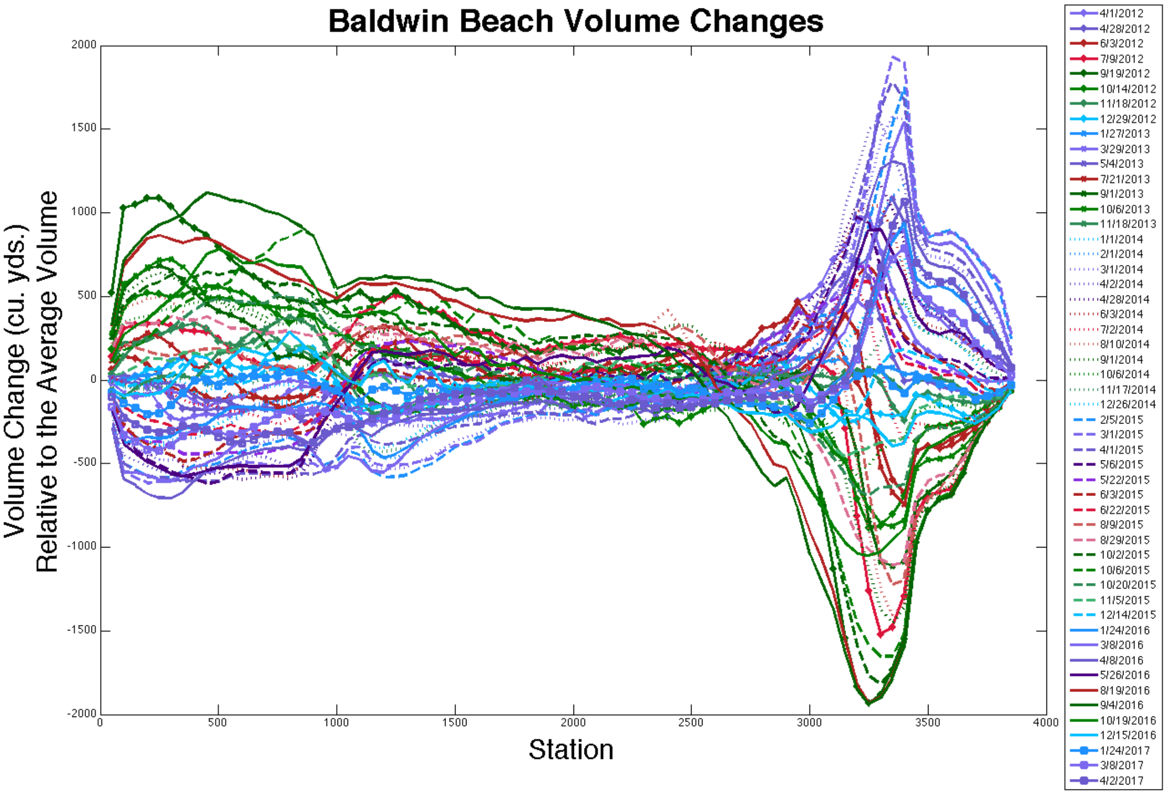

Figure 5.2: Baldwin Beach sand volume across the shoreline measured by ‘Ailana Surveying. Left side of the figure is near Baby Beach and the right side is the spit near the revetment. Each beach survey is indicated by a different line. Winter months are plotted in blue, spring is in purple, summer is red, and fall is green. Negative volume anomalies correspond with beach erosion.

The survey data represented as a Hovmöller plot shows us the propagation of sand across the beach with time. In Figure 5.3 the northwest swell is plotted on the left and the trade wind swell is on the right. In the middle is the deviation in beach volume across the beach with time increasing in the y-axis with blue representing accretion and red as erosion. The seasonal cycle is easy to see this way. The trade wind swell is persistent throughout the year, but often peaks in the fall. The south swell has a much smaller energy flux contribution to the system and stays below 5 kW/m year-round. The northwest swell is large during the winter and early spring at Baldwin with varying magnitude each year. In the winter of 2016 when the northwest swell is persistently large, the west side of the beach and in toward the middle erodes and the east side accretes. The following fall, the west side has the most accretion seen since surveys began and the east side has erosional conditions that persist corresponding with a large trade wind wave event. It is possible that the response of the beach after the large swell under low NPI conditions is as much or more important than what happened during the previous winter.

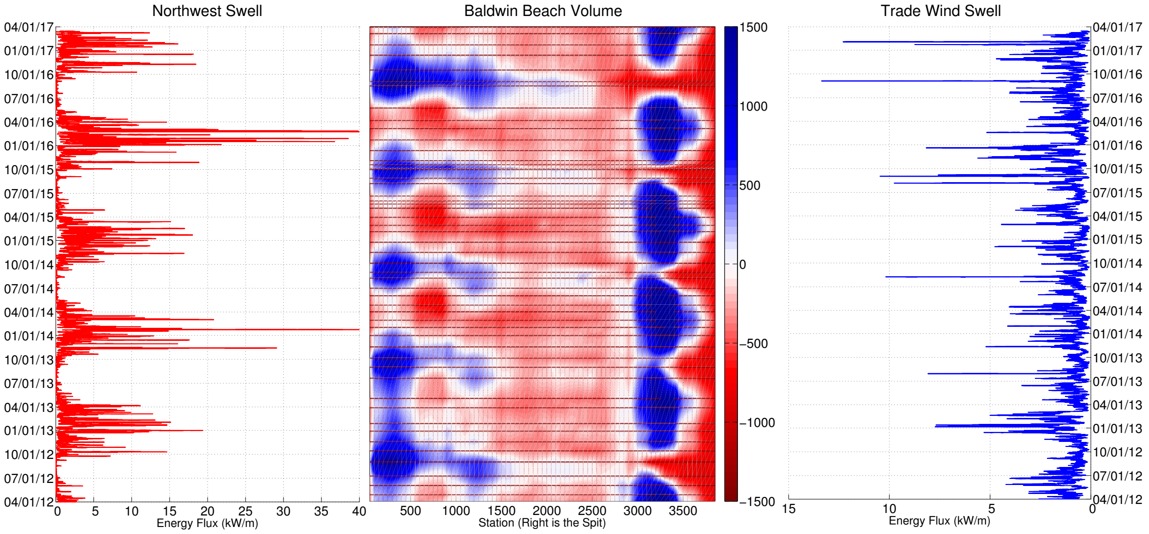

Figure 5.3: Left panel is the data from the Pauwela PacIOOS wave buoy. In red is a time series of incoming wave energy from the northwest swell. The middle panel is a hovmoller plot of the deviations from the mean volume at Baldwin Beach. Blue indicates accretion and red indicates erosion with the western side of the beach, by Baby Beach, on the left side and the eastern part, by the revetment, on the right side. The right panel is a time series of incoming wave energy from the trade wind swell in blue.

Similar seasonal longshore transport patterns have been documented at Kailua Beach, Oahu (Lee et al., 2004; Norcross et al., 2002), at Kaanapali Beach, Maui (D. and Fletcher, 2002; Vitousek et al., 2007), and at Waikiki Beach, Oahu (Miller and Fletcher, 2003). Seasonal and longer-term beach changes are the result of the cumulative impacts of wave events, which can significantly alter the subaerial sediment volume and shoreline position of island beaches in a single energetic event (Dail et al., 2000; Hanson et al., 2009). At Baldwin, the level of beach sand has been observed to change by several feet over the course of ten days during large winter swell 10/6/2014-10/16/2014 (Heidi Sherman, personal communication, 2014). Figures 5.4-5.5 show examples of the erosion that occurs at Baldwin Beach. While the longshore movement of sand is an energetic component of beach change at Baldwin, the role of cross-shore sediment transport is more subtle and challenging to assess.

Figure 5.4: Photos of Baldwin Beach taken August 6, 2015 and August 13, 2015.

Figure 5.5: Photos of Baldwin Beach taken September 9, 2014 and April 1, 2015 of the same stump in both photos.

At Baldwin, the net sand volume exhibits a seasonal cycle, although it is not clear if this represents and offshore-onshore seasonal cycle, or a convergence-divergence of longshore transport. Sea level, in addition to the wave activity, may attribute to beach erosion. When sea levels are high, waves can impact more of the beach sand and transport it. An examination of the temporal changes in sea level at Baldwin is beyond the scope of this current study, but could be related to seasonal heating, eddies, El Niño, and other wind-driven effects. Shown in Figure 5.6 is a comparison of net sea level before each beach survey and the beach volume. The sea level sign has been flipped in this figure to make the time series easier to compare. When sea levels are high, there is often more beach erosion. A spectral analysis of the Baldwin Beach volume time series reveals that the annual cycle is the dominant frequency of oscillation (Figure 5.7) supporting visual observations.

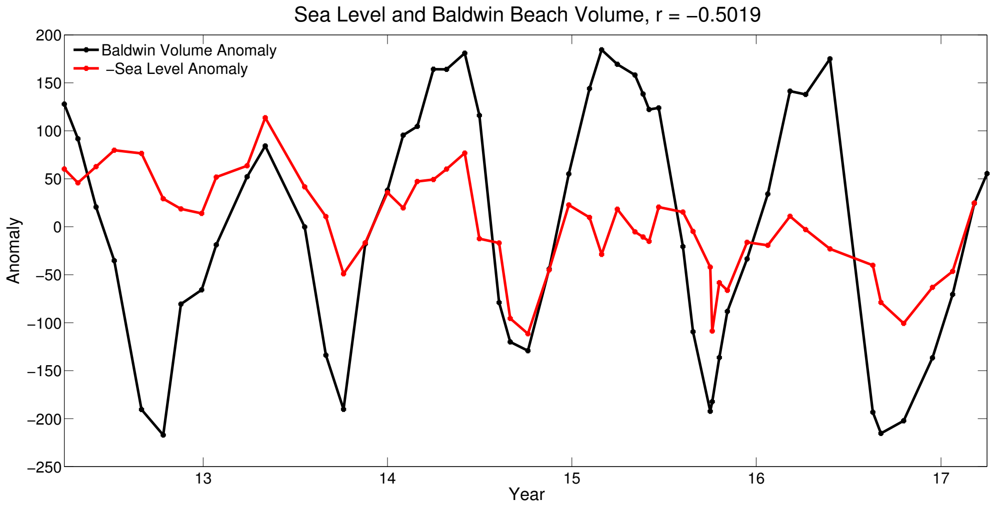

Figure 5.6: In black is the beach sand volume anomaly for Baldwin Beach Maui Island for each beach survey. In red is the net sea level anomaly between each survey with the sign flipped. The correlation between these two lines is -0.50, p = 0.032.

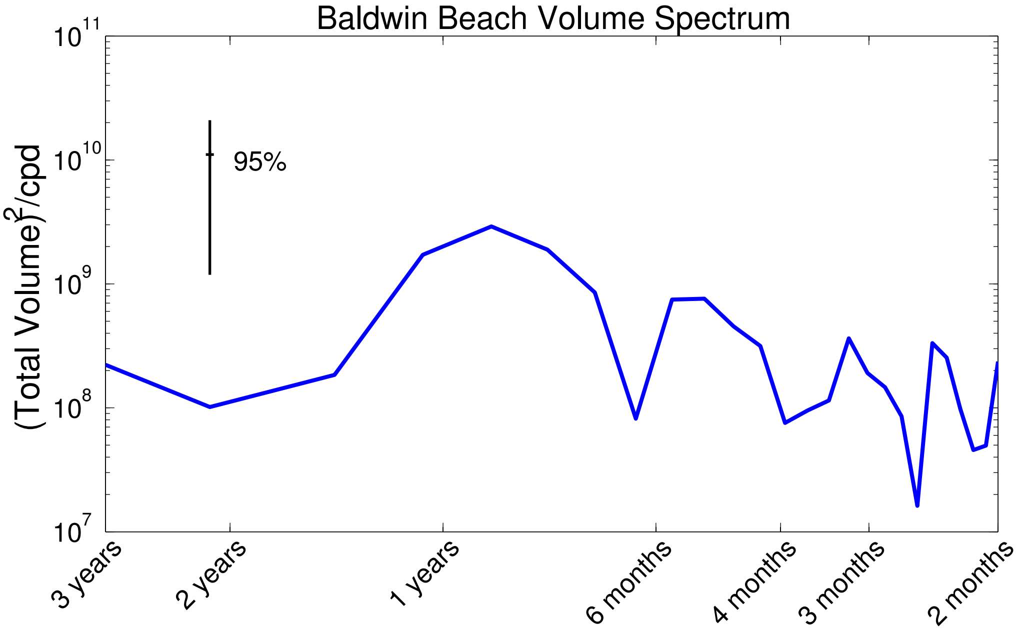

Figure 5.7: Spectral analysis of the Baldwin Beach net volume time series. Degrees of Freedom = 2.

Baldwin Beach historical shoreline information has been compiled by the Coastal Geology Group at the University of Hawai‘i. Historical shorelines were extracted from old aerial photographs. Figure 5.8 shows the progression of the shoreline since

1940. The shoreline retreat rate has been calculated at 4.2 mm/yr. This is the highest beach shoreline retreat rate in the state of Hawaiʻi for beaches examined by the Coastal Geology Group. A large contributor to why so much sand has been lost at this beach, is the old lime kiln factory described earlier. Now that it has been shut down, the retreat rate is likely not as fast as before.

An EOF of the Baldwin Beach profile information (with time mean removed) in space and time shows the first three modes explain 96.2% of the variance. Modes 1 and 2 describe the annual cycle of longshore sediment transport (Figure 5.9). Mode 3 describes a trending pattern in time, with a notable rhythmic pattern in the longshore. It might describe the growth of the beach along the middle and erosion occurring at the east and west ends.

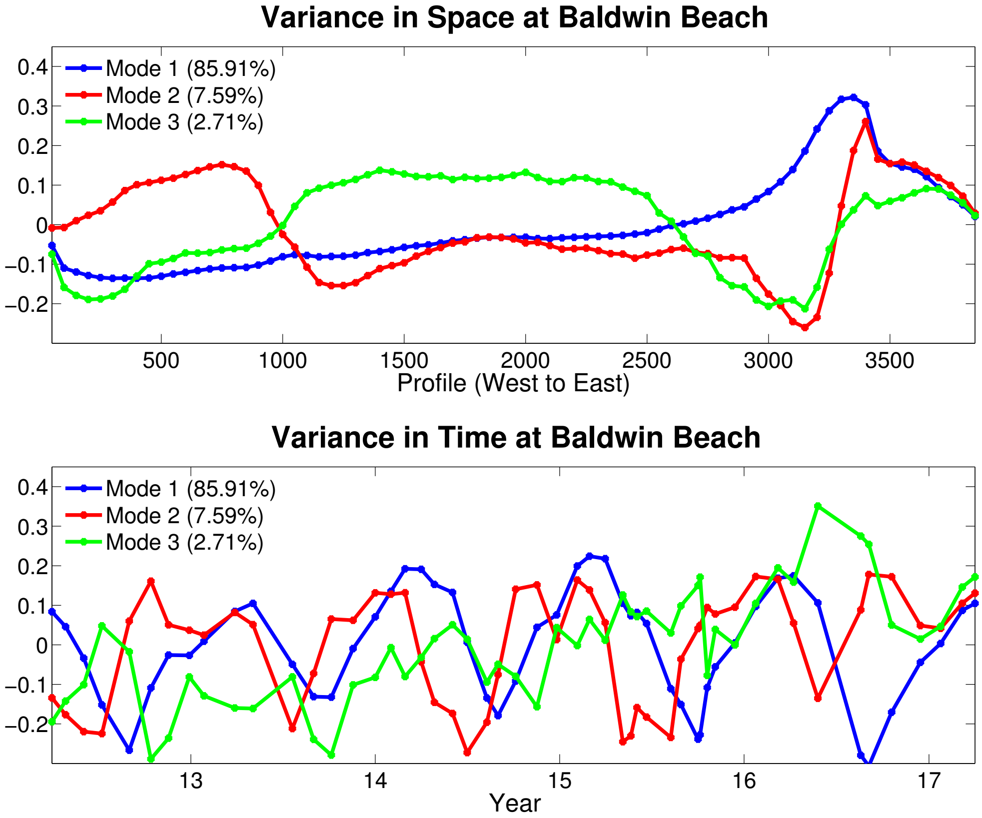

Figure 5.9: First three modes of the EOF of Baldwin Beach sand volume. Top: Variance of the modes in space across the beach with west on the left and east (spit) on the right. Bottom: Variance of the same modes in time. In the legend is the percent of the variance explained by each mode.

We examined the temporal variability of the 78 individual beach profiles to determine which parts of the beach respond to swell types. To do this we grouped profiles that exhibited similar variations over time using a cluster analysis (Thompson and Merrifield, 2014; Agustin et al., 2015). Shown is the resulting dendrogram from the analysis (Figure 5.10), which summarizes correlations amongst beach profiles. Based on the cluster analysis, we describe Baldwin in three sections: west (blue), middle (green), and the spit (red).

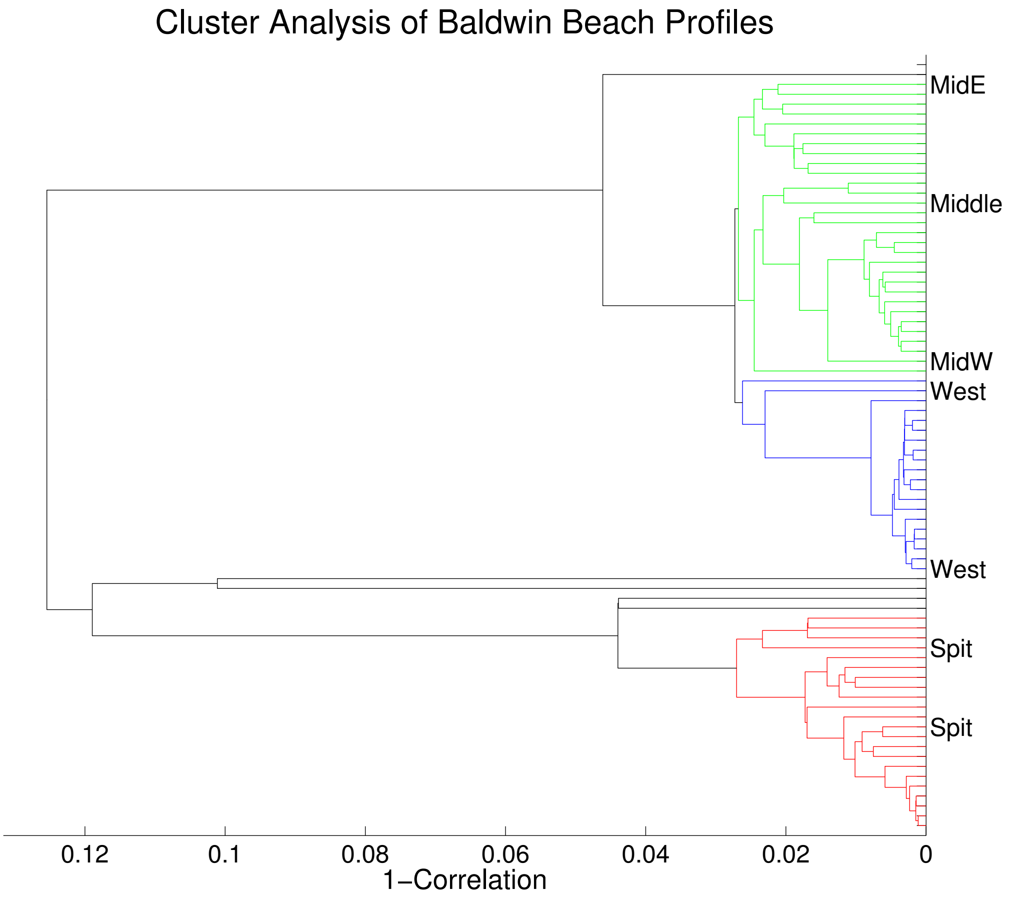

Figure 5.10: Cluster analysis dendrogram of Baldwin Beach volume data along the 78 profiles. The distance function used here is time series correlation values. In blue are profiles on the western side, in green are profiles in the middle, and in red are profiles that make up the spit on the wast end.

If we plot the time series of the average of each of these clusters, we get Figure 5.11. When the west end begins to erode, the middle starts to build up and then the spit on the east end builds up. The same occurs when the spit begins to erode and sand gets transported back to the western side. None of the clusters appear to have a trend. The spit time series looks similar to the mode one EOF time series (Figure 5.9).

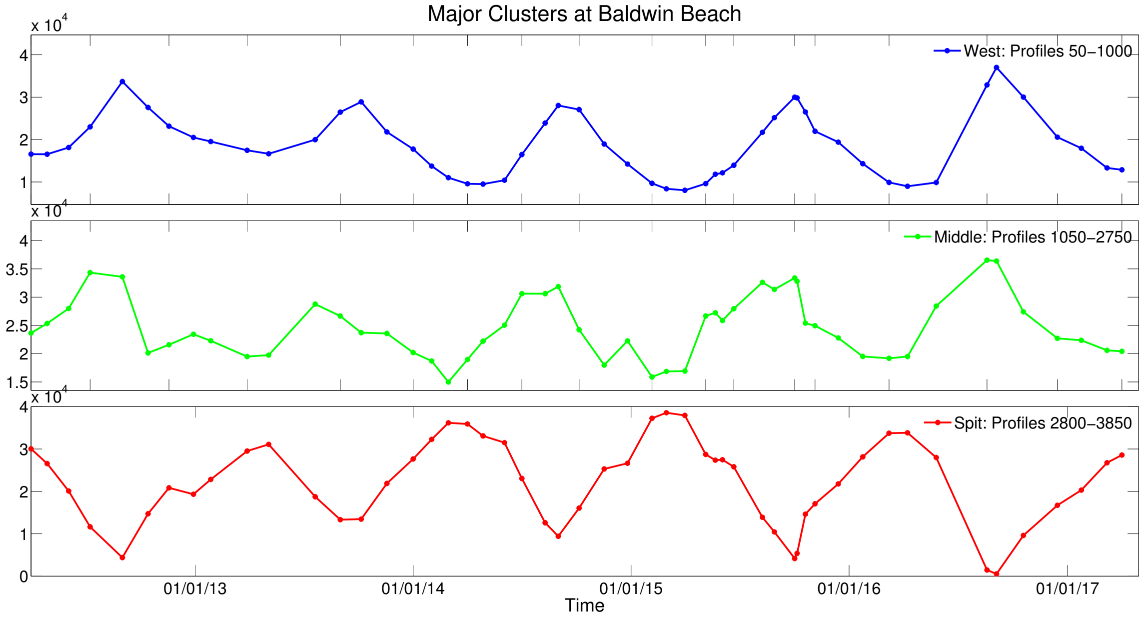

Figure 5.11: Time series of the three clusters identified in the cluster analysis. On top is the average of the western profiles in blue, in center are the middle profiles in green, and on bottom is the average of the profiles on the east end in red.

A complete study of Baldwin Beach would require further information about the cross-shore characteristics of the sediment transport and in-situ measurements of the currents. With the information that is available, it appears that Baldwin Beach exhibits dominant seasonal variation. Given the shortness of the time series, it is not clear if the beach exhibits long-term erosion of interannual variation. A combination of northwest swell, western trade wind swell, and perhaps sea level cause beach volume changes. The changes in net volume (Figure 5.6) require further study. It is unclear if some of the sand gets stored offshore or for how long.

For the time period we have volume data for Baldwin Beach, it appears that the impact of NPI on swell intensity also impacts the volume of sediment transport (Figure 5.3). During the large winter northwest swell, there was not unusual net beach erosion. The recovery the following summer is what makes the low NPI year unique with more accretion on the western and middle parts than normal and increased erosion on the eastern side (Figure 5.11). There was also a large trade wind wave event during the recovery phase. The response of the beach might also be related to an equilibrium between not only the incoming swell energy, but also the incoming angle. There may also be significant exchange between the subaerial beach and the nearshore that is not captured in this volume data and requires further study.

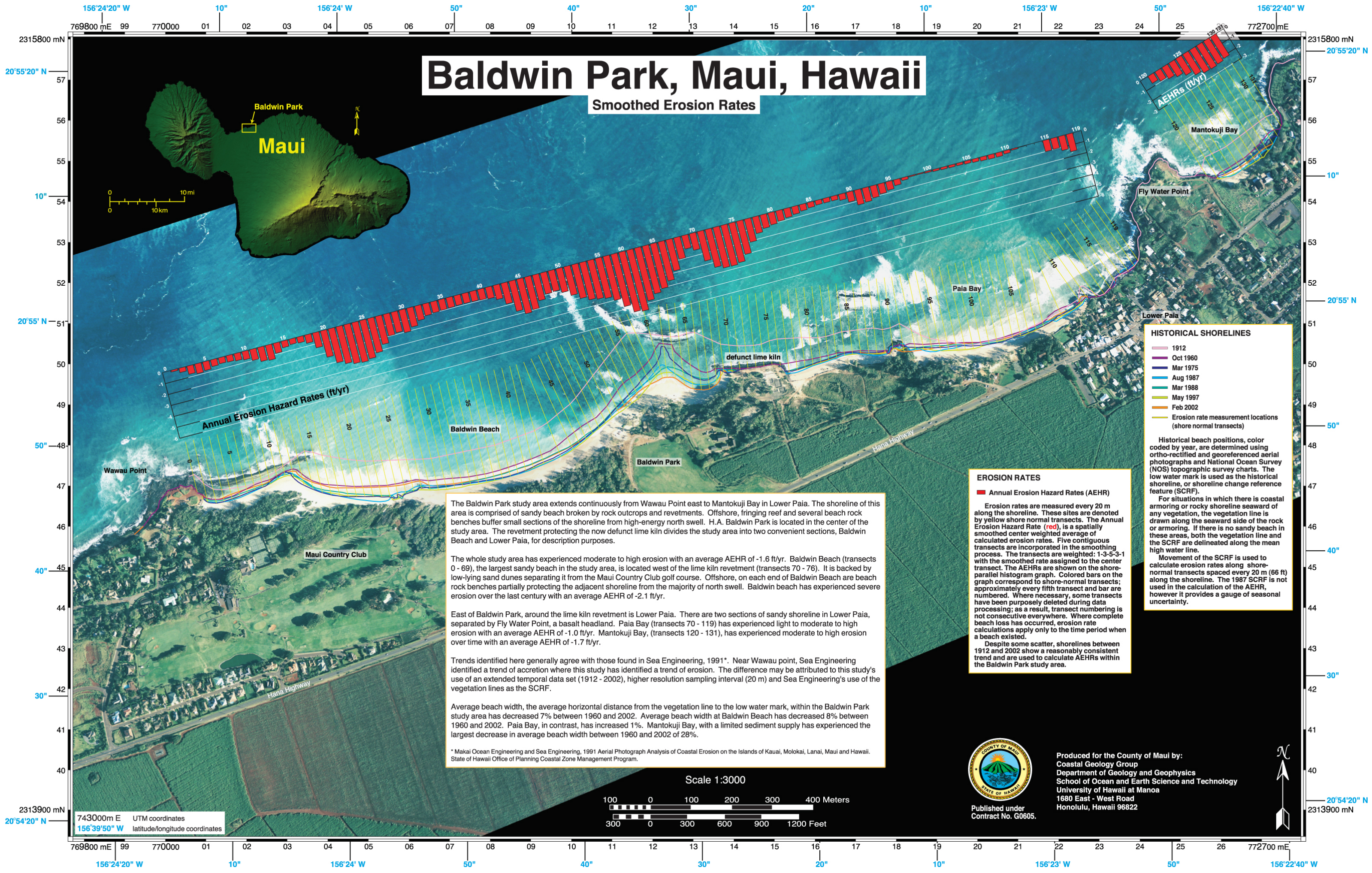

The Baldwin Park study area extends continuously from Wawau Point east to Mantokuji Bay in Lower Paia. The shoreline of this area is comprised of sandy beach broken by rock outcrops and revetments. Offshore, fringing reef and several beach rock benches buffer small sections of the shoreline from high-energy north swell. H.A. Baldwin Park is located in the center of the study area. The revetment protecting the now defunct lime kiln divides the study area into two convenient sections, Baldwin Beach and Lower Paia, for description purposes.

The whole study area has experienced moderate to high erosion with an average AEHR of -1.6 ft/yr. Baldwin Beach (transects 0 - 69), the largest sandy beach in the study area, is located west of the lime kiln revetment (transects 70 - 76). It is backed by low-lying sand dunes separating it from the Maui Country Club golf course. Offshore, on each end of Baldwin Beach are beach rock benches partially protecting the adjacent shoreline from the majority of north swell. Baldwin beach has experienced severe erosion over the last century with an average AEHR of -2.1 ft/yr.

East of Baldwin Park, around the lime kiln revetment is Lower Paia. There are two sections of sandy shoreline in Lower Paia, separated by Fly Water Point, a basalt headland. Paia Bay (transects 70 - 119) has experienced light to moderate to high erosion with an average AEHR of -1.0 ft/yr. Mantokuji Bay, (transects 120 - 131), has experienced moderate to high erosion over time with an average AEHR of -1.7 ft/yr.

Trends identified here generally agree with those found in Sea Engineering, 1991*. Near Wawau point, Sea Engineering identified a trend of accretion where this study has identified a trend of erosion. The difference may be attributed to this study's use of an extended temporal data set (1912 - 2002), higher resolution sampling interval (20 m) and Sea Engineering's use of the vegetation lines as the SCRF.

Average beach width, the average horizontal distance from the vegetation line to the low water mark, within the Baldwin Park study area has decreased 7% between 1960 and 2002. Average beach width at Baldwin Beach has decreased 8% between 1960 and 2002. Paia Bay, in contrast, has increased 1%. Mantokuji Bay, with a limited sediment supply has experienced the largest decrease in average beach width between 1960 and 2002 of 28%.

* Makai Ocean Engineering and Sea Engineering, 1991 Aerial Photograph Analysis of Coastal Erosion on the Islands of Kauai, Molokai, Lanai, Maui and Hawaii. State of Hawaii Office of Planning Coastal Zone Management Program.

Erosion rates are measured every 20 m along the shoreline. These sites are denoted by yellow shore normal transects. The Annual Erosion Hazard Rate (red), is a spatially smoothed center weighted average of calculated erosion rates. Five contiguous transects are incorporated in the smoothing process. The transects are weighted: 1-3-5-3-1 with the smoothed rate assigned to the center transect. The AEHRs are shown on the shore-parallel histogram graph. Colored bars on the graph correspond to shore-normal transects; approximately every fifth transect and bar are numbered. Where necessary, some transects have been purposely deleted during data processing; as a result, transect numbering is not consecutive everywhere. Where complete beach loss has occurred, erosion rate calculations apply only to the time period when a beach existed.

Despite some scatter, shorelines between 1912 and 2002 show a reasonably consistent trend and are used to calculate AEHRs within the Baldwin Park study area.

Historical beach positions, color coded by year, are determined using ortho-rectified and georeferenced aerial photographs and National Ocean Survey (NOS) topographic survey charts. The low water mark is used as the historical shoreline, or shoreline change reference feature (SCRF).

For situations in which there is coastal armoring or rocky shoreline seaward of any vegetation, the vegetation line is drawn along the seaward side of the rock or armoring. If there is no sandy beach in these areas, both the vegetation line and the SCRF are delineated along the mean high water line.

Movement of the SCRF is used to calculate erosion rates along shore-normal transects spaced every 20 m (66 ft) along the shoreline. The 1987 SCRF is not used in the calculation of the AEHR, however it provides a gauge of seasonal uncertainty.

Published under
Contract No. G0605.

Produced for the County of Maui by:
Coastal Geology Group
Department of Geology and Geophysics
School of Ocean and Earth Science and Technology
University of Hawaii at Manoa
1680 East - West Road
Honolulu, Hawaii 96822

Figure 5.8: Map of the smoothed erosion rated at Baldwin Beach, Maui Island, Hawaii for 1912-2002. Figure obtained from http://www.soest.hawaii.edu/coasts/erosion/index.php

6 | Summary and Conclusion

Understanding the wave climate of Hawai‘i is essential for oceanographers, coastal engineers, and coastal planners who make decisions and inferences based upon the expected wave climate. The influence of Pacific climate variability on the winter wave field at Hawai‘i is closely related to the North Pacific Index and sea level pressure.

This study found that wave buoy data are best once directional buoy data becomes available in 2000 to describe swell types. The Goddard and Caldwell dataset agrees with the directional buoy data during the overlap period, as well as with SWAN model hindcasts. The visual-based observations appear to be a more reliable estimate of winter wave heights at Waimea than the nondirectional buoys. The winter northwest swell has a high correlation to the North Pacific Index, a proxy for sea level pressure and a -0.92 correlation with the winter sea level pressure at 42.5°N, 150°W.

Yin (2005) found that with global warming, there will be an intensification poleward of the Aleutian Low. This will cause storm tracks to also shift northwards (Salathè, 2006). More northward storm tracks might mean a reduction in the northwest swell energy reaching Hawai‘i. The ESTELA model shows the region 25-40°N, 160-190°W to be the primary source of the northwest swell energy. Storm tracks in that region are more frequent and the jet stream is intensified during low NPI conditions creating bigger winter waves in the Hawaiian Islands.

Baldwin Beach of Maui Island, Hawai‘i experiences cross-shore sediment transport back and forth each year with the onset of the northwest swell and the east trade wind swell. High sea levels may promote erosion at Baldwin Beach. Large wave events contribute further to extreme water levels. The ESTELA model gives insight into which swell types will impact different island areas like Baldwin Beach on Maui Island.

To understand the variability of the trade wind swell and south swell better, we recommend an expansion of this work by using our extended time series for each swell type and comparing these swells to different forcings as we have done for the winter northwest swell. An examination of the currents and offshore sediment supply at Baldwin Beach would greatly contribute to the understanding of the dynamics there.

A Appendix A

In Chapter 3, Wave Buoys, we discussed how we created directional spectrums for each of the wave buoys and used that to stitch together the available buoy data and observations to make long time series for the northwest swell. In this Appendix we do the same for the south swell and for the east trade wind swell.

A.1 Directional Spectrums

Using data provided by PacIOOS, we first construct directional spectrums for each of the wave buoys to see which swell types are dominant at each buoy. Figure 2.1 shows the locations of the buoys described below.

For Hanalei, the dominant source of wave energy in the summer (June, July, August) is the trade wind swell and during the winter (December, January, February) the northwest swell dominates (Figure A.1). The northwest swell at this buoy is approximately in the range of 250-10°, and 6-30sec. The east trade wind swell is approximately 50-100° and 5-13s.

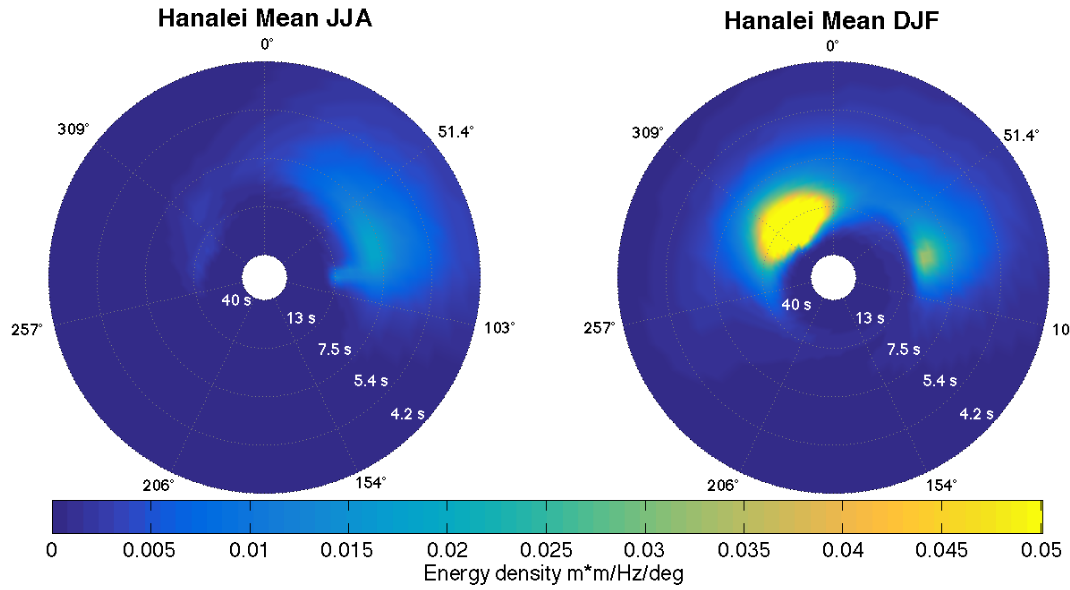

Figure A.1: Hanalei directional spectrum. Left: Summer (June, July, August) Average. Right: Winter (December, January, February) Average.

During the summer at Barbers Point, the dominant source of wave energy is the south swell from approximately 105-230° over 4-25sec (Figure A.2). During the winter, energy mostly comes from the northwest (260-340°, 8-20sec). There is also a south swell signal in the winter in the directional spectrum (110-170°, 4-10sec).

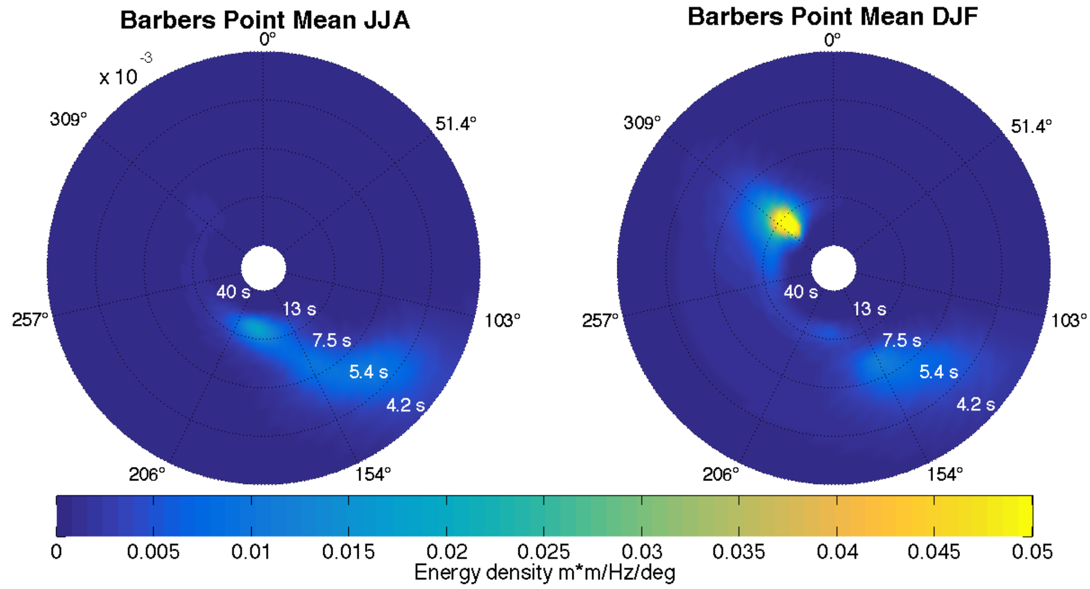

Figure A.2: Barbers Point directional spectrum. Left: Summer (June, July, August) Average. Right: Winter (December, January, February) Average.

Summers at Kaneohe Bay have a dominant source of wave energy is the trade wind swell from approximately 0-100° over 5-13sec (Figure A.3). During the winter there an energy signal coming from the northwest (315-15°, 6-20sec) and from the east (20-100°, 4-13sec). The northwest swell appears more north in this directional spectrum because waves have to wrap around the north side of Oahu first and then travel southeast to reach Kaneohe Bay.

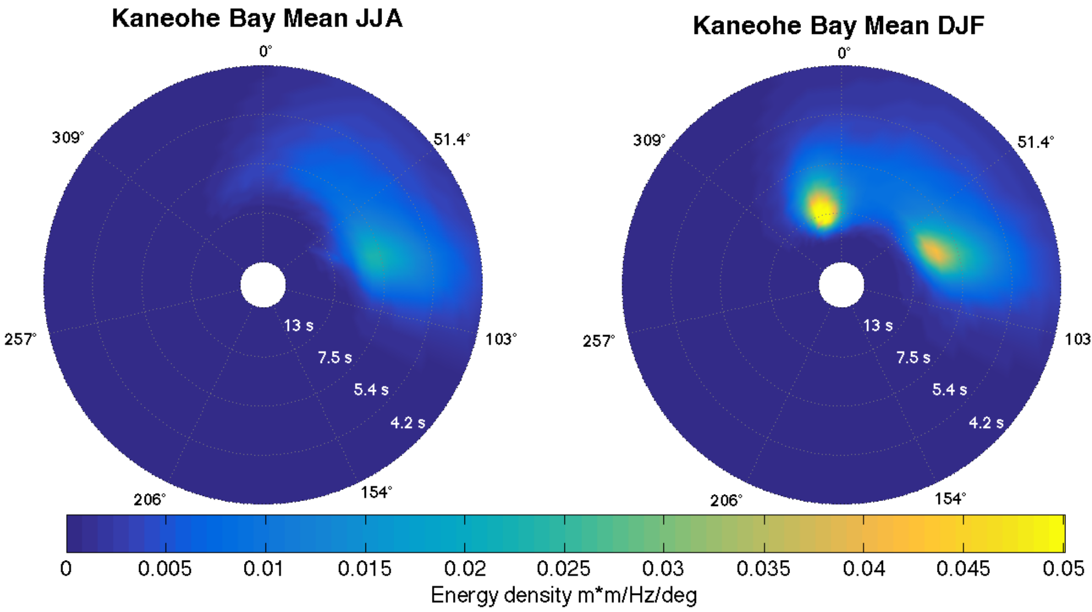

Figure A.3: Kaneohe Bay directional spectrum. Left: Summer (June, July, August) Average. Right: Winter (December, January, February) Average.

The Mokapu Point buoy has a dominant source of wave energy is a broad trade wind swell from approximately 0-130° over 4-13sec during the summer (Figure A.4). During the winter there is more energy coming from the northwest (315-15°, 6-30sec) and from the east (20-130°, 7-10sec). Again, the northwest swell appears more north in this directional spectrum compared to Figure 3.1 because the energy has to wrap around the island.

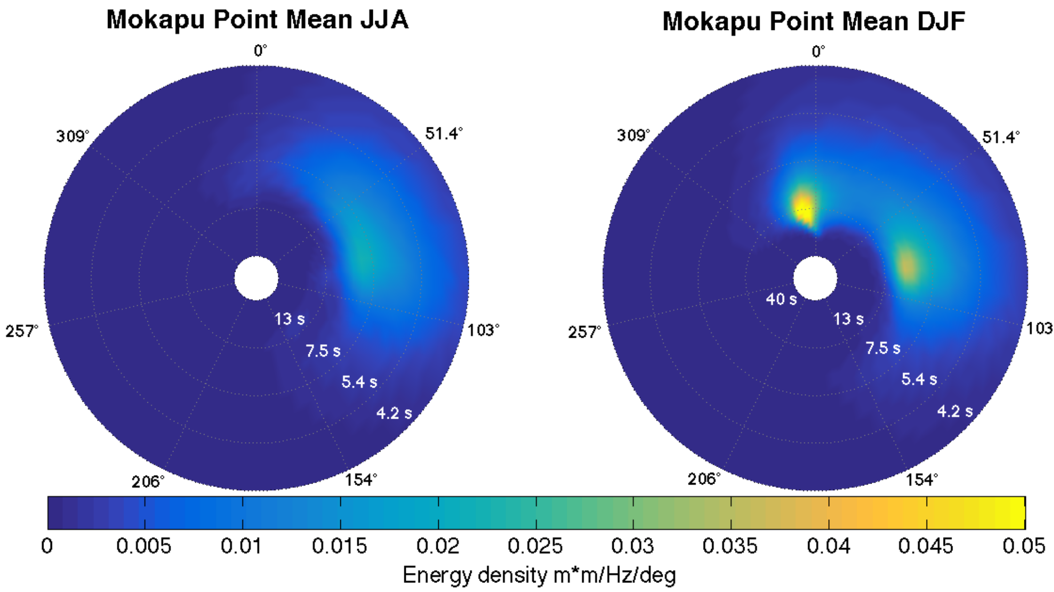
Mokapu Point Mean JJA

Mokapu Point Mean DJF

Figure A.4: Mokapu Point directional spectrum. Left: Summer (June, July, August) Average. Right: Winter (December, January, February) Average.

During the summer at Pauwela, the dominant source of wave energy is the trade wind swell from approximately 0-125° over 4-15sec (Figure A.5). During the winter there is energy coming from the northwest (260-5°, 7-30sec) and from the east (30-125°, 4-15sec).

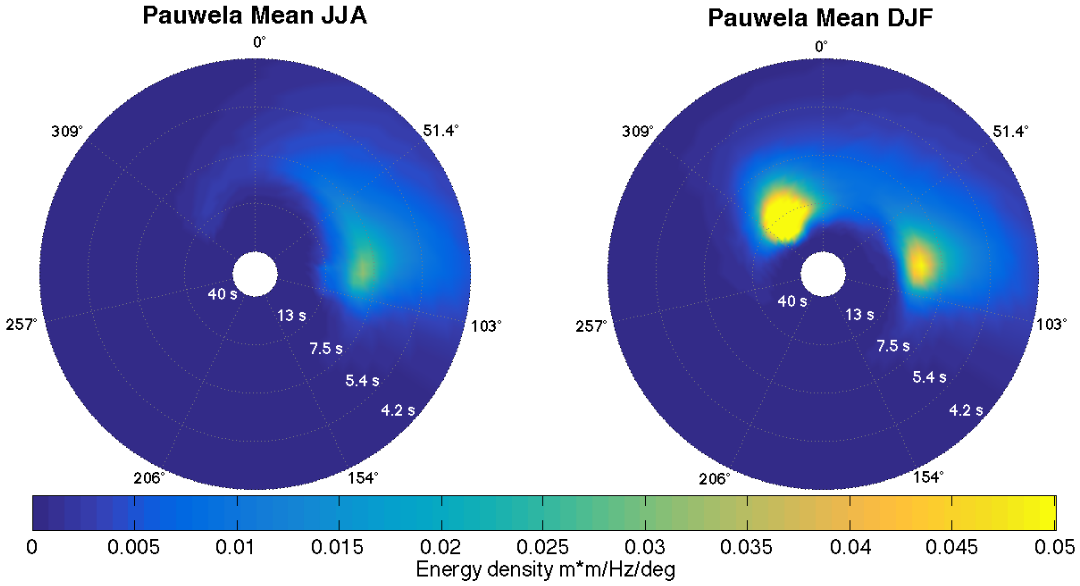
Pauwela Mean JJA

Pauwela Mean DJF

Figure A.5: Pauwela directional spectrum. Left: Summer (June, July, August) Average. Right: Winter (December, January, February) Average.

Summers at Kaumalapau have a dominant source of wave energy is the south swell from approximately 155-210° over 4-25sec (Figure A.6). During the winter, energy comes from the west (250-310°, 8-20sec). This is likely the northwest swell wrapping around the islands to Kaumalapau. There is also a south swell signal in the winter in the directional spectrum (155-175°, 5-10sec).

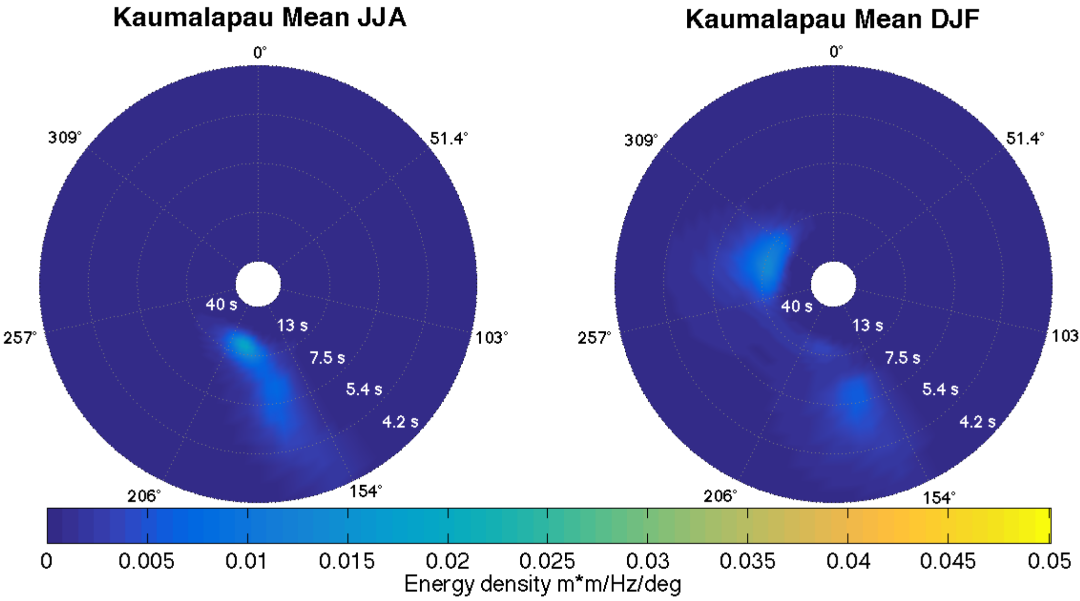

Figure A.6: Kaumalapau directional spectrum. Left: Summer (June, July, August) Average. Right: Winter (December, January, February) Average.

The Hilo has a dominant source of wave energy is the trade wind swell from approximately 0-155° over 5-15sec during the summer (Figure A.7). During the winter there is energy coming from the northwest (300-5°, 7-30sec) and from the east (5-150°, 5-13sec).

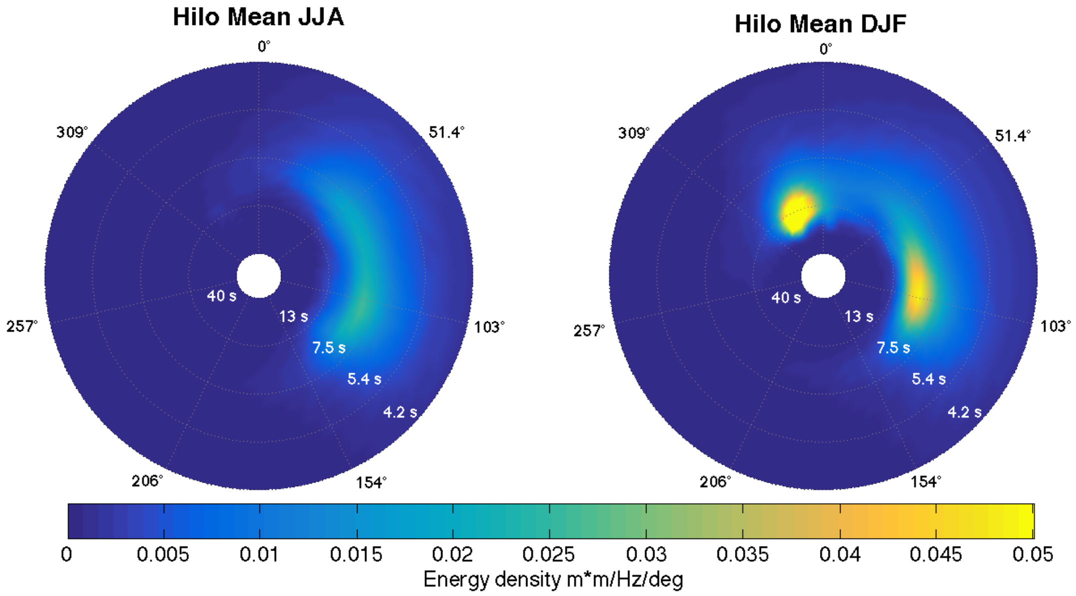

Figure A.7: Hilo directional spectrum. Left: Summer (June, July, August) Average. Right: Winter (December, January, February) Average.

A.2 South and Trade Wind Swell Climatologies

Figure A.8 shows time series of the significant wave height from buoys that experience an eastern trade swell. From this figure, it appears that Mokapu Point and Pauwela get the most energy. Hilo and Kaneohe Bay also get a good signal. We combine these records to create one long time series for the trade wind swell in Figure A.9.

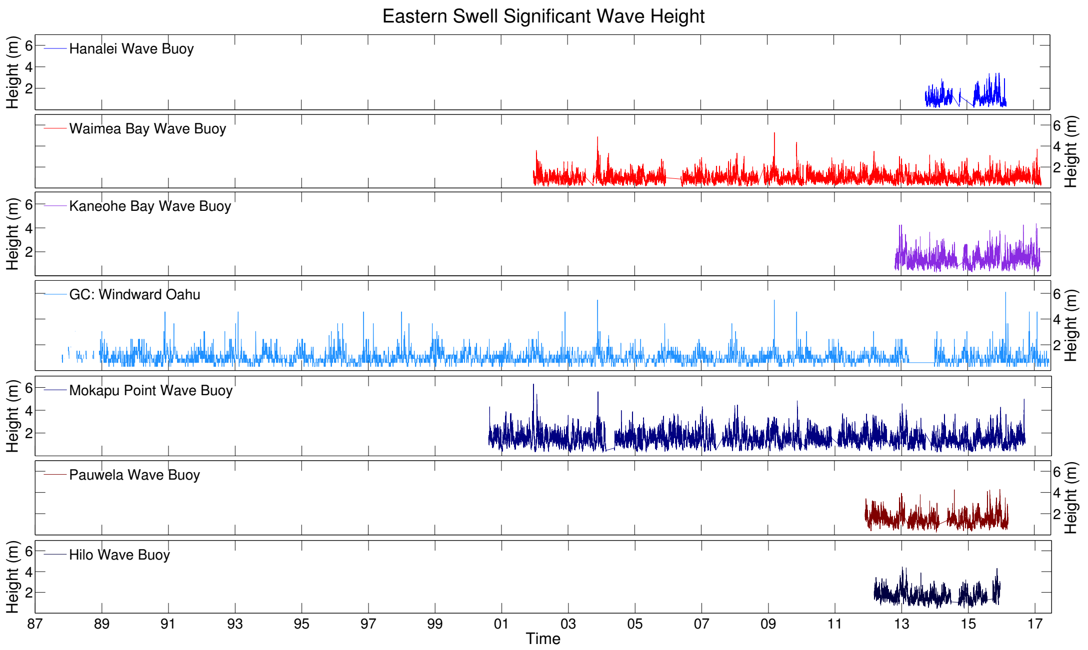

Figure A.8: Significant wave heights for the eastern trade wind swell. GC is the Goddard and Caldwell dataset.

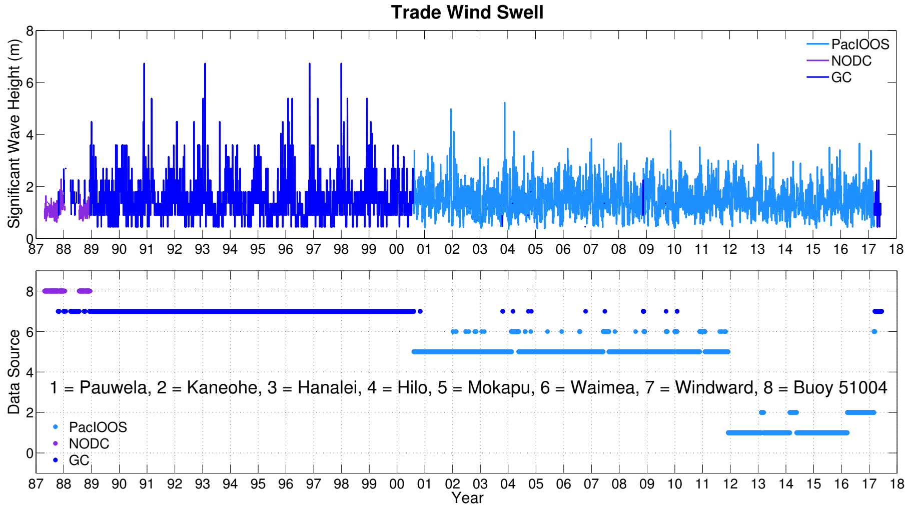

Figure A.9: Long time series for the trade wind swell created by merging the time series from the PacIOOS buoys and the Goddard and Caldwell surf height observations.

Figures A.10 shows time series of the significant wave height from buoys that experience an Southern swell. There are only two buoys currently run by PacIOOS that capture a good south swell signal at the time of this study for a shorter period of time than any of the other swell directions. We combine these records to create one long time series for the South swell in Figure A.11.

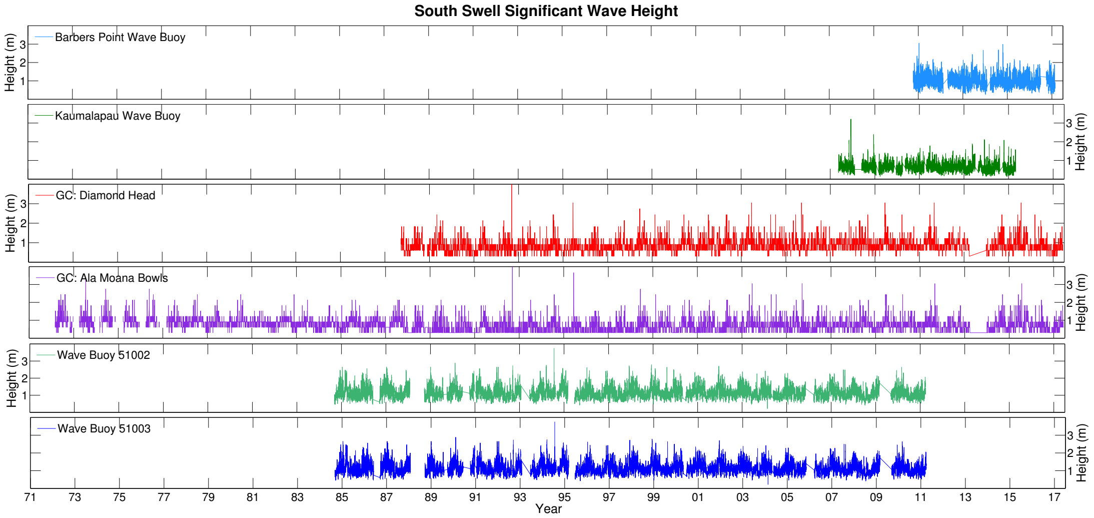

Figure A.10: Significant wave heights for the South swell. GC is the Goddard and Caldwell dataset.

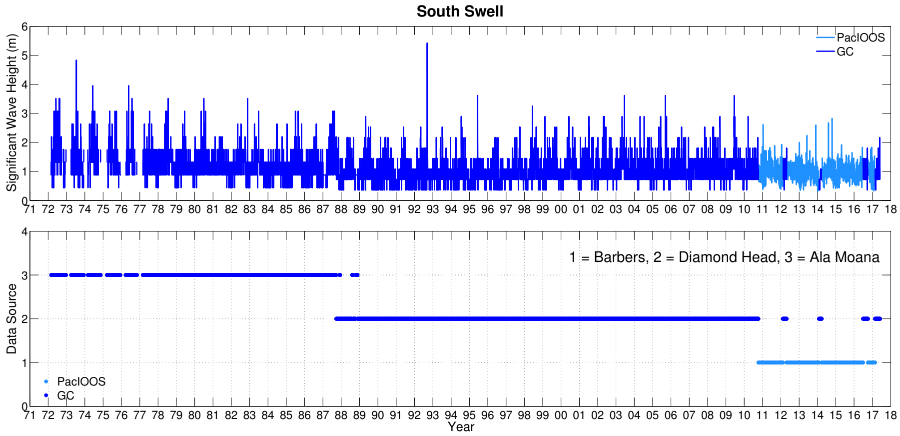

Figure A.11: Long time series for the south swell created by merging the time series from the PacIOOS buoys and the Goddard and Caldwell surf height observations.

The monthly averages of the significant wave height arriving on the south shores is given in Figure A.12. These values are important because on the south shore of Oahu is Waikiki Beach and the wave heights that arrive there have a large impact on the tourism industry.

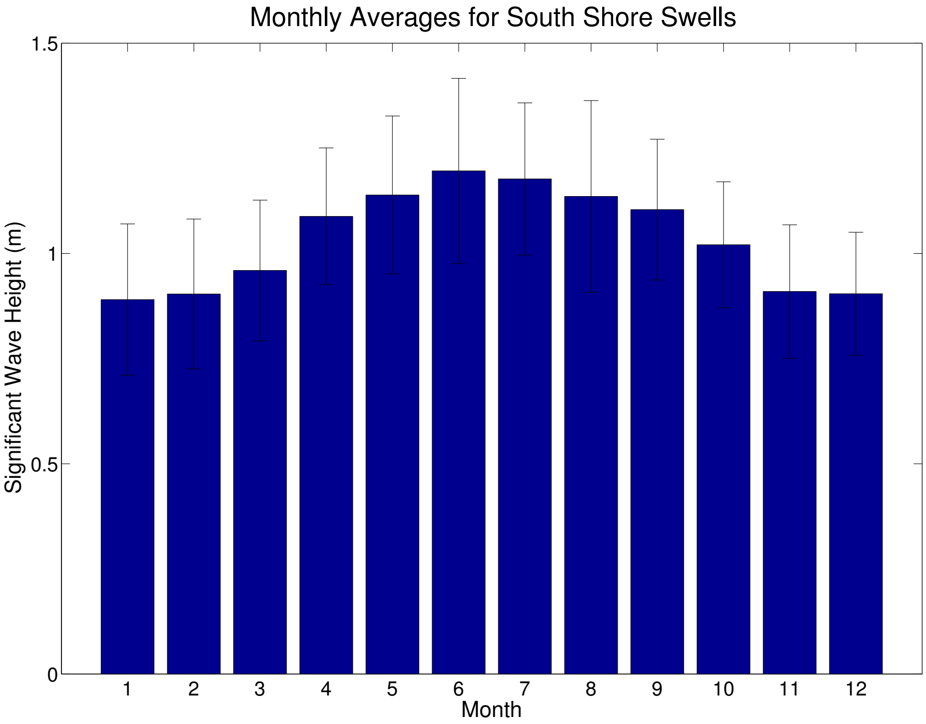

Figure A.12: Monthly average of wave height on the South shore of Oahu.

B | Appendix B

This Appendix includes more of the ESTELA model output for more buoy locations. The Waimea buoy is discussed in Chapter 4.

The most northwestern of the PacIOOS wave buoys is the Hanalei buoy offshore if the island of Kauai. When the position of this buoy is set as the target point in ESTELA, we get a mean effective wave energy flux field similar to what we got for Waimea (Figure B.1). This makes sense because Waimea and Kauai are both on the north shores of islands that have few obstructions between their position and the northwest swell. In the Hanalei output, we can see some energy south near New Zealand that might be part of the south swell that finds its way to the north shore of Kauai. We can also see the trade wind swell generation region to the southeast.

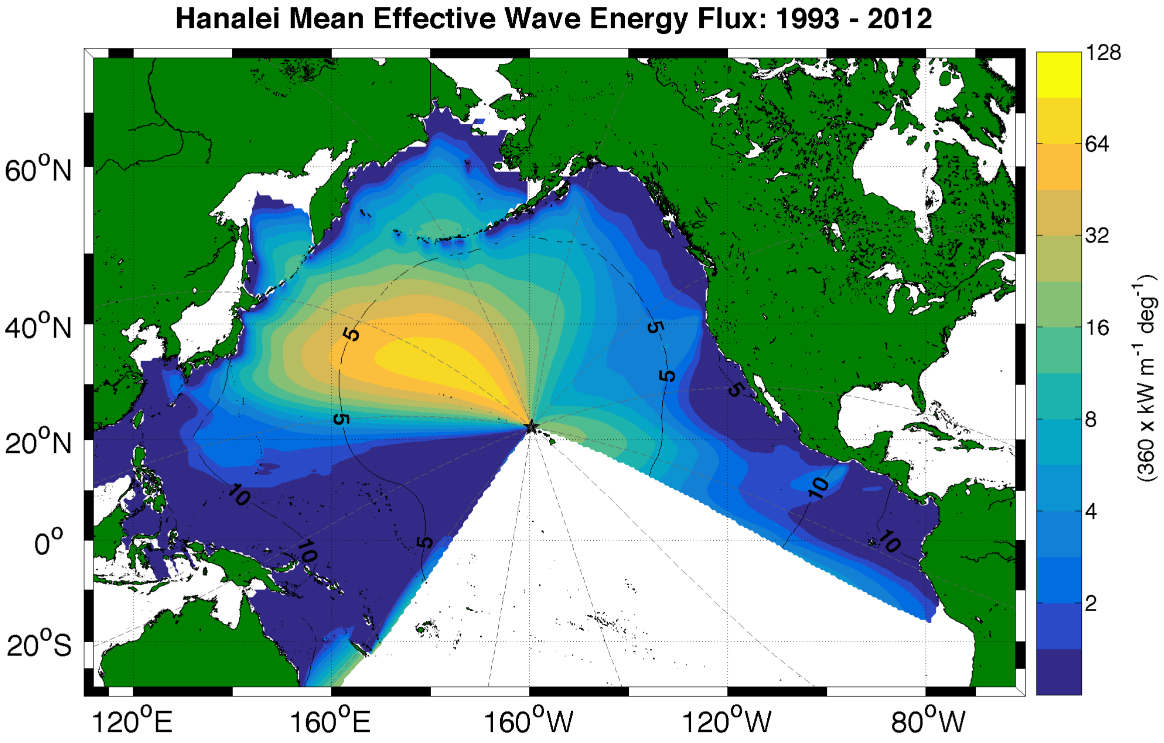

Figure B.1: Mean of monthly effective wave energy flux output from the ESTELA model with the Hanalei buoy as the target point. Contours are approximately the number of days it will take for energy along the contour to reach the target point. Dashed lines are great circle routes wave energy will travel along.

During the summer at Hanalei the northwest swell and the trade wind swell generation regions are still active, but have smaller magnitudes (Figure B.2). During the winter, the northwest swell region becomes more energetic (Figure B.3).

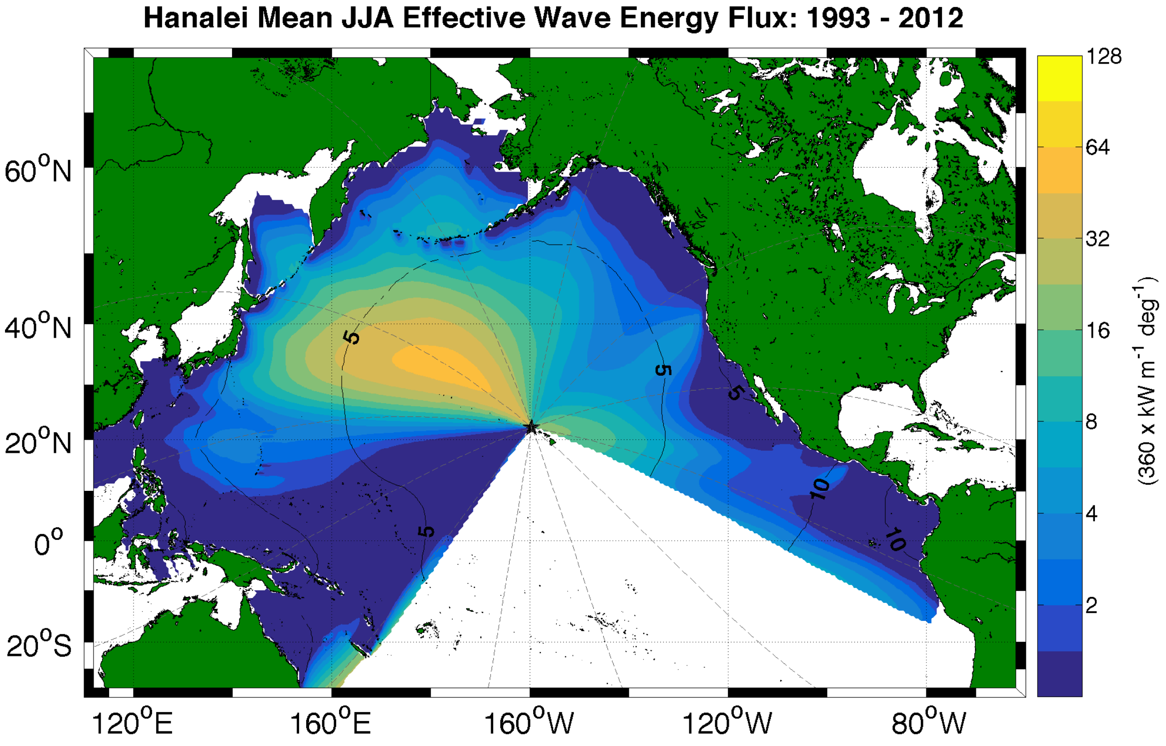

Figure B.2: Mean of summer (June, July, August) effective wave energy flux output from the ESTELA model with the Hanalei buoy as the target point. Contours are approximately the number of days it will take for energy along the contour to reach the target point. Dashed lines are great circle routes wave energy will travel along.

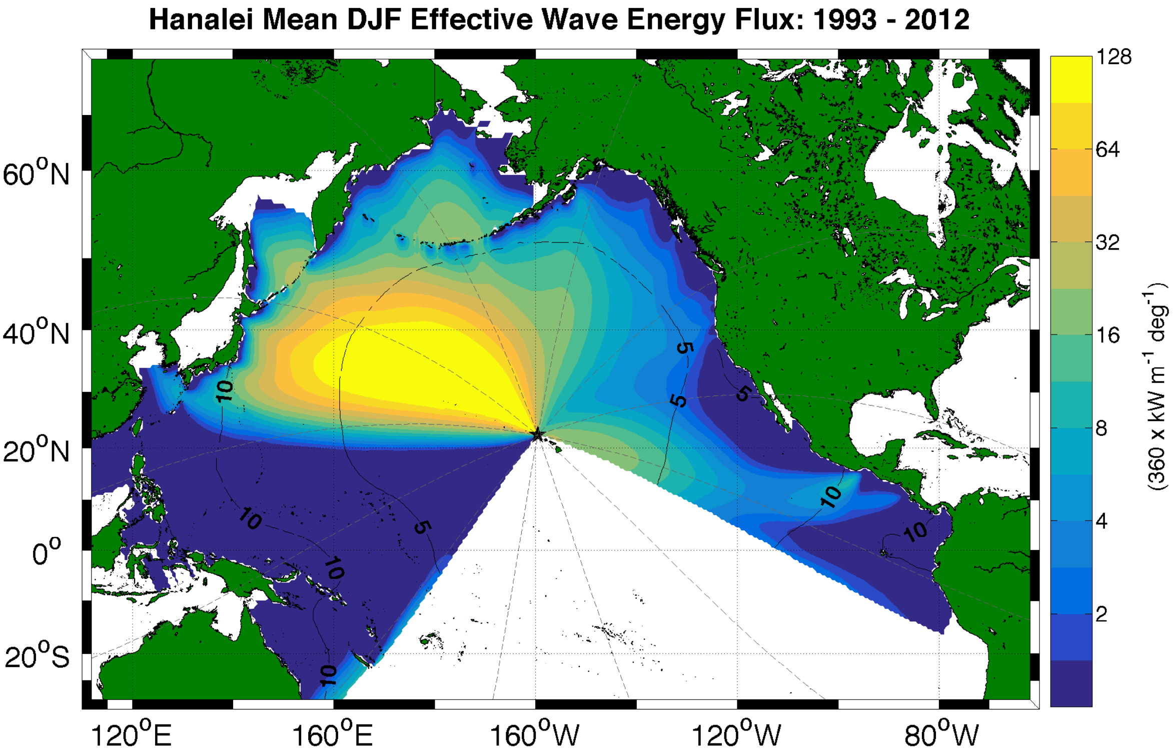

Figure B.3: Mean of winter (December, January, February) effective wave energy flux output from the ESTELA model with the Hanalei buoy as the target point. Contours are approximately the number of days it will take for energy along the contour to reach the target point. Dashed lines are great circle routes wave energy will travel along.

In the case where the Pauwela wave buoy is set as the target point in ESTELA, we can clearly see the impact the geographic criteria has on the model output with the shadowing Kauai and Oahu causes for Pauwela on Maui Island (Figure B.4). This is also why no energy comes from the south in the output, Maui itself blocks the south swell from reaching the north shore in the ESTELA model criteria. Again, at Pauwela we see the northwest swell generation region and a weaker trade wind swell generation region. Summers at Pauwela (Figure B.5) have a weaker northwest swell compared to the high energy winters (Figure B.6).

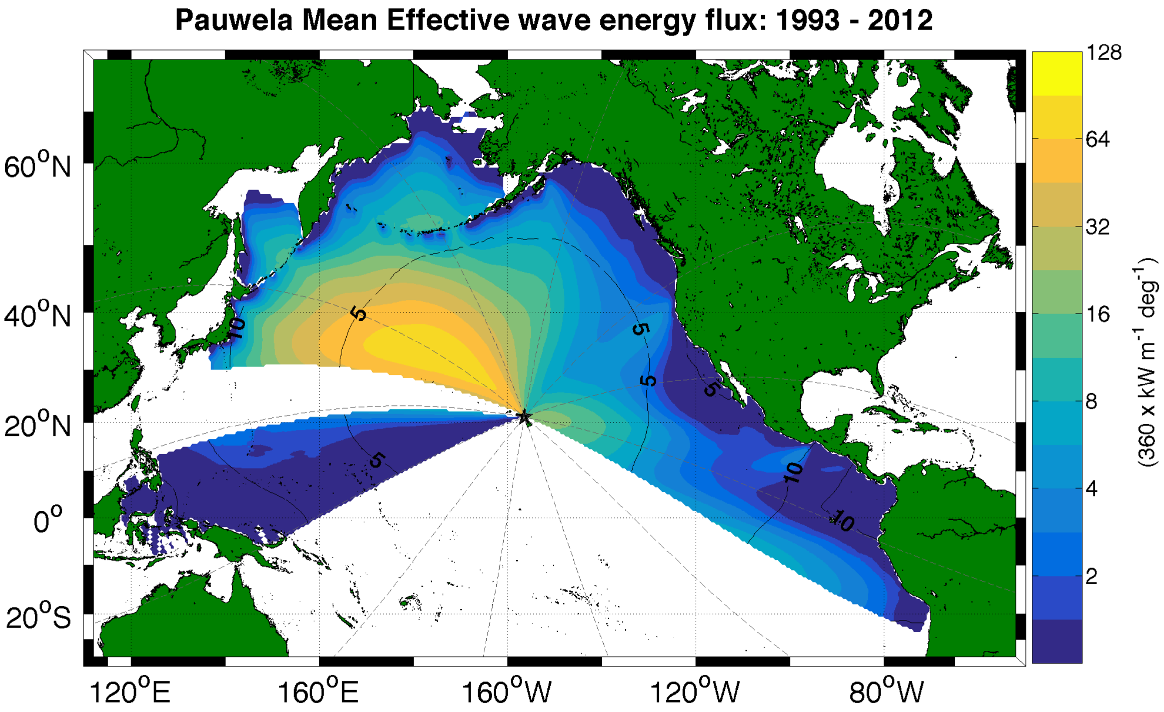

Figure B.4: Mean of monthly effective wave energy flux output from the ESTELA model with the Pauwela buoy as the target point. Contours are approximately the number of days it will take for energy along the contour to reach the target point. Dashed lines are great circle routes wave energy will travel along.

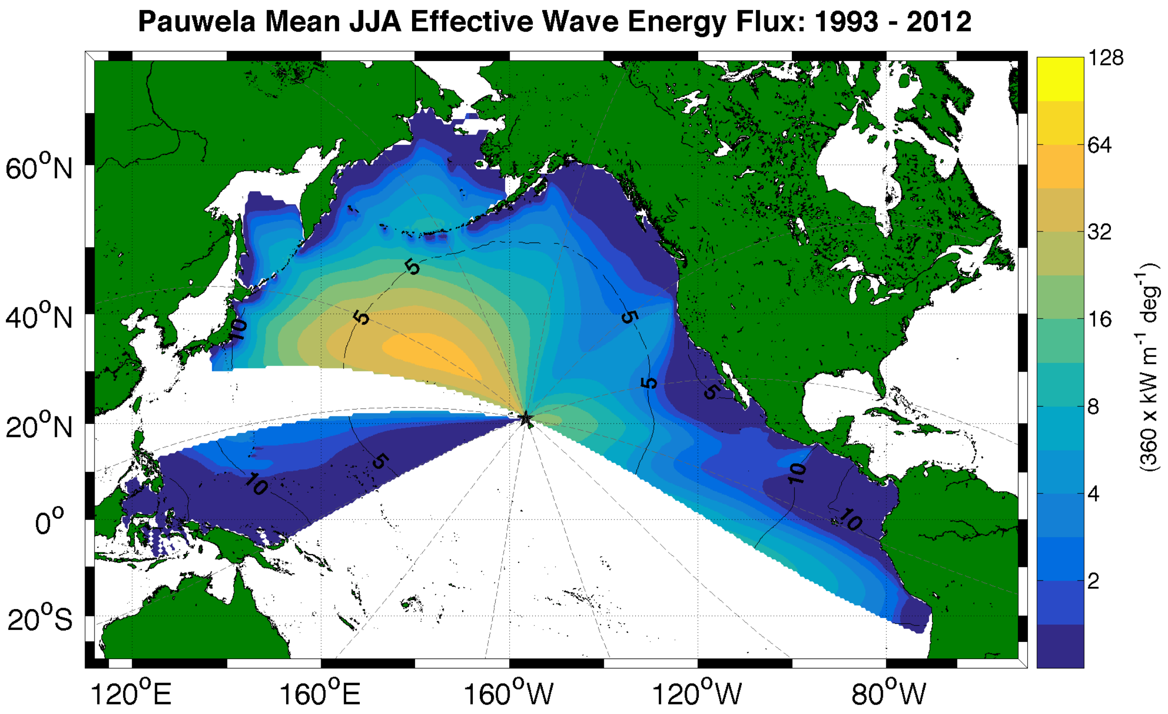

Figure B.5: Mean of summer (June, July, August) effective wave energy flux output from the ESTELA model with the Pauwela buoy as the target point. Contours are approximately the number of days it will take for energy along the contour to reach the target point. Dashed lines are great circle routes wave energy will travel along.

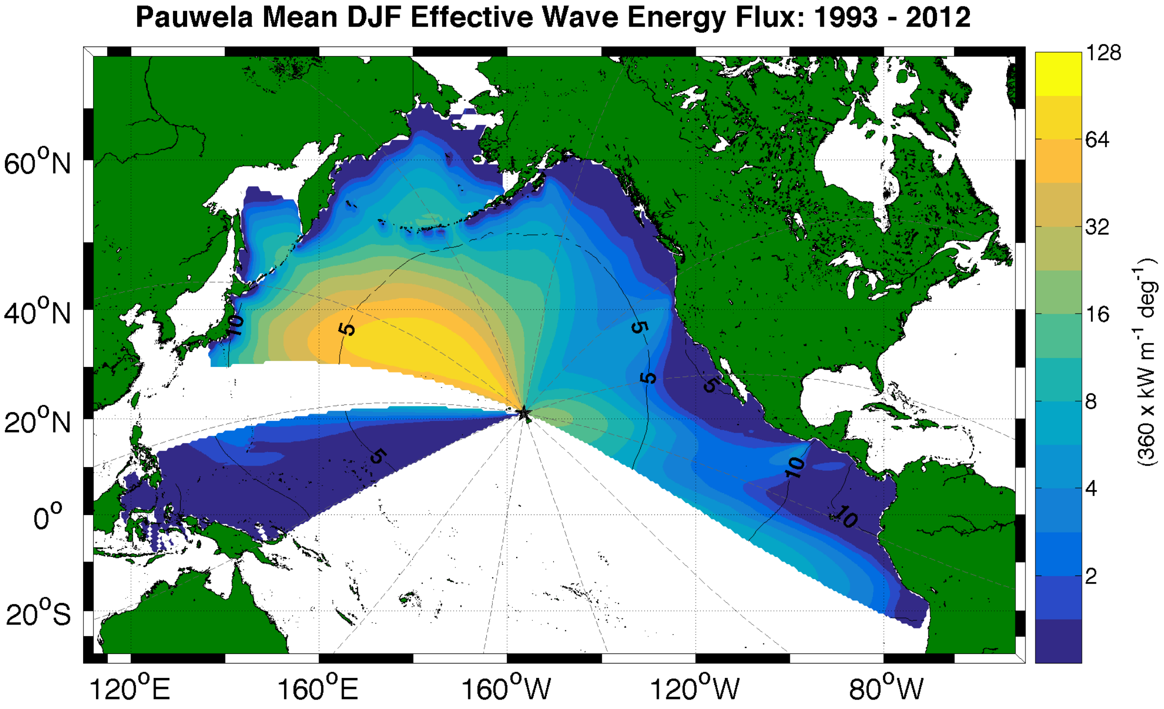

Figure B.6: Mean of winter (December, January, February) effective wave energy flux output from the ESTELA model with the Pauwela buoy as the target point. Contours are approximately the number of days it will take for energy along the contour to reach the target point. Dashed lines are great circle routes wave energy will travel along.

Hilo, the PacIOOS buoy furthest to the east, gives a better picture of the effective wave energy along the eastern Pacific. At Hilo we can still see the northwest swell generation region (Figure B.7). Apart from the trade wind swell generation region, there does not appear to be any comparably energetic regions in the eastern Pacific. In the summer, energy reaching the Hilo buoy gets small everywhere (Figure B.8). During the winter the northwest swell is the most energetic region (Figure B.9).

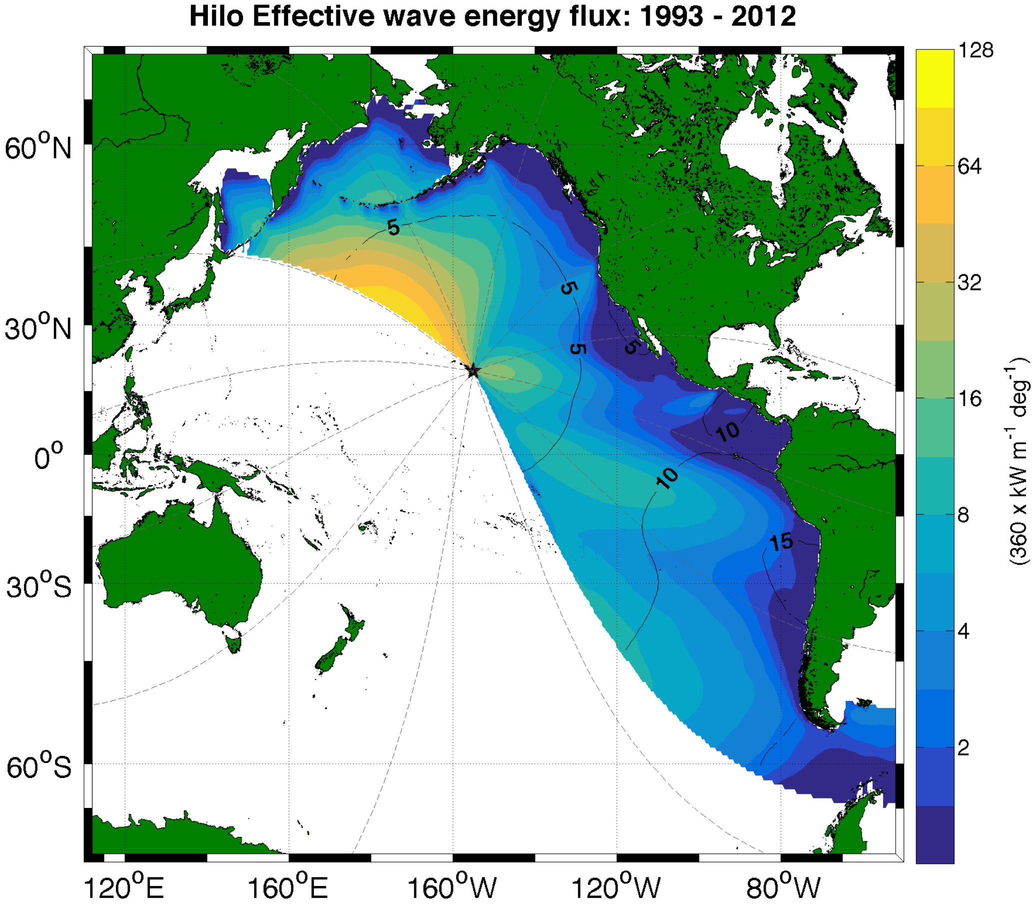

Figure B.7: Mean of monthly effective wave energy flux output from the ESTELA model with the Hilo buoy as the target point. Contours are approximately the number of days it will take for energy along the contour to reach the target point. Dashed lines are great circle routes wave energy will travel along.

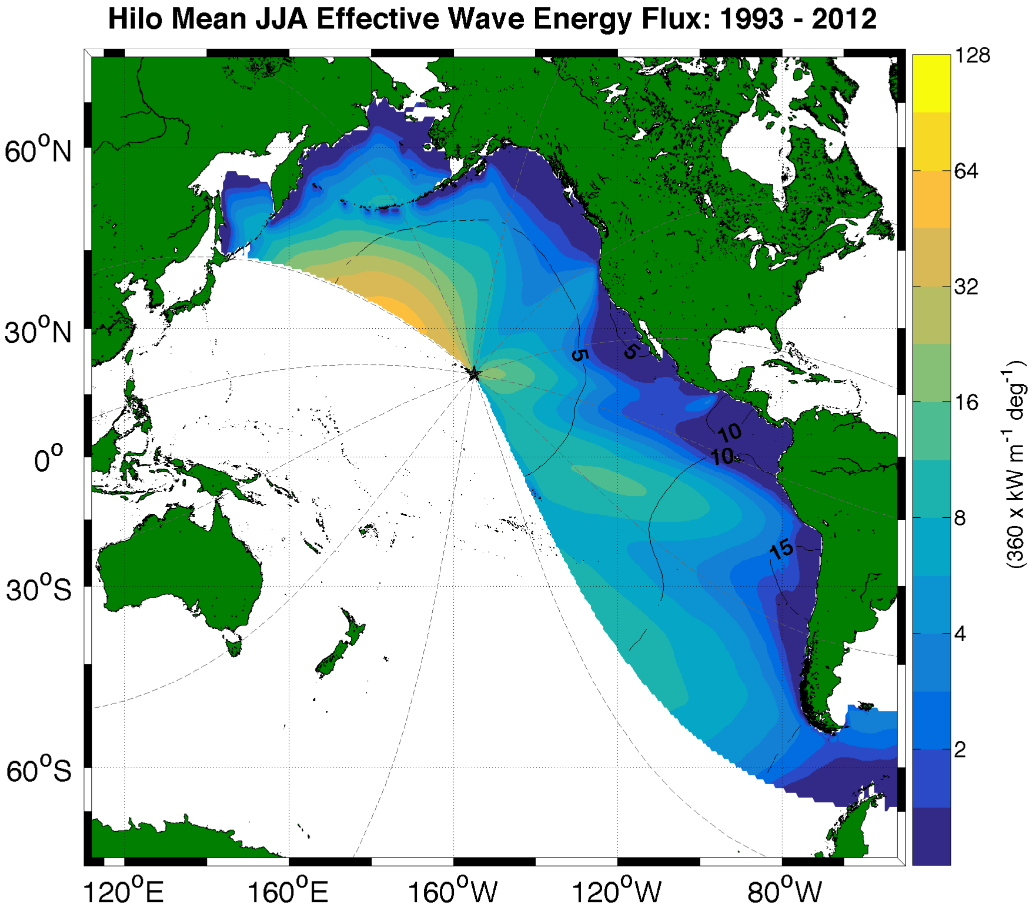

Figure B.8: Mean of summer (June, July, August) effective wave energy flux output from the ESTELA model with the Hilo buoy as the target point. Contours are approximately the number of days it will take for energy along the contour to reach the target point. Dashed lines are great circle routes wave energy will travel along.

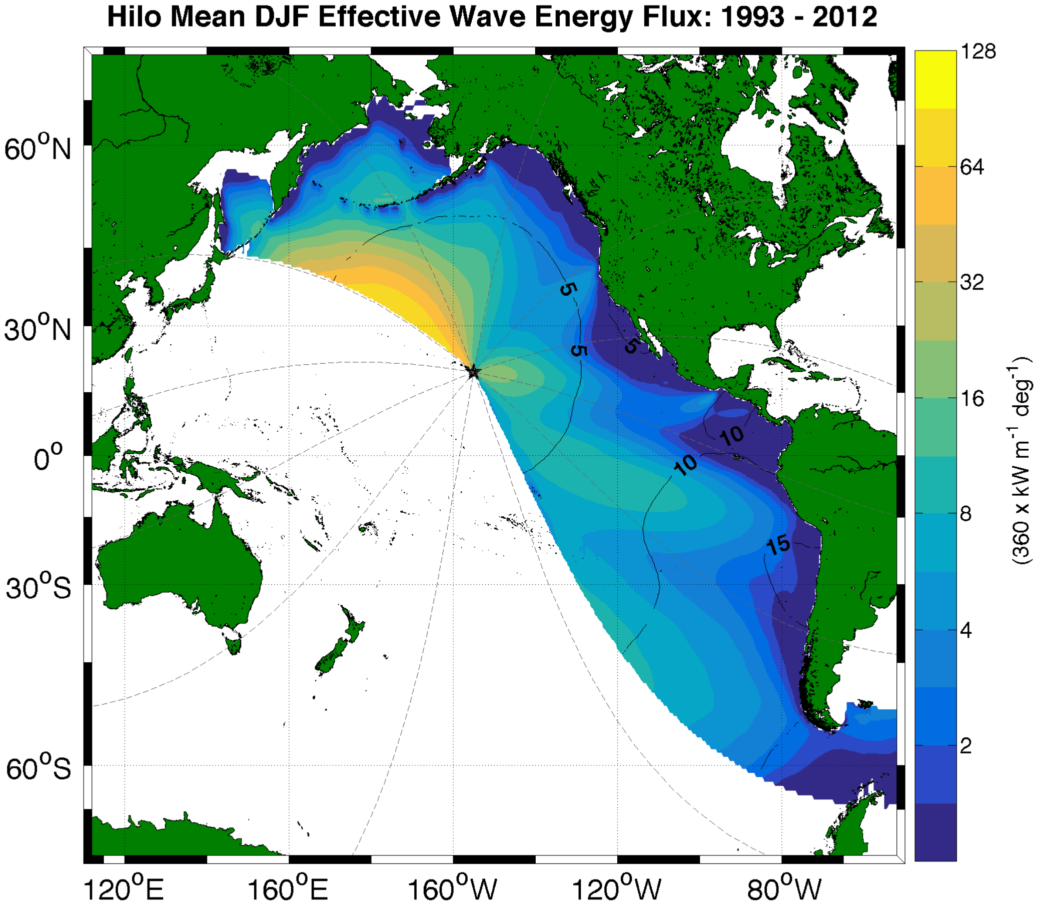

Figure B.9: Mean of winter (December, January, February) effective wave energy flux output from the ESTELA model with the Hilo buoy as the target point. Contours are approximately the number of days it will take for energy along the contour to reach the target point. Dashed lines are great circle routes wave energy will travel along.

By setting buoy 51000 as the target point in ESTELA, we get a very nice picture of what the entire Pacific Ocean is doing in terms of effective wave energy (Figure B.10). The output shows the northwest swell we are familiar with, the trade wind swell, and a new picture of the south swell generation region. During the summer, the south swell can be quite large (Figure B.11). The ESTELA output suggests that the northwest swell we see in Hawai'i is a result of energy generation on either side of New Zealand with the most energy coming from near Tasmania. The south swell energy takes approximately ten days to get to the Hawaiian Islands. After being generated, the energy has a long distance to travel to reach Hawai'i which will act to sort the wave trains. In the winter, the northwest swell and the south swell are comparable in magnitude in the map, but the northwest swell is closer.

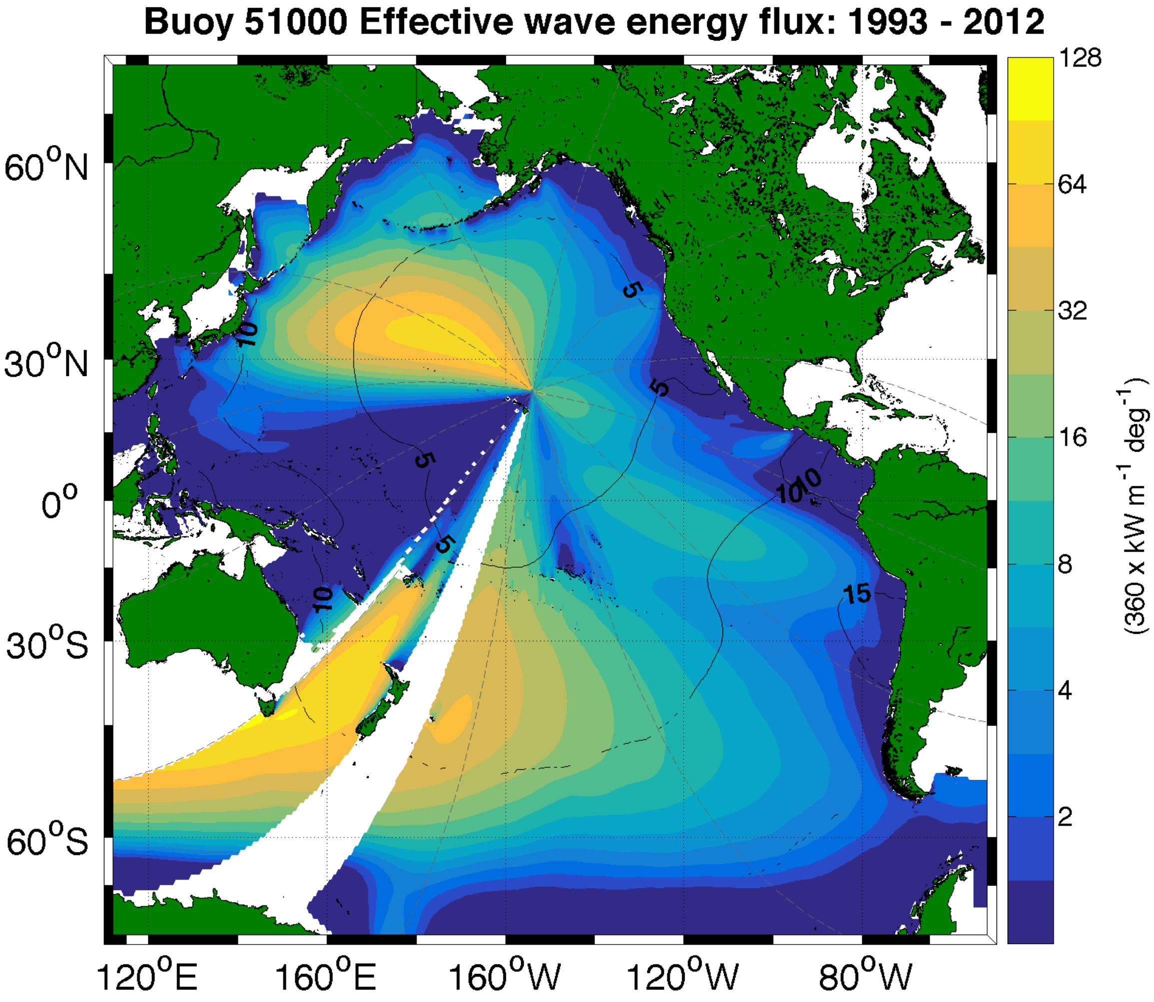

Figure B.10: Mean of monthly effective wave energy flux output from the ESTELA model with buoy 51000 as the target point. Contours are approximately the number of days it will take for energy along the contour to reach the target point. Dashed lines are great circle routes wave energy will travel along.

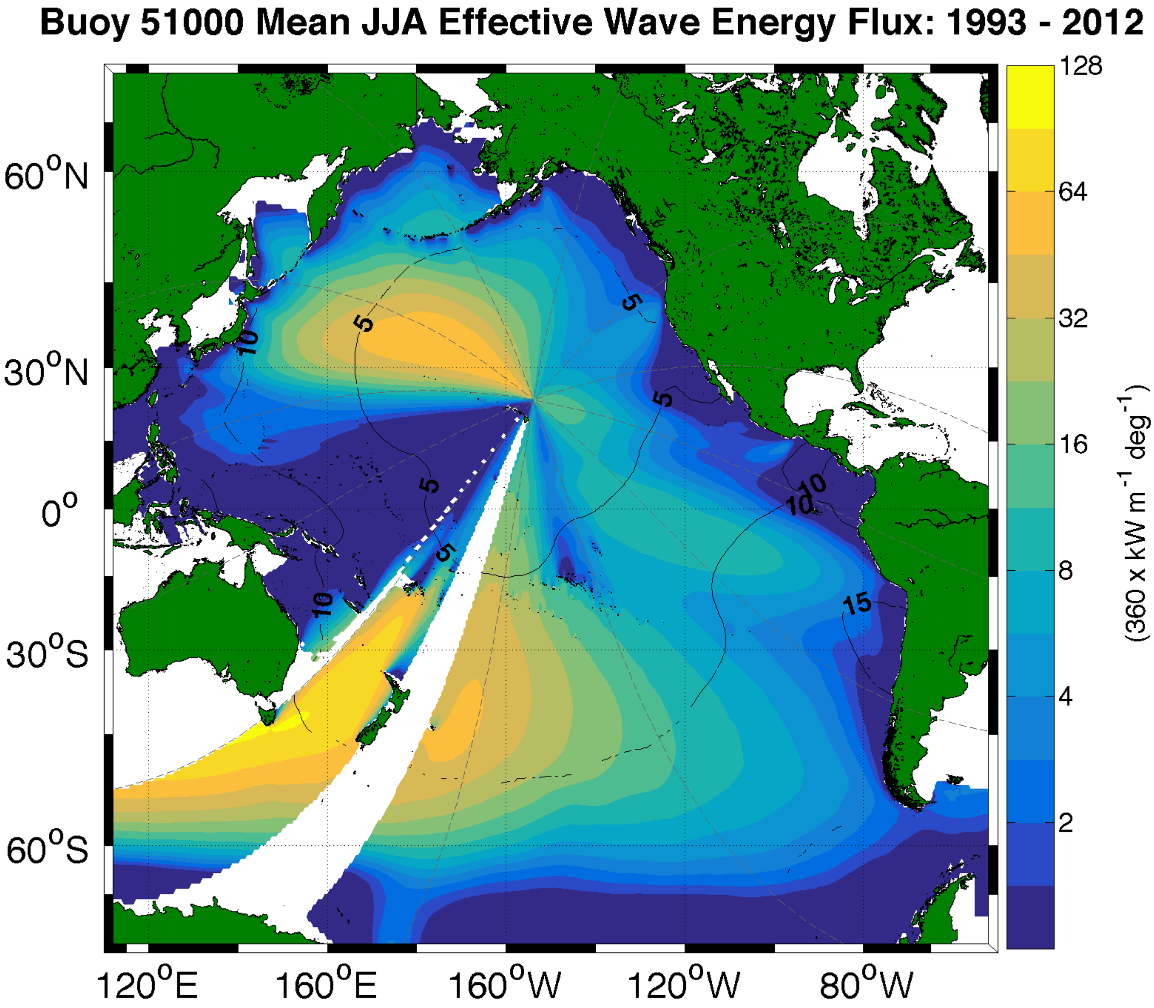

Figure B.11: Mean of summer (June, July, August) effective wave energy flux output from the ESTELA model with buoy 51000 as the target point. Contours are approximately the number of days it will take for energy along the contour to reach the target point. Dashed lines are great circle routes wave energy will travel along.

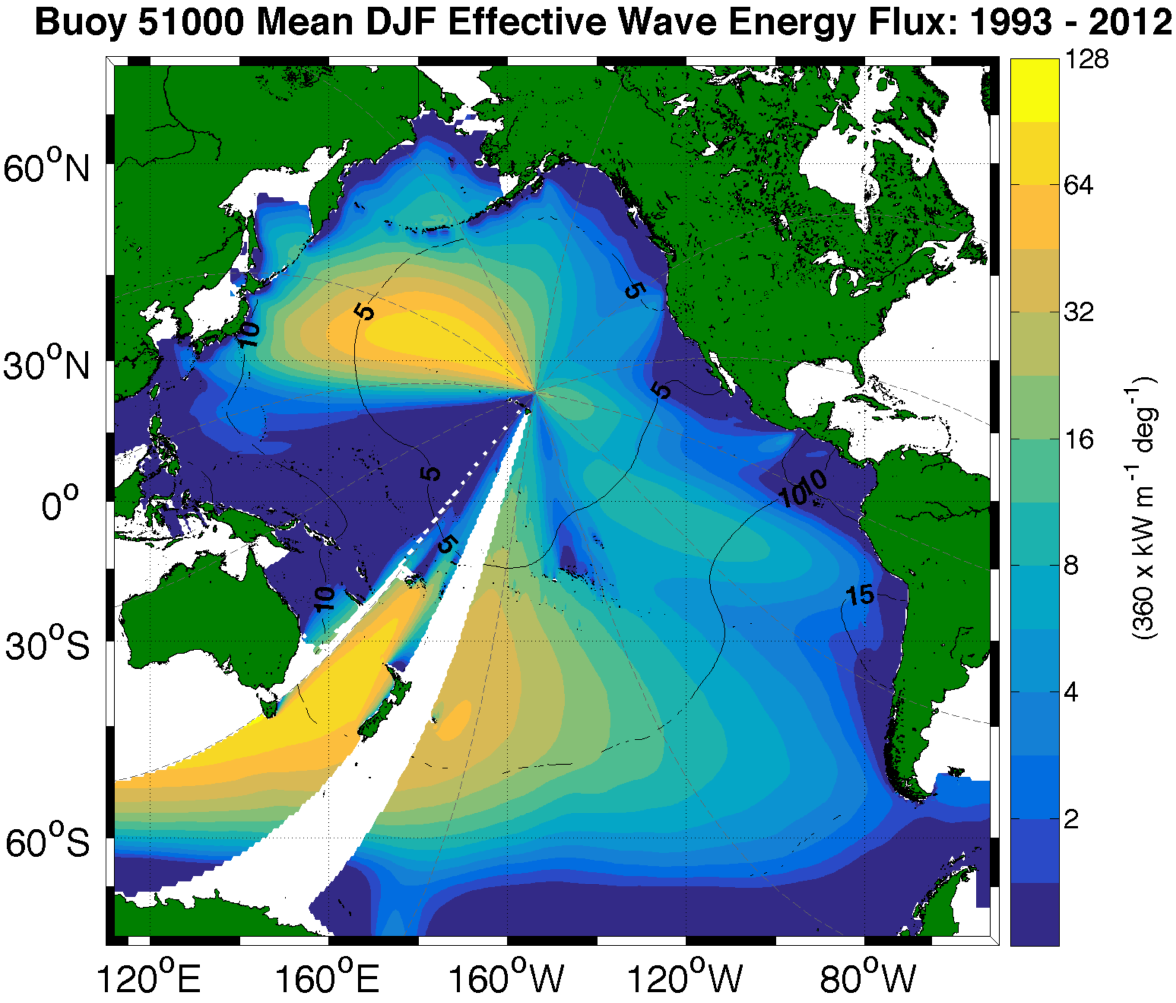

Figure B.12: Mean of winter (December, January, February) effective wave energy flux output from the ESTELA model with buoy 51000 as the target point. Contours are approximately the number of days it will take for energy along the contour to reach the target point. Dashed lines are great circle routes wave energy will travel along.

Buoy 51003 is on the south side of the islands and gets a more complete picture of what is going on around New Zealand (Figure B.13). Summers and winters are very similar to what was seen for buoy 51000 (Figures B.14-B.15).

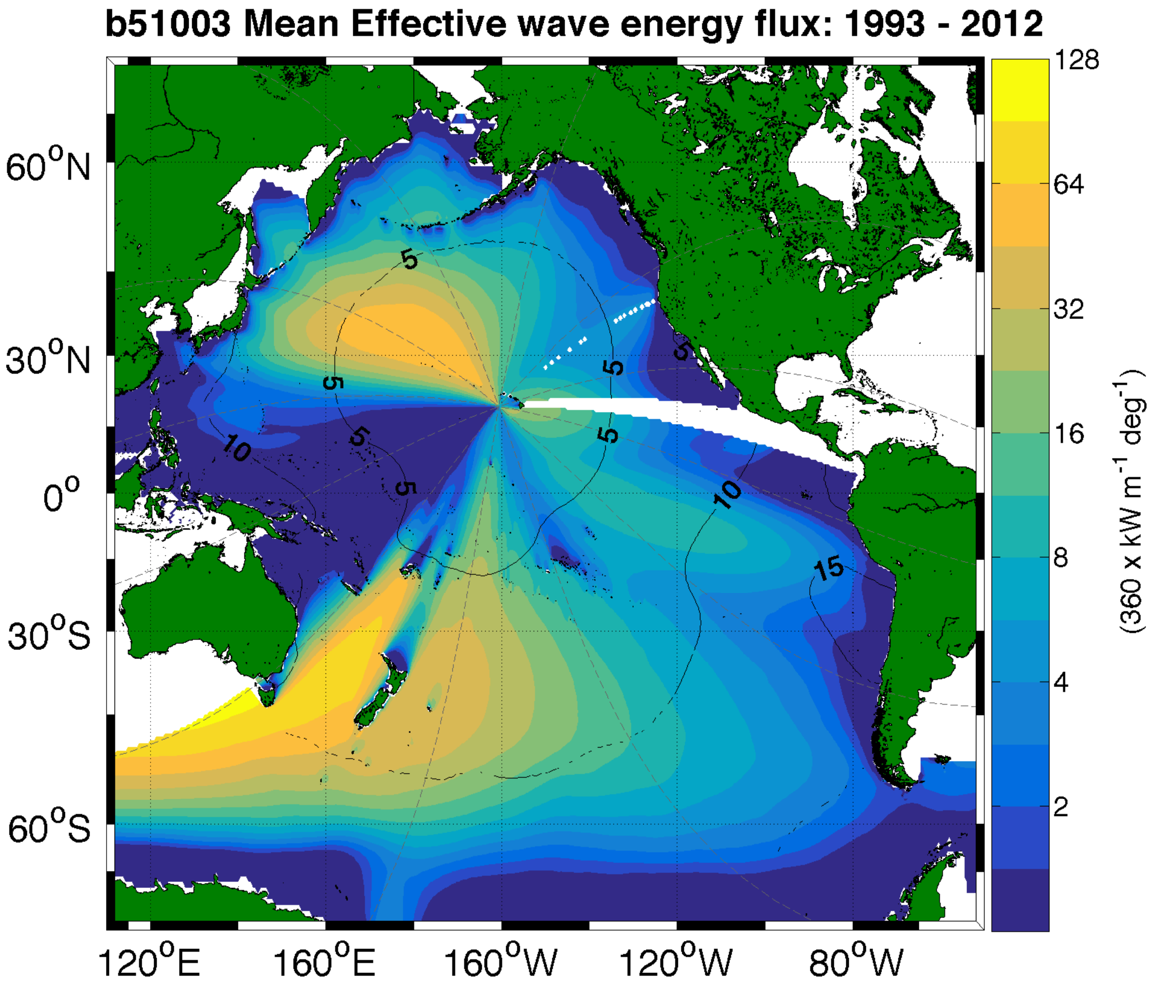

Figure B.13: Mean of monthly effective wave energy flux output from the ESTELA model with buoy 51003 as the target point. Contours are approximately the number of days it will take for energy along the contour to reach the target point. Dashed lines are great circle routes wave energy will travel along.

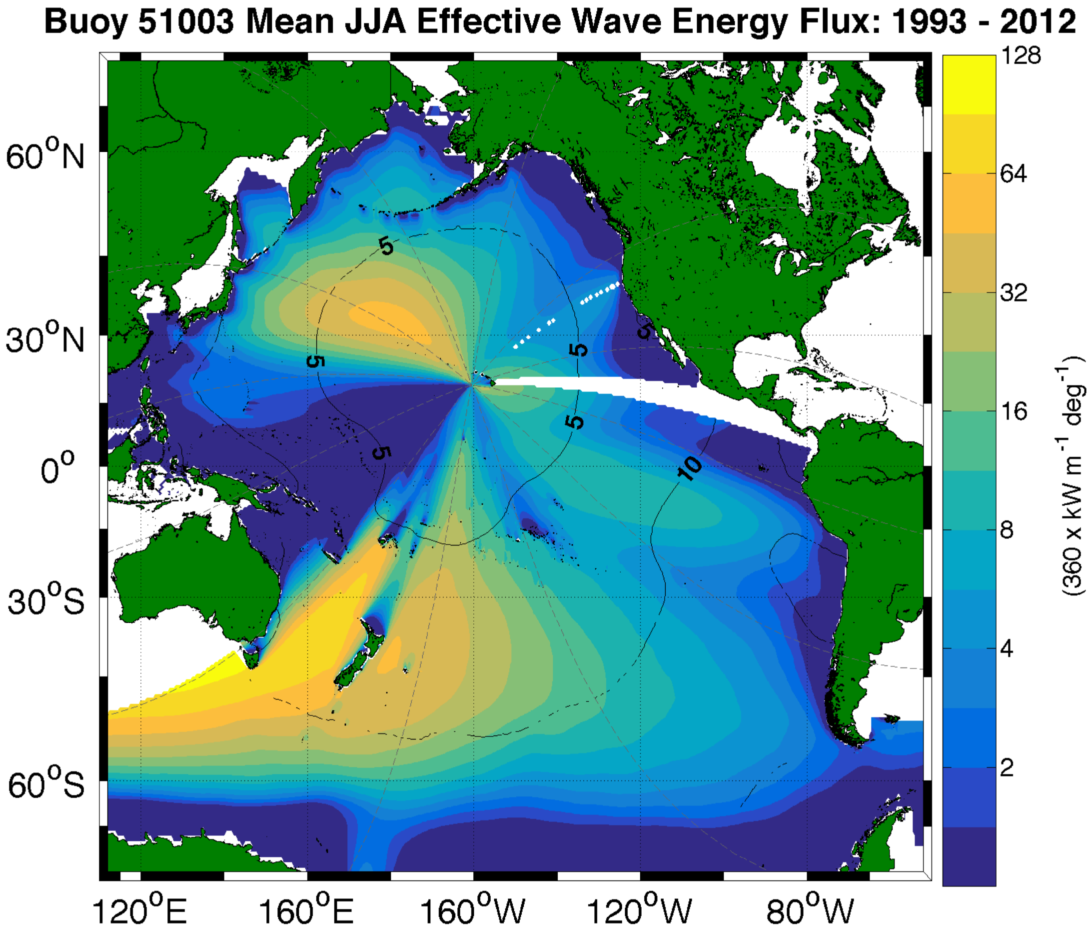

Figure B.14: Mean of summer (June, July, August) effective wave energy flux output from the ESTELA model with buoy 51003 as the target point. Contours are approximately the number of days it will take for energy along the contour to reach the target point. Dashed lines are great circle routes wave energy will travel along.

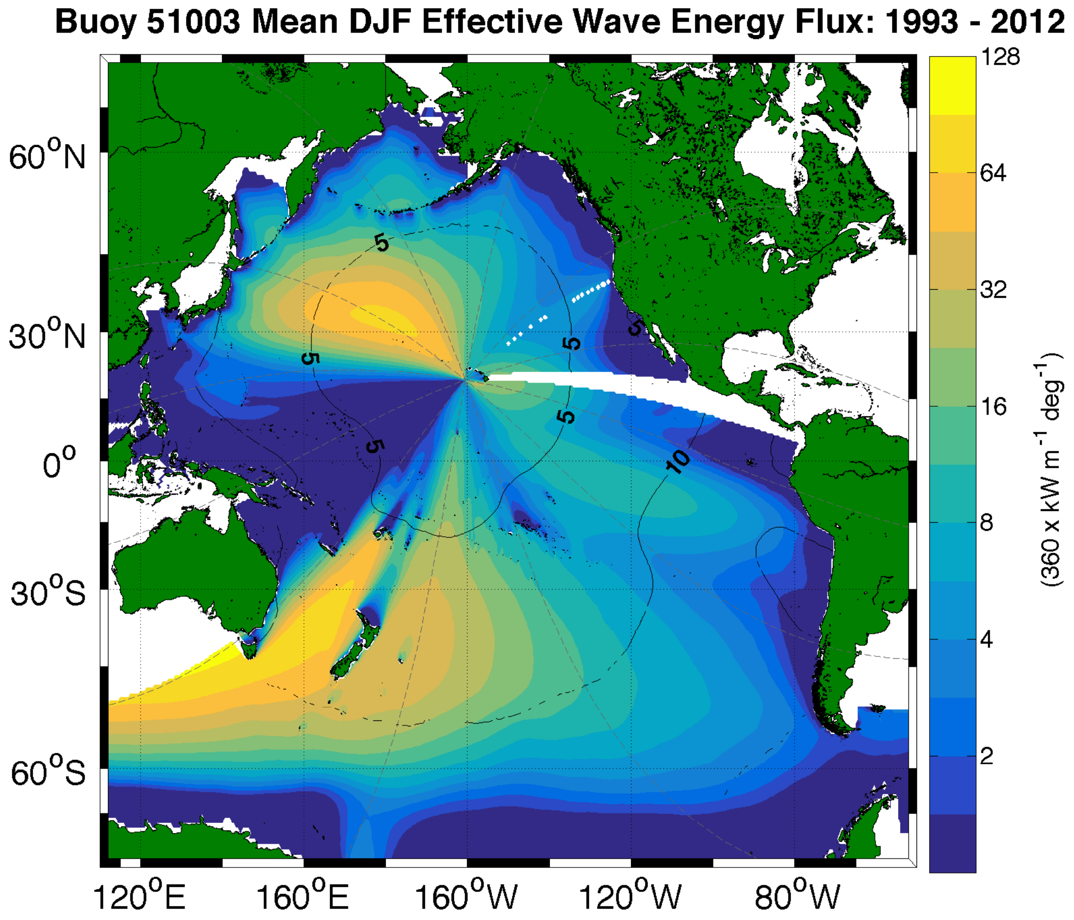

Figure B.15: Mean of winter (December, January, February) effective wave energy flux output from the ESTELA model with buoy 51003 as the target point. Contours are approximately the number of days it will take for energy along the contour to reach the target point. Dashed lines are great circle routes wave energy will travel along.

Buoy 51004, on the southeastern side of the Hawaiian Islands gets blocked by the Islands to much of the northwest swell energy (Figure B.16). In the summers and winters are very similar to the output for buoy 51003 (Figures B.17-B.18).

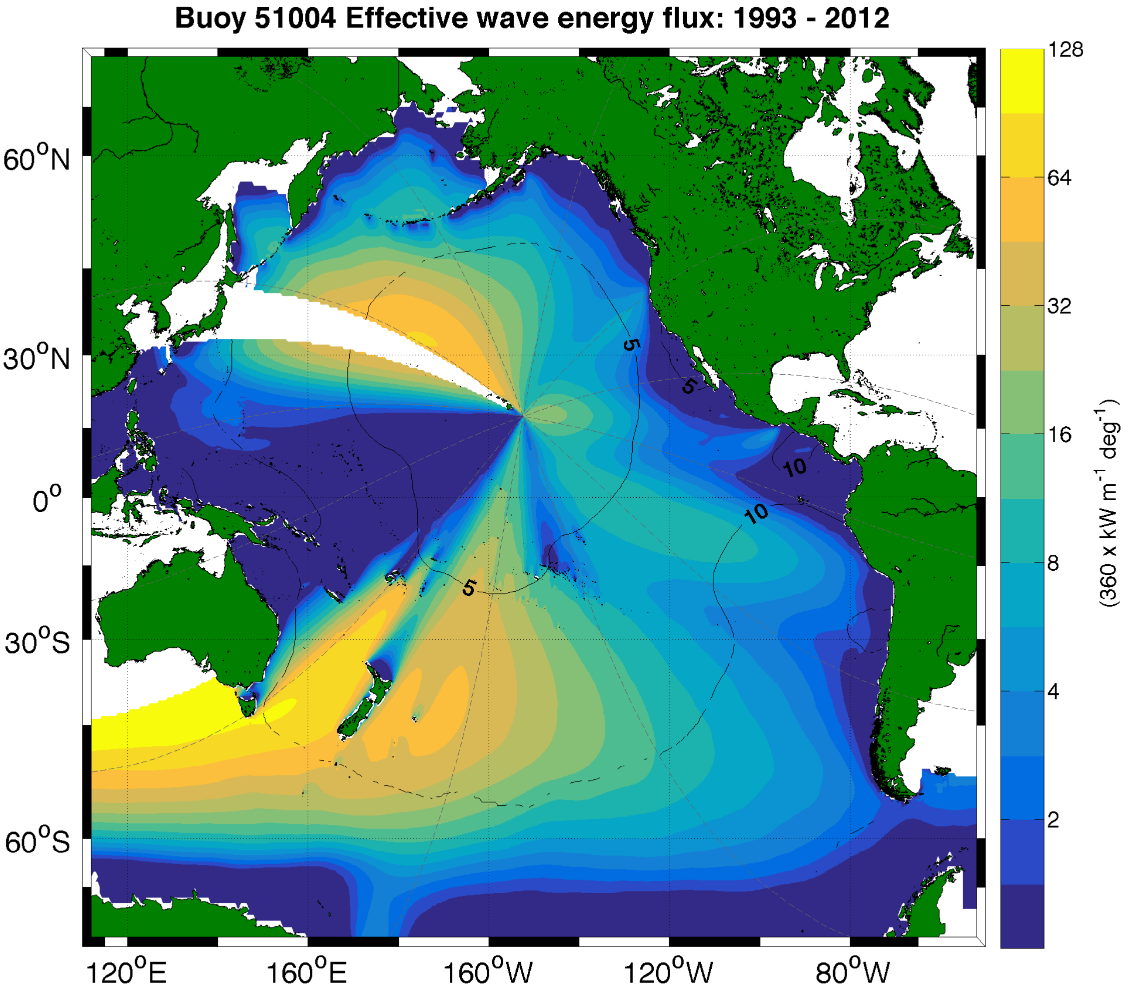

Figure B.16: Mean of monthly effective wave energy flux output from the ESTELA model with buoy 51004 as the target point. Contours are approximately the number of days it will take for energy along the contour to reach the target point. Dashed lines are great circle routes wave energy will travel along.

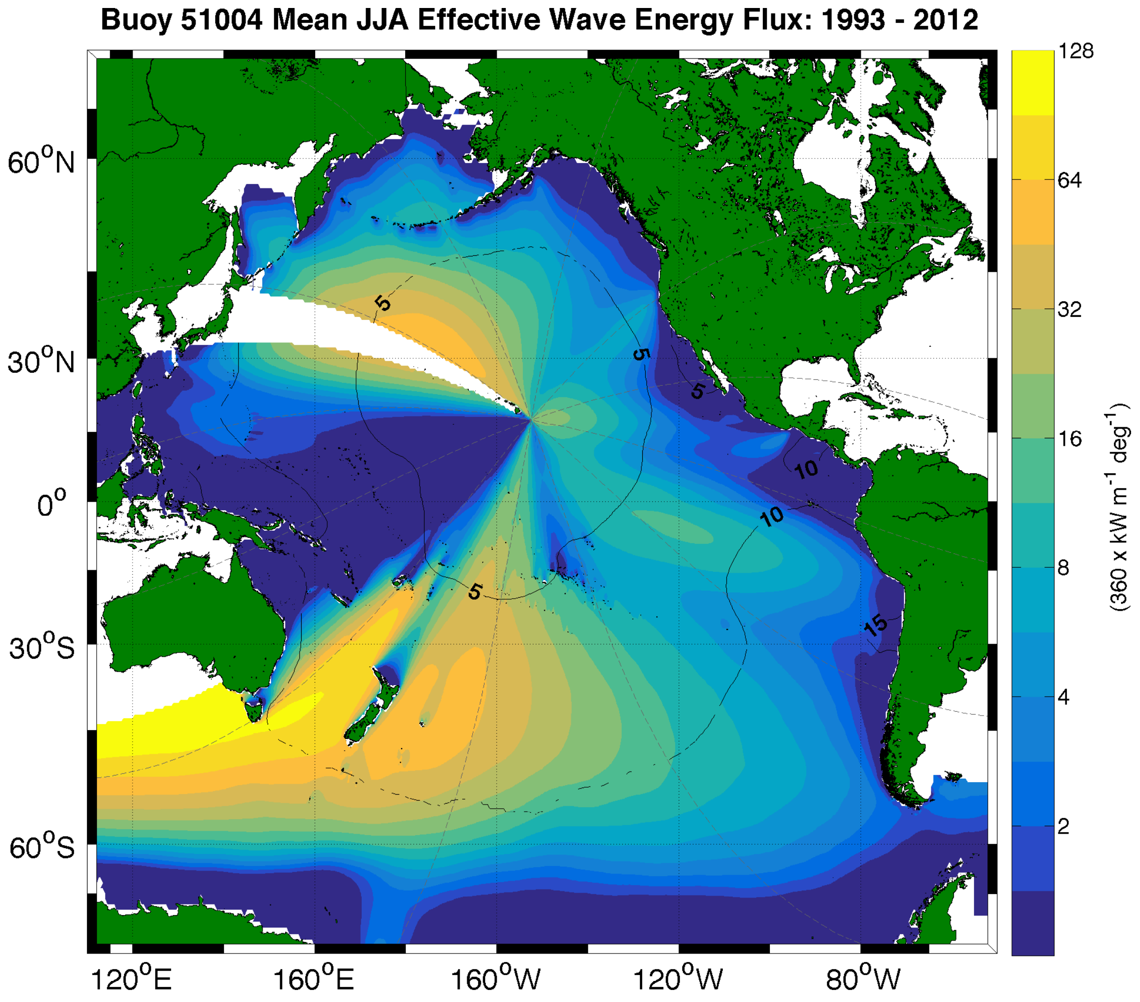

Figure B.17: Mean of summer (June, July, August) effective wave energy flux output from the ESTELA model with buoy 51004 as the target point. Contours are approximately the number of days it will take for energy along the contour to reach the target point. Dashed lines are great circle routes wave energy will travel along.

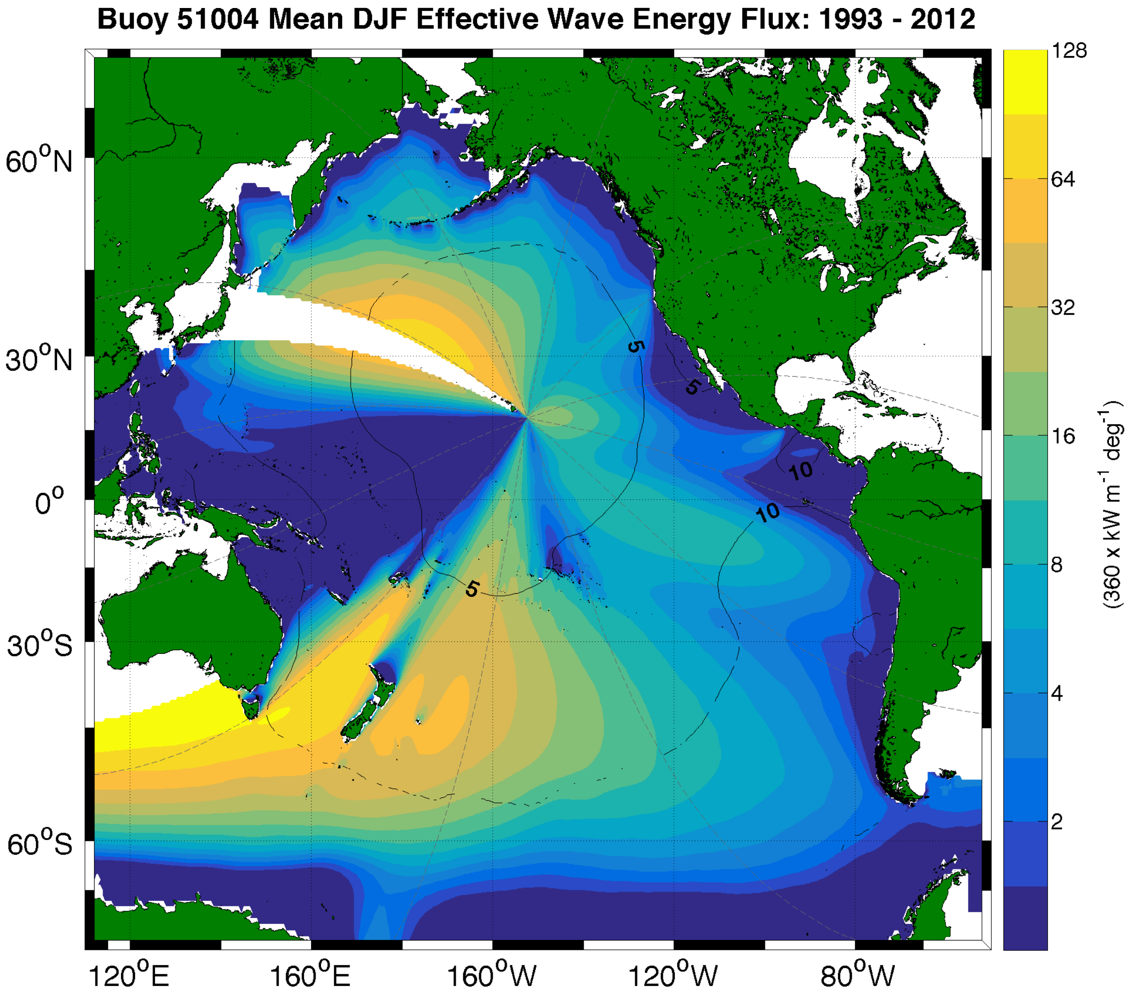

Figure B.18: Mean of winter (December, January, February) effective wave energy flux output from the ESTELA model with buoy 51004 as the target point. Contours are approximately the number of days it will take for energy along the contour to reach the target point. Dashed lines are great circle routes wave energy will travel along.

These ESTELA output maps give us some insight into why the older non-directional data are not very accurate when we make the buoy time series (Figure 3.4). There are lots of swell types that interact with each buoy even in just the winter. A measure of significant wave height without a filter for frequency or direction is not an accurate representation of a given swell direction.

References

Adams, P., Inman, D., Graham, N., 2008. Southern california deep-water wave climate: Characterization and application to coastal processes. Journal of Coastal Research 24, 1022–1035. doi:`10.2112/07-0831.1`.

Agustin, A., Merrifield, M., Potemra, J., Morishige, C., 2015. Temporal variability of marine debris deposition at tern island in the northwestern hawaiian islands. Marine Pollution Bulletin 101, 200–207. doi:`10.1016/j.marpolbul.2015.10.076`.

Alexander, M., Blade, I., Newman, M., Lanzante, J., Lau, N., Scott, J., 2002. The atmospheric bridge: The influence of enso teleconnections on air?sea interaction over the global oceans. American Meteorological Society 15, 2205–2231.

Anderson, T., Fletcher, C., Barbee, M., Frazer, L., Romine, B., 2015. Doubling of coastal erosion under rising sea level by mid-century in hawaii. Natural Hazards doi:`10.1007/s11069-015-1698-6`.

Ardhuin, F., Chapron, B., Collard, F., 2009. Observation of swell dissipation across oceans. Geophysical Research Letters doi:`10.1029/2008GL037030`.

Aucan, J.P., 2006. Directional wave climatology for the hawaiian islands from buoy data and the influence of enso on extreme wave events from wave model hindcast. In: Proceedings of the 9th International Workshop on Wave Hindcasting and Forecasting (Victoria, British Columbia, Environment Canada, the U.S. Army Engineer Research and Development .

Barnard, P., Hoover, D., Hubbard, D., Snyder, A., Ludka, B., Allan, J., Kaminsky, G., Ruggiero, P., Gallien, T., Gabel, L., McCandless, D., Weiner, H., Cohn, N., Anderson, D., Serafin, K., 2017. Extreme oceanographic forcing and coastal response due to the 2015-2016 el niño. Nature Communications 8, 1–8. doi:`10.1038/ncomms14365`.

Barnard, P., Short, A., Harley, M., Splinter, K., Vitousek, S., Turner, I., Allan, J., Banno, M., Bryan, K., Doria, A., Hansen, J., Kato, S., Kuriyama, Y., Randall-Goodwin, E., Ruggiero, P., Walker, I., Heathfield, D., 2015. Coastal vulnerability across the pacific dominated by el niño/southern oscillation. Nature Geoscience 8, 801–808. doi:`10.1038/NGEO2539`.

Barnston, A.G., Chelliah, M., Goldenberg, S.B., 1997. Documentation of a highly enso-related sst region in the equatorial pacific. Atmos.-Ocean , 367–383.

Biondi, F., Gershunov, A., Cayan, D., 2001. North pacific decadal climate variability since 1661. Journal of Climate 14, 5–10.

Briganti, R., Torres-Freyermuth, A., Baldock, T.E., Brocchini, M., Dodd, N., Hsu, T., Jiang, Z., Kim, Y., Pintade-Patiño, J.C., Postacchini, M., 2016. Advances in numerical modelling of swash zone dynamics. Coastal Engineering , 26–41doi:`10.1016/j.coastaleng.2016.05.001`.

Bromirski, P., Cayan, D., Flick, R., 2005. Wave spectral energy variability in the northeast pacific. Journal of Geophysical Research , C03005.doi:`10.1029/2004JC002398`.

Bromirski, P.D., Flick, R.E., Graham, N., 1999. Ocean wave height determined from inland seismometer data: Implications for investigating wave climate changes in the ne pacific. Journal of Geophysical Research , 20,753–20,766.

Bruun, P., 1962. Sea-level rise as a cause of shore erosion. Journal of the Waterways and Harbors Division 88, 117–130.

Caccamise, D., Merrifield, M., Bevis, M., Foster, J., Firing, Y., Schenwerk, M., Taylor, F., Thomas, D., 2005. Sea level rise at honolulu and hilo, hawaii: Gps estimates of differential land motion. Geophysical Research Letters , L03607.

Caldwell, C., 2005. Validity of north shore, oahu, hawaiian islands surf observations. Journal of Coastal Research , 1127–1138doi:`10.2112/03-0092.1`.

Caldwell, C., Aucan, J., 2007. An empirical method for estimating surf heights from deepwater significant wave heights and peak periods in coastal zones with narrow shelves, steep bottom slopes, and high refraction. Journal of Coastal Research 23, 1237–1244. doi:`10.2112/04-0397R.1`.

Caldwell, C.P., Vitousek, S., Auncan, J.P., 2009. Frequency and duration of coinciding high surf and tides along the north shore of oahu, hawaii, 1981-2007. Journal of Coastal Research , 734–743doi:`10.2112/08-1004.1`.

Caldwell, P., NESDIS, U.D.N., 2011. Goddard and caldwell: Oahu, hawaii surf observation data set for 1968 - 2004 (nodc accession 0001754). version 1.1. national oceanographic data center, noaa. dataset. [may 30, 2017]. National Oceanographic Data Center .

Camargo, S., Sobel, A., 2005. Western north pacific tropical cyclone intensity and enso. Journal of Climate 18, 2296–3006.

Campbell, T.J., Benedet, L., 2006. Beach nourishment magnitudes and trends in the u.s. Journal of Coastal Research , 57–64.

Chan, D., Zhang, Y., Wu, Q., 2017. Variability in strength and position of the 1 east asian jet stream: 2 dynamics and its linkage to extratropical large-scale circulations. Manuscript submitted for publication to the Journal of Climate .

Chan, J.C.L., Liu, K.S., 2004. Global warming and western north pacific typhoon activity from an observational perspective. Journal of Climate 17, 4590–4602. doi:`10.1175/3240.1`.

Collard, R., Ardhun, F., Chapron, B., 2009. Monitoring and analysis of ocean swell fields from space: new methods for routine observations. Journal of Geophysical Research , C07023.doi:`10.1029/2008JC005215`.

D., E., Fletcher, C., 2002. Longshore sediment transport rates on a reef-fronted beach: Field data and empirical models kaanapali beach, hawaii. Journal of Coastal Research , 649–663.

Dail, H., Merrifield, M., Bevis, M., 2000. Steep beach morphology changes due to energetic wave forcing. Marine Geology 162, 443–458.

Dean, R., Dalrymple, R., 1991. Water Wave Mechanics for Engineers and Scientists. Advanced series on ocean engineering, World Scientific.

Dore, B., 1978. Some effects of the air-water interface on gravity waves. Geophysical Astrophysics Fluid Dynamics , 215–230.

Filipot, J.F., Cheung, K., 2012. Spectral wave modeling for fringing reef environment. Coastal Eng. 67, 67–79.

Firing, Y.L., Merrifield, M.A., 2004. Extreme sea level events at hawaii: Influence of mesoscale eddies. Geophysical Research Letters , L24306doi:`10.1029/2004GL021539`.

Flament, P., Kennan, S., Lumpkin, R., Sawyer, M., Stroup, E., 1996. The ocean atlas of hawaii. Department of Oceanography, School of Ocean and Earth Science and Technology, University of Hawaii (poster). .

Fletcher, C.H., 2010. Hawaii's changing climate, briefing sheet. University of Hawaii Sea Grant College Program, Center for Island Climate Adaptation and Policy, Honolulu , 7p.

Fletcher, C.H., Grossman, E., Richmond, B., Gibbs, A., 2002. Atlas of natural hazards in the hawaiian coastal zone. U.S. Geological Survey Geological Investigations Series , 182–183.

Fletcher, C.H., Mullane, R.A., Richmond, B.M., 1997. Beach loss along armored shorelines on oahu, hawaiian islands. Journal of Coastal Research , 209–215.

Fletcher, C.H., Romine, B.M., Genz, A.S., Barbee, M.M., Dyer, M., Anderson, T.R., Lim, S.C., Vitousek, S., Bochicchio, C., Richmond, B.M., 2012. National assessment of shoreline change: historical shoreline change in the hawaiian islands. U.S. Geological Survey Open-File Report .

Fletcher, C.H., Rooney, B.J., Lim, S.C., Richmond, B., 2003. Mapping shoreline change using digital orthophotogrammetry on maui, hawaii. Journal of Coastal Research , 106–124.

Gan, B., Wu, L., Li, S., Cai, W., Nakamura, H., Alexander, M., Miller, A., 2017. On the response of the aleutian low to greenhouse warming. Journal of Climate 30, 3907–3925. doi:`10.1175/JCLI-D-15-0789.1`.

Garza, J., Chu, P., Norton, C., Schroeder, T., 2012. Changes of the prevailing trade winds over the islands of hawaii and the north pacific. Journal of Geophysical Research .

Graham, N., Diaz, H., 2001. Evidence for intensification of north pacific winter cyclones since 1948. Bulletin of American Meteorological Society , 1869–1893.

Hall, M.J., Pilkey, O.H., 1991. Effects of hard stabilization on dry beach width for new jersey. Journal of Coastal Research , 771–785.

Hanson, J., Tracy, B., Tolman, H., Scott, R., 2009. Pacific hindcast performance of three numerical wave models. J. Atmos. Oceanic Technol. 26, 1614–1633.

Harney, J., Grossman, E., Richmond, B., Fletcher, C., 1999. Age and composition of carbonate shoreface sediments, kailua bay, oahu, hawaii. Coral Reefs 19, 141–154.

Hasselmann, K., 1973. Measurements of wind?wave growth and swell decay during the joint north seawave project. Ergnzungsheft zur Deutschen Hydrographischen Zeitschrift Reihe , 1–95 suppl. A.

Hitzl, D., Chen, Y.L., Nguyen, H., 2014. Numerical simulations and observations of airflow through the alenuihaha channel, hawaii. Mon. Weather Rev. , 4696–4718.

Holthuijsen, L., 2007. Waves in oceanic and coastal waters. Cambridge University Press , 387.

Horel, J., Wallace, J.M., 1981. Planetary scale atmospheric phenomena associated with the southern oscillation. Mon. Weather Rev. , 813–829.

Hwang, D., 2005. Hawaii coastal hazard mitigation guidebook. A publication of the Hawaii Coastal Zone Management Program, Office of Planning, Department of Business, Economic Development & Tourism, State of Hawaii, University of Hawaii Sea Grant College Program , 216 p.

Jones, S.C., Harr, P.A., Abraham, J., Bosart, L.F., Bowyer, P.J., Evans, J.L., Hanley, D.E., Hanstrum, B.N., Hart, R.E., Lalaurette, F., Sinclair, M.R., Smith, R.K., Thorncroft, C., 2003. The extratropical transition of tropical cyclones: Forecast challenges, current understanding, and future directions. Weather and Forecasting 18, 1052–1092. doi:`10.1175/1520-0434(2003)018<1052:TETOTC>2.0.CO;2`.

Jordan, L., Banks, K., Fisher, L., Walker, B., Gilliam, D., 2010. Elevated sedimentation on coral reefs adjacent to a beach nourishment project. Marine Pollution Bulletin , 261–271.

Komar, P., McDougal, W.G., 1988. Coastal erosion and engineering structures: the oregon experience. Journal of Coastal Research , 77–92.

Kraus, N.C., 1988. The effects of seawalls on the beach: an extended literature review. Journal of Coastal Research , 1–28.

Lander, M., 1994. An exploratory analysis of the relationship between tropical storm formation in the western north pacific and enso. American Meteorological Society 122, 636–651.

Lee, J., Liu, J., Teng, M., 2004. Numerical study on nearshore sediment transport around oahu island in hawaii. Journal of Coastal Research , 1700–1705.

Li, N., Cheung, K.F., Stopa, J.E., Hsiao, F., Chen, Y., Vega, L., Cross, P., 2016. Thirty-four years of hawaii wave hindcast from downscaling of climate forecast system reanalysis. Ocean Modelling , 78–95doi:`10.1016/j.ocemod.2016.02.001`.

Linkin, M., Nigam, S., 2008. The north pacific oscillation-west pacific teleconnection pattern: Mature-phase structure and winter impacts. Journal of Climate 21, 1979–1997. doi:`10.1175/2007JCLI2048.1`.

Lipp, D., 1995. Changes in beach profiles due to wave reflections off seawalls at lanikai, hawaii (thesis). University of Hawaii, Department of Ocean Engineering .

Longuet-Higgins, M., Stewart, R., 1963. A note on wave set-up. Journal of Marine Research , 4–10.

Lygre, A., Krogstad, H., 1986. Maximum entropy estimation of the directional distribution in ocean wave spectra. Journal of Physical Oceanography , 2052–2060.

Mantua, N., Hare, S., Zhang, Y., Wallace, J., Francis, R., 1997. A pacific interdecadal climate oscillation with impacts on salmon production. Bull. Amer. Meteor. Soc. , 1069–1079.

Menèndez, M., Mèndez, F.J., Losada, I.J., Graham, N., 2008. Variability of extreme wave heights in the northeast pacific ocean based on buoy measurements. Geophysical Research Letters , L22607,doi:`10.1029/2008GL035394`.

Miller, T., Fletcher, C., 2003. Waikiki historical analysis of an engineered shoreline. Journal of Coastal Research , 1026–1043.

Mitsuyasu, H., Tasai, F., Suhara, T., Mizuno, S., Ohkusu, M., Honda, T., Rikiishi, K., 1975. Observations of the directional spectrum of ocean waves using a cloverleaf buoy. Journal of Physical Oceanography , 750–760.

Moberly, R., Chamberlain, T., 1964. Hawaiian beach systems. Hawaii Institute of Geophysics Technical Report , Honolulu: University of Hawaii.

Morton, R., 1988. Interactions of storms, seawalls and beaches of the texas coast. Journal of Coastal Research , 113–134.

Nguyen, H., Chen, Y.L., Fujioka, F., 2010. Numerical simulations of island effects on airflow and weather during the summer over the island of oahu. Mon. Weather Rev. , 2253–2280.

Norcross, Z., Fletcher, C., Merrifield, M., 2002. Annual and interannual changes on a reef-fringed pocket beach: Kailua bay, hawaii. Marine Geology , 533–580.

Pérez, J., Méndez, F., Menéndez, M., 2014. Estela: a method for evaluating the source and travel time of the wave energy reaching a local area. Ocean Dynamics , 1181–1191doi:`10.1007/s10236-014-0740-7`.

Phillips, O., 1957. On the generation of waves by turbulent wind. Journal of Fluid Mechanics 2, 417–445.

Plikey, O.H., Wright, H.L., 1988. Seawalls versus beaches. Journal of Coastal Research , 41–64.

Puelo, J., Lankriet, T., Wang, P., 2012. Near bed cross-shore velocity profiles, bed shear stress and friction on the foreshore of a microtidal beach. Coastal Engineering , 6–16.

Rascle, N., Ardhuin, F., 2012. global wave parameter database for geophysical applications. part 2: Model validation with improved source term parameterization. Ocean Model doi:`10.1016/j.ocemod.2012.12.001`.

Rascle, N., Ardhuin, F., Queffeulou, P., Croizé-Fillon, D., 2008. A global wave parameter database for geophysical applications. part 1: Wave-current-turbulence interaction parameters for the open ocean based on traditional parameterizations. Ocean Model , 154–171doi:`10.1016/j.ocemod.2008.07.006`.

Table of Contents

Rocha, C., 2016. Response of the global wave climate to el niño southern oscillation (thesis). University of Hawaii, Department of Ocean and Resource Engineering .

Romine, B.M., Fletcher, C.H., Barbee, M.M., Anderson, T.R., Frazer, L.N., 2013. Are beach erosion rates and sea-level rise related in hawaii? Global and Planetary Change , 149–157.

Rooney, J., Fletcher, C., Engles, M., Grossman, E., Field, M., 2004. El niñ o influence on holocene reef accretion in hawai'i. Pacific Science , 305–324.

Ruggiero, P., Komar, P.D., McDougal, W.G., Marra, J.J., Beach, R.A., 2001. Wave runup, extreme water levels and the erosion of properties backing beaches. Journal of Coastal Research , 407–419.

Saha, S., Moorthi, S., Pan, H.L., Wu, X., Wang, J., Nadiga, S.e.a., 2010. The ncep climate forecast system reanalysis. Bulletin of American Meteorological Society , 1015–1057doi:`10.1175/2010BAMS3001.1`.

Saha, S., Moorthi, S., Wu, X., Wang, J.e.a., 2014. The ncep climate forecast system version 2. Journal of Climate , 2185–2208doi:`10.1175/JCLI-D-12-00823.1`.

Salathè, E., 2006. Influences of a shift in north pacific storm tracks on western north american precipitation under global warming. Geophysical Research Letters 33. doi:`10.1029/2006GL026882`.

Serreze, M., Barrett, A.P., 2008. The summer cyclone maximum over the central arctic ocean. Journal of Climate , 1048–1065doi:`10.1175/2007JCLI1810.1`.

Serreze, M., Carse, F., Barry, R.G., Rogers, J.C., 1997. Icelandic low cyclone activity: Climatological features, linkages with the nao, and relationships with recent changes in the northern hemisphere circulation. Journal of Climate , 453–464doi:`10.1175/1520-0442(1997)010<0453:ILCACF>2.0.CO;2`.

Serreze, M.C., 2009. Northern hemisphere cyclone locations and characteristics from ncep/ncar reanalysis data. Data retrieved from Boulder, Colorado USA: National

Snow and Ice Data Center. Digital media, `ftp://sidads.colorado.edu/pub/DATASETS/atmosphere/nsidc0423_cyclone_ncep_ncar_reanalysis/`.

Stopa, J.E., Cheung, K.F., 2014. Periodicity and patterns of ocean wind and wave climate. J. Geophys. Res. Oceans 119, 5563?5584. doi:`10.1002/2013JC009729`.

Stopa, J.E., Cheung, K.F., Chen, Y.L., 2011. Assessment of wave energy resources in hawaii. Renewable Energy , 554–567doi:`10.1016/j.renene.2010.07.014`.

Stopa, J.E., Filipot, J.F., Li, N., Cheung, K.F., Chen, Y.L., Vega, L., 2013. Wave energy resources along the hawaiian island chain. Renewable Energy , 305–321doi:`10.1016/j.renene.2012.12.030`.

Sverdrup, H., 1947. Wind-driven currents in a baroclinic ocean; with application to the equatorial currents of the eastern pacific. Proc. Natl. Acad. Sci. 33, 318–326. doi:`10.1073/pnas.33.11.318`.

Tait, J.F., Griggs, G.B., 1990. Beach response to the presence of a seawall. Shore and Beach , 11–28.

Thompson, P., Merrifield, M., 2014. A unique asymmetry in the pattern of recent sea level change. Geophysical Research Letters 41, 7675–7683. doi:`10.1002/2014GL061263`.

Trenberth, K., Branstator, G., Karoly, D., Kumar, A., Lau, N., Ropelewski, C., 1998. Progress during toga in understanding and modeling global teleconnections associated with tropical sea surface temperatures. Journal of Geophysical Research 103, 14,291–14,324.

Trenberth, K., Hurrell, J., 1994. Decadal atmosphere-ocean variations in the pacific. Climate Dynamics , 303–319.

Vitousek, S., Fletcher, C., Merrifield, M., Pawlak, G., Storlazzi, C., 2007. Model scenarios of shoreline change at kaanapali beach, maui, hawaii: Seasonal and extreme events. Coastal Sediments ?07, American Society of Civil Engineers, New Orleans, La. , 1227–1240.

Wallace, J.M., Gutzler, D., 1981. Teleconnections in the geopotential height field during the northern hemisphere winter. Mon. Weather Rev. , 784–812.

Wang, H., Sun, J., Fan, K., 2007. Relationships between the north pacific oscillation and the typhoon/hurricane frequencies. Science in China Series D: Earth Sciences 50, 1409–1416.

Wright, L., Short, A., 1983. Morphodynamics of beaches and surf zones in australia. In: Handbook of Coastal Processes and Erosion, ed. KOMIARP, .D., CRC Press, Boca Raton, Florida , 35–64.

Yang, Y., Chen, Y., Fujoka, F.M., 2005. Numerical simulations of the island-induced circulations over the island of hawaii during harp. Monthly Weather Review , 3693–3713.

Yin, J.H., 2005. A consistent poleward shift of the storm tracks in simulations of 21st century climate. Geophys. Res. Lett. 32. doi:`10.1029/2005GL023684`.

Zhang, Y., Wallace, J., Battisti, D., 1997. Enso-like interdecadal variability: 1900-93. Climate , 1004–1020.

Zhu, X., Sun, J., Liu, Z., Liu, Q., Martin, J., 2007. A synoptic analysis of the interannual variability of winter cyclone activity in the aleutian low region. American Meteorological Society 20, 1523–1538. doi:`10.1175/JCLI4077.1`.